Mechanisms and Manipulation of Ion Beam Pattern Formation on Si(001)

I n a u g u r a l - D i s s e r t a t i o n

zur

Erlangung des Doktorgrades

der Mathematisch-Naturwissenschaftlichen Fakultät

der Universität zu Köln

vorgelegt von

Sven Macko

aus Duisburg

Köln 2011

Berichterstatter:	Prof. Dr. Thomas Michely
(Gutachter)	Prof. Dr. Hans Hofsäss
Vorsitzender der Prüfungskommission:	Prof. Dr. Joachim Krug

Tag der mündlichen Prüfung: 11. Oktober 2011

Abstract

Ion beam pattern formation is a versatile and cost-efficient tool for the fabrication of well-ordered nanostructures. Furthermore, silicon is known to be a prime material in microelectronics. The thesis at hand deals with pattern formation on Si(001) through 2 keV Kr^+ ion beam erosion under ultra high vacuum conditions investigated by *in situ* scanning tunneling microscopy, *ex situ* atomic force microscopy, scanning electron microscopy, and transmission electron microscopy. Under highly pure conditions, at room temperature, and for fluences of $F \approx 1 \times 10^{22}\,\mathrm{ions\,m^{-2}}$, no ion beam induced patterns develop for ion incidence angles $\vartheta \leq 55^\circ$ with respect to the global surface normal. In fact, the ion beam induces a smoothing of preformed patterns. Only for grazing incidence angles $60^\circ \leq \vartheta < 81^\circ$ pronounced ripple and tiled roof patterns develop. Analysis of the fluence dependence of pattern formation was conducted at $\vartheta = 75^\circ$ in the unstable ion incidence angular range. The initially flat surface develops small amplitude, regular ripple patterns which then evolve to large amplitude, irregular facet patterns.

Experiments were conducted to rule out or determine the processes of relevance in ion beam pattern formation on Si(001) with impurities. Co-deposition of stainless steel during ion beam erosion results in well developed hole, dot and ripple patterns for even small ion fluences of $F \approx 5 \times 10^{21}\,\mathrm{ions\,m^{-2}}$. The key factor determining the type of pattern realized is the ion-to-impurity arrival ratio. While in a broad range from 140 K to 440 K pattern formation tends to be temperature independent, dramatic changes take place above a threshold temperature of about 600 K, when structures of crystalline iron silicide are shaped upon the surface. For these high temperatures nanopillars and spongelike patterns with amplitudes in the order of 100 nm and directed towards the ion beam evolve. Furthermore, variation of the angle between ion beam and impurity source has a significant effect on pattern formation. The larger this angle is, the more efficient the pattern formation. This observation highlights the relevance of shadowing. Our investigations on the phenomenology of metal assisted ion beam pattern formation identify height fluctuations, local flux variations, induced chemical inhomogeneities, silicide formation and ensuing composition-dependent sputtering to be of relevance.

Kurzfassung

Ionenstrahlinduzierte Musterbildung ist ein vielseitiges und kostengünstiges Verfahren für die Herstellung von regelmäßigen Nanostrukturen. Darüber hinaus ist Silizium ein maßgebendes Material in der Mikroelektronik.

Die vorliegende Dissertation behandelt die Musterbildung auf Si(001) mittels 2 keV Kr^+ Beschuss unter Ultrahochvakuumbedingungen. Die Untersuchungen wurden mittels *in situ* Rastertunnelmikroskopie, *ex situ* Rasterkraftmikroskopie, Rasterelektronenmikroskopie und Transmissionselektronenmikroskopie durchgeführt. Unter reinsten Bedingungen bei Raumtemperatur und Ionenfluenzen von $F \approx 1 \times 10^{22}$ Ionen m^{-2} bilden sich keine Muster für Ioneneinfallswinkel $\vartheta \leq 55°$ relativ zur globalen Oberflächennormalen. Im Gegenteil, senkrecht einfallende Ionen glätten eine anfänglich raue Siliziumoberfläche. Ausschließlich für flach bis streifend einfallende Ionen mit $60° \leq \vartheta < 81°$ bilden sich ausgeprägte Wellen- und ziegeldachartige Muster. Es wurde eine fluenzabhängige Messreihe im instabilen Ioneneinfallswinkelbereich mit $\vartheta = 75°$ durchgeführt. Die anfänglich flache Oberfläche entwickelt sich über regelmäßige Wellenmuster mit kleiner Amplitude zu einem facettierten ungeordnetem Muster mit großer Amplitude.

Weitere Experimente wurden durchgeführt, um relevante Prozesse in der ionenstrahlinduzierten Musterbildung auf Si(001) unter Hinzugabe von Verunreinigungen aufzudecken. Bereits bei niedrigen Ionenfluenzen von $F \approx 5 \times 10^{21}$ ions m^{-2} führt Kodeposition von Stahl während des Ionenbeschusses der Si Oberfläche zu ausgeprägten Loch-, Punkt- und Wellenmustern. Der entscheidende Faktor, der den resultierenden Mustertyp festlegt, ist das Ionen-zu-Verunreinigung-Flussverhältnis. Während in einem großen Temperaturbereich von 140 K bis 440 K die Musterbildung weitestgehend temperaturunabhängig ist, ergeben sich drastische Unterschiede oberhalb einer kritischen Temperatur von ungefähr 600 K, wobei sich kristalline Strukturen aus Eisensilizid auf der Oberfläche bilden. Bei dieser hohen Temperatur entwickeln sich nanoskalige Säulen und schwammartige Muster mit Höhen in der Größenordnung von 100 nm. Die Muster sind dabei zum Ionenstrahl hin ausgerichtet. Änderungen des Winkels zwischen Ionenstrahl und den einfallenden Verunreinigungen haben eine starken Effekt auf die Musterbildung. Je größer der einschließende Winkel, desto effizienter ist die Musterbildung. Diese Beobachtung führt zu dem Schluss, dass Abschattungseffekte von Bedeutung sind. Unsere Untersuchungen zur Phänomenologie der ionenstrahlinduzierten Musterbildung mithilfe metallischer Verunreinigungen führten zu folgenden Ergebnissen: Höhenfluktuationen, lokale Unterschiede im Teilchenfluss, induzierte Ungleichmäßigkeiten in der chemischen Zusammensetzung, Silizidbildung und eine daraus folgende kompositionsabhängige Zerstäubungsausbeute sind ausschlaggebend.

Contents

Abstract iii

Table of Contents v

1 Preface 1

Frequently used symbols 1

2 Fundamentals 5

2.1 Ion Surface Interaction . . . 5
2.2 The Kinetic Monte Carlo Simulation Software TRIM.SP . . . 11
2.3 Smoothing Mechanisms . . . 13
2.4 Roughening Mechanisms . . . 15
2.5 Gradient Dependent Surface Topography Development . . . 19
2.6 Continuum Modelling . . . 21
2.7 Modelling Metal Assisted Ion Beam Pattern Formation . . . 25
2.8 Previous Work . . . 26

3 Experimental 37

3.1 UHV System *Athene* . . . 37
3.2 *ex situ* Measurement Methods . . . 39
3.3 Sample Preparation . . . 40
3.4 Data Evaluation . . . 44

4 Ion Beam Pattern Formation on Si(001) 49

4.1 Ion Beam Induced Amorphization of Si(001) . . . 49
4.2 Ion Beam Incidence Angle Dependence . . . 50
4.3 Ion Beam Induced Smoothing . . . 58
4.4 Fluence Dependent Pattern Evolution . . . 59
4.5 Fabrication of Crystalline Ripple Patterns . . . 66

5 Impurity Assisted Ion Beam Patterning on Si(001) 69
5.1 Impurity Induced Pattern Morphologies by Co-sputter Deposition . . 69
5.2 Temperature Dependence 80
5.3 Morphological Phase Transition:
From a Smooth to a Rippled Surface 86
5.4 Impurity Assisted Ion Beam Patterning
in the Crystalline Phase 93
5.5 Impurity to Ion Flux Ratio Dependence 105
5.6 Fluence Dependent Pattern Evolution 109
5.7 Dependence on the Directionality of Incoming Kr^+ and Fe 116
5.8 Co-deposition Directionality and Ion Beam Patterning:
A Stability Analysis 120
5.9 Directionality and Flux Ratio Dependence:
A Pattern Phase Diagram 124

6 Summary 131

7 Outlook 135

References 137

A Publications 157

B Ripple Profile Erosion Velocity Simulation: Gnuplot Code 159

C Acknowledgements 161

D Curriculum Vitae 165

1 Preface

Ion beam surface patterning of amorphous and crystalline materials has attracted considerable interest in the past years. This interest is of twofold origin. First, it results from the complex physics involved in ion beam patterning which has not yet been entirely uncovered. Second, ion beam nanopatterning is a relatively cheap and low tech method for creating various regular nanoscale surface patterns over large, wafersize areas. Such structured surfaces may be used as templates for subsequent nanostructure fabrication. There are a number of potential applications: 'Moth eye' surfaces and facet structures with a high aspect ratio may serve as an anti-reflection surface finish due to their gradation of the refractive index [1–3]. Specifically patterned Si surfaces are capable of increasing the efficiency of solar cells [4–6]. Well aligned ripple patterns are a beneficial substrate for orientation of large molecules [7]. Nanoporous silicon was identified not only as a bio-compatible material supporting cell and apatite growth (the latter being a major component of bone tissue) [8; 9] but also being a promising material for small sensitive sensors [10]. Arrays of pillars oriented upstanding to the Si substrate were found to be an ideal material for enhancing the performance of thermoelectric generators [11], optoelectronic devices [12; 13] as well as being useful for flat panel displays as field emitter arrays [14; 15]. Finally, magnetic plain rods and pillars show interesting properties in the field of nanomagnetism [16–20]. As specified above, the variety of possible applications is manyfold.

As Si is a prime material of technology and readily available in high purity and quality, it is not surprising that the ion beam patterning studies are numerous for this material. At room temperature Si readily amorphizes during ion exposure [21]. The loss of anisotropy and crystal structure appears to make it an ideal material to be described by the continuum theory of ion erosion, which effectively averages out

complex atomistic details of the processes.

Nanopatterns are observed by many groups following ion-beam erosion of silicon surfaces and the arrangement of individual features can be highly regular. While there are certain conditions under which ion beam erosion of Si does not cause pattern formation [22; 23], the overwhelming number of investigations find pattern formation on Si in a large parameter space.

The variety and complexity of observed patterns stimulated the development of continuum theories [24–28] extending the concept of the curvature dependent yield as a prime destabilization mechanism.

However, in the past, even for similar ion-beam parameters and formation conditions, the type of pattern created appeared to depend on the laboratory of fabrication and the ion-beam apparatus used. In this situation the question arose, whether there is a hidden chemical or impurity factor in pattern formation on Si. Such a largely disregarded attribute could make it impossible for theory to come up with an adequate description of pattern formation.

The present thesis contributes to the cognitive process of the last years that impurities play a crucial role in the ion beam pattern formation process. Subsequently it was found that no patterns develop on Si surfaces in a large angular range of ion incidence $0° \leq \vartheta \leq 50°$ with respect to the surface normal, if no impurities are present or co-deposited [22; 29–31]. All patterns observed in this angular range – in the past often erroneously interpreted in terms of pure ion beam erosion mechanisms – revealed to be just a consequence of unintentional co-deposition of a non-volatile species during erosion resulting in a two-component surface system.

These findings not only prepare the ground for careful and clean ion beam erosion experiments, which may serve as an empirical basis for a theoretical description of single component ion beam erosion, they also provide a strong parameter for tuning patterns and developing new ones [32–36], qualitatively different from the patterns observed in a one component situation.

The first part of this work will address pure ion beam erosion experiments on

Si without impurities. Analyzing the resulting surface morphology of angle and fluence dependent measurements gives insight to the fundamental ion beam pattern formation mechanism.

In the second part we investigate the phenomenology of impurity driven pattern formation on Si(001) using co-deposition of stainless steel. The goal of our analysis lies in separating and distinguishing the most relevant factors for ion beam induced pattern formation with co-deposition. Knowledge of such factors is a prerequisite for an adequate modelling of this situation and thus for manipulating the resulting patterns. Key findings relate to the effect of chemical reactions on pattern formation, to critical fluctuations causing a pattern bifurcation as well as to local flux variations of the co-deposited species causing its inhomogeneous lateral distribution.

2 Fundamentals

2.1 Ion Surface Interaction

This chapter deals with the phenomenology of ion surface interaction by low energy (100 eV – 10 keV) noble gas ions with silicon as a target material. The elucidated fundamentals of the present section are based primarily upon the book *M. Nastasi, J. W. Mayer, and J. K. Hirvonen: Ion-Solid interactions: Fundamentals and Applications* [37] and the volume series *R. Behrisch, K. Wittmaack, and W. Eckstein: Sputtering by Particle Bombardment* [38–40].

Collision Cascade

An impinging charged particle induces a collision cascade in a solid and causes damage in the near surface layers by transferring energy to the target atoms.

Figure 2.1 illustrates the ion induced collision cascade. The impinging energetic ion (blue) with a *global* incident angle of ϑ interacts within a primary collision (red) with stationary surface and bulk atoms[1]. Due to the ion impact the knocked-on atoms leave their site and may still have enough energy to induce further collision events with neighboring atoms leading to secondary collisions (orange). Aside of vacancy production events and replacement collisions most of the atoms remain as interstitial atoms (green) until their kinetic energy is depleted and the energy drops below the displacement energy of a target atom. The result is a highly disordered region around the path of the ion. Near surface atoms may be sputtered that means they are removed from the surface. Not the direct collision caused by the ion but

[1]Note that we distinguish here and in the following between the *global* angle of incidence ϑ (measured with respect to the normal of the average surface plane) and the *local* angle of incidence θ (measured with respect to the surface normal of a specific surface element).

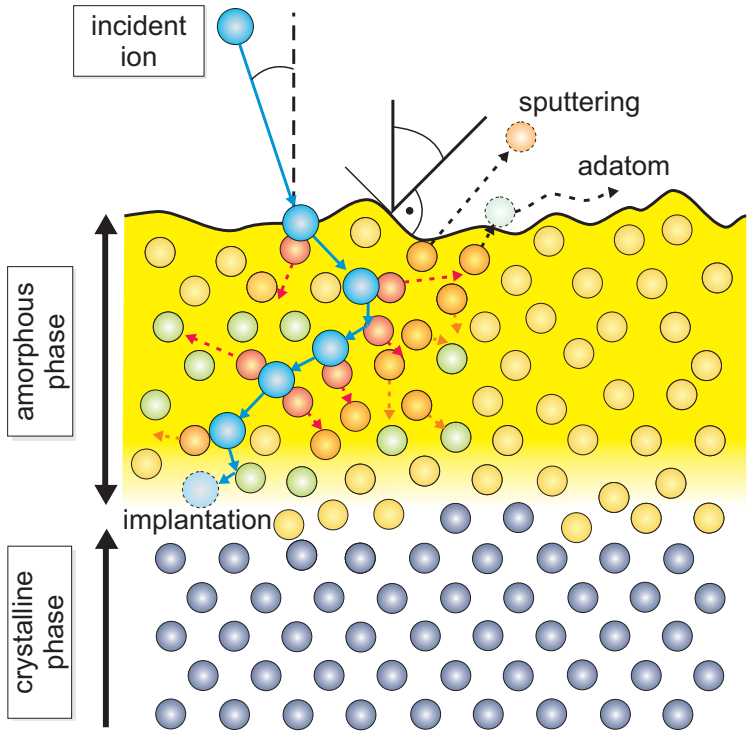

Figure 2.1: Schematic view of the ion induced collision cascade. An impinging ion (blue) induces a collision cascade. Events such as ion implantation, replacement collisions, vacancy production, interstitial and adatom generation, and sputtering occur. An amorphous layer forms near the surface on top of the crystalline layer (modified from [41]).

secondary collisions by atoms lead to sputtering of a surface atom. These sputtered atoms originate from the first two layers, nearly independent of the ion energy and the angle of incidence [42]. A gauge for the erosion is the sputtering yield Y which gives the mean number of sputtered atoms per incident ion. If the energy of a hit surface atom is not high enough to overcome the surface binding energy and leave the surface boundary it may act as a mobile adatom. The mobile adatom contributes to surface diffusion, before being incorporated back into the solid bulk. By undergoing a series of collisions with the atoms and electrons in the target the ion loses energy at a rate of the stopping power dE/dx:

$$\frac{dE}{dx} = \left.\frac{dE}{dx}\right|_n + \left.\frac{dE}{dx}\right|_e \tag{2.1}$$

The subscripts n and e denote nuclear and electronic collisions, respectively.

Nuclear collisions may account for large discrete energy losses and a significant angular deflection of the ion trajectory. The energy is transmitted as translatory motion to a target atom. This process is responsible for the production of lattice disorder by displacement of atoms from their lattice positions.

The stopping power depends on the energy and mass of the ion as well as on the substrate material. The nuclear energy loss can be calculated as follows ([37] p. 94):

$$\left.\frac{dE}{dx}\right|_n = 0.28\,[\mathrm{eV\,nm^2}] \quad \frac{Z_1 Z_2}{\Omega Z_1^{\frac{1}{2}} Z_2^{\frac{1}{2}}} \quad \frac{M_1}{M_1 + M_2} \tag{2.2}$$

with Ω being the atomic volume.

Equation 2.2 is a reasonable approximation for most of the keV energy region. For 2 keV Kr^+ ions impinging upon a silicon target, as in our experiments, the nuclear energy loss calculated by equation 2.2 is 235 eV/nm.

Electronic collisions between the ion and the electrons in the solid (excitation or ionization) involve much smaller energy losses per collision. Electronic stopping originates from the transfer of momentum that occurs when target electrons are captured by the projectile. Those electrons have to be accelerated up to the ion velocity and the ion loses a small amount of momentum inducing a negligible deflection of the ion trajectory, and negligible lattice disorder [37].

Nuclear stopping predominates for low energies and high atomic numbers Z_1, whereas electronic stopping takes over for high energies and low atomic numbers Z_1. In our investigated energy range of keV ion bombardment the electronic excitation can be neglected. The energy transferred to electrons is small compared with the exchange of kinetic energy between the atoms [37]. The whole energy loss process slows the ion down and after it comes to rest it remains implanted (blue dashed). The depth distribution of implanted ions in amorphous materials is expected to have a Gaussian shape and is characterized by a projected range R_p and a straggling ΔR_p [37].

Binary Collisions

The collision cascade may be described via binary collision approximation. As diagrammed in figure 2.2 an ion with energy E_0, velocity v_0 and mass M_1 hits an atom at rest with mass M_2. After collision the ion is scattered by the angle ψ and its energy and velocity is reduced to E_1 and v_1 while the energy E_2 is transferred to the knocked-on atom recoiled by the angle φ. In the investigated low energy bombardment range the mean free path between collisions is far greater than the interatomic spacing. The probability of three or more particle collisions is very small. The energy transfer of a collision event is characterized by the consideration of the principles of conservation of momentum and energy. These considerations lead to following equations [37]:

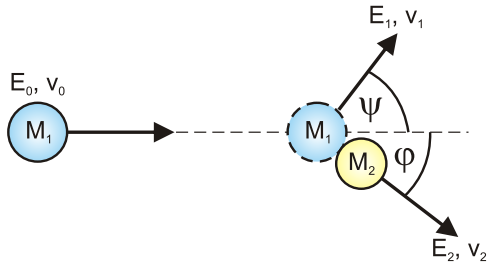

Figure 2.2: Sketch of an elastic binary collision. A moving particle M_1 hits a particle at rest M_2 (see text).

Energy of the scattered projectile:

$$E_1 = E_0 \frac{\left(\frac{M_1}{M_2}\cos\psi \pm \sqrt{1-(\frac{M_1}{M_2})^2\sin^2\psi}\right)^2}{\left(1+\frac{M_1}{M_2}\right)^2}, \qquad \psi \leq \sin^{-1}\left(\frac{M_2}{M_1}\right) \tag{2.3}$$

Maximum energy transferable in a head-on collision:

$$E_2^{max} = \frac{4\,M_1 M_2}{M_1+M_2} E_0 \tag{2.4}$$

Energy transferred to the target atom:

$$E_2 = E_2^{max} \sin^2\left(\frac{\pi - 2\varphi}{2}\right) \tag{2.5}$$

Angle of the scattered projectile:

$$\tan\psi = \frac{M_2 \sin(\pi - 2\varphi)}{M_1 + M_2 \cos(\pi - 2\varphi)} \tag{2.6}$$

The interaction of charged particles is described in the simplest form by a Coulomb potential ([37] p. 70).Specifically in the keV energy range of particle collisions a screened Coulomb potential is more appropriate as the electron clouds effectively screen the nucleus [43–46].

Ion Induced Amorphization

The major energy fraction of a keV ion collision with the target is transferred to the primary recoiled atoms which in turn convert the kinetic energy to a large extent into phonon excitations of target atoms [43; 47]. The resulting local annealing amounts to a temperature of a few 1000 K and is termed *thermal spike*. The heat dissipates within a timescale of ps [48; 49]. In comparison the impact rate of incoming ions on a certain surface point with typically used ion fluxes is in the range of seconds i.e. higher on the timescale by a factor of 10^9 [41; 47]. Regarding room temperature ion beam erosion experiments on silicon, the material does not recrystallize due to the rapid quenching. This process generates defects in the near surface region. With each impinging ion and an increasing number of collision cascades an amorphous layer forms near the surface above the crystalline layer [50; 51]. The thickness of the amorphous layer corresponds to the mean penetration depth of the ion [41] which depends on the energy E_0 and mass M_1 of the incoming ion and the mean free path of collisions.

Angle Dependence

Shifting the angle of incidence from normal to oblique incidence the ion path is moved closer to the surface. With increasing energy deposited by the ion in the near surface region more surface atoms are affected by the collision cascade and the sputtering yield rises. Ion beam incidence angle dependent kinetic Monte Carlo (KMC) simulations for low energy noble gas ion erosion on Si and other various targets show that the maximum sputtering yield is found for oblique *global* incident angles with $\vartheta \geq 60°$ ([40] p. 101 ff.). At grazing incidence the fraction of reflected ions increases accompanied by a decrease of erosion and hence a diminished sputtering yield. The relative width of the distribution depends primarily on the ratio between ion mass M_1 and the mass of the substrate atom M_2.

Spatial Sputtering Yield Distribution

The angular sputtering yield distribution of emitted particles depends predominantly on the ion energy, the ion to atom mass ratio and the angle of incidence. For normal incident ions the angular distribution of sputtered particles may be described in a first approximation by a cosine distribution ([40] p. 4). By sputtering with heavy ions at low bombarding energies close to the sputtering threshold the majority of atoms leave the surface at large angles. Contrariwise the emission distribution is moved towards the normal direction by sputtering with light ions and higher energies ([40] p. 4, [52]). In the case of oblique ion incidence the major fraction of atoms is shifted away from the incoming ion beam. Less than 5% of the sputtered atoms are ionized; emitted atoms are primarily neutral atoms in the ground state ([38] p. 5).

Sputtering Compound Targets

Sputtering a multicomponent target leads to different partial sputtering yields for different elements. This is due to the varying momentum transfers of the incoming ion to the different alloy components [40]. This so-called *preferential sputtering* and

the angular and energy distribution of the sputtered species depend on the masses and the surface binding energies of the respective species in the compound material. At low fluence the ion induced collision cascade will change the stoichiometry in the projectile penetration range ([38] p. 3). With increasing fluence one component is removed at a higher rate so that the surface layer is enriched in the other component until a steady state condition is established ([40] p. 129). A higher ion mass leads to a lower steady state fluence. Furthermore, the different constituents may be sputtered with slightly different angular distributions.

Whereas temperature does not influence the collision cascade of one component amorphous targets (except for temperatures near the melting point), in the case of multicomponent targets diffusion and segregation can change and with it the collisional cascade ([40] p. 132, [53; 54]).

2.2 The Kinetic Monte Carlo Simulation Software TRIM.SP

The Monte Carlo program TRIM (transport of ions in matter) is capable of reproducing experimental data of collisional sputtering processes [55; 56]. TRIM.SP (sputtering) is an extension of the original program TRIM and is also based on the binary collision approximation. Total sputtering yields and also more detailed information on angular and energy distributions of sputtered particles may be calculated [57].

As discussed in section 2.1 the sputtering yield depends mainly on the projectile-target atom combination, on the energy and angle of incidence of the projectile and the surface binding energy.

For the calculation proper values for surface and bulk binding energies are necessary. The program includes electronic energy loss and uses an analytic formula which is based on realistic interatomic potentials for determining particle scattering angles and the energy transfer to target atoms [55]. In the simulation each particle

starts with a given energy, position, and direction. Both incident particle trajectories and those of the target atoms are followed collision after collision throughout their slowing-down process. The particles change their direction as a result of binary nuclear (elastic) collisions and move in a straight path between collisions until their energy is reduced by nuclear and electronic (inelastic) energy losses. The record of a moving particle ends when its energy falls below a predetermined energy or the particle leaves the target surface.

In the simulation the target atoms are localized at random locations so that the directional properties of a crystal lattice are ignored. The path length between collisions is determined from the target density [55]. This approach is feasible for amorphous target materials as in our case silicon already becomes amorphous at very low erosion fluences.

TRIM.SP uses a planar surface potential; the emitted particles have to overcome the surface binding energy which is closely approximated by the heat of sublimation given by the sum of the heat of fusion (melting) and the heat of evaporation. The surface potential causes an energy loss and a refraction for target atoms leaving the surface [57].

One needs to be careful using the simulated data for the evaluation of experiments resulting in a rough surface e.g. a patterned surface [57]. In particular considering a perturbed surface the bonding of an in-surface atom depends on the local varying coordination number. Various authors argue that the energy required to remove an atom from a rough surface should be greater by some 30% - 40% ([40] p. 236).

Simulations of sputtering multicomponent targets are only truthful in case of a non-changing target composition with erosion time. Until equilibrium is established, reflection and sputtering depend on the fluence of projectiles [42]. Therefore the static version TRIM.SP may only be used for the low fluence case or for equilibrium. For the specific case of fluence dependent preferential sputtering of multicomponent materials TRIM.SP was extended under the designation TRIDYN [58]. Being suitable for dynamical calculations, TRIDYN covers simultaneously recoil

implantation, cascade mixing and surface recession [52].

2.3 Smoothing Mechanisms

Surface Diffusion

Mullins derived an equation for the height evolution considering surface diffusion. A small slope approximation for the surface is taken into account and the atomistic nature of the crystal and crystalline imperfections are ignored [59]. Gradients of chemical potential along the surface are associated with gradients of curvature. The chemical potential changes when an atom is transferred from a point of zero curvature to a point of curvature K on the surface. Therefore such gradients produce a drift of surface atoms [60].

$$\frac{\partial z}{\partial t} = -\frac{D_s \gamma \Omega^2 n_s}{k_B T} \nabla^4 z \tag{2.7}$$

$z, D_s, \gamma, \Omega, n_s, k_B$ and T denote the surface height, surface diffusion constant, surface free energy, atomic volume, surface density of atoms, Boltzmann constant, and temperature, respectively.

Ion-Irradiation-Enhanced Viscous Flow

Ion irradiation leads to a flow within a thin amorphous surface layer with thickness a_z of the ion penetration range. This thin viscous layer enhances material transport on the eroded target [61; 62]. The viscous flow is described by a *hydrodynamic* model treating the targets crystalline to amorphous transition as solid-liquid interface. Besides, the model is valid in the range where the surface layer thickness a_z is much smaller than the corrugation wavelength Λ.

The viscous term is found by solving the Navier-Stokes equation in the limit of small Reynolds numbers with no slip condition at the solid-liquid interface and

vanishing shear stress at the surface [60]. The linear approximation yields:

$$\frac{\partial z}{\partial t} = \frac{\gamma a_z^3}{3\eta_{ion}} \quad \nabla^4 z, \tag{2.8}$$

in which η denotes the viscosity. In this model changes in corrugation wavelength Λ with temperature T may be attributed to a temperature dependence of the ion-induced viscosity η_{ion} [63].

Ballistic Smoothing

Ion impacts form subnanometer craters next to the impact point. The ballistic smoothing characterizes an ion impact-induced downhill current at the atomic scale. In the top layer these currents cause a strong smoothing of initially rough substrates by erosion of hills into neighboring hollows.

Assuming that, the incoming ions with a *local* angle of incidence θ are directed towards the $-x$-direction, the lateral atomic shifts in the direction of the incoming particle are Δx_i. The sum of atomic shifts enters by means of $-\delta\cos(\theta)$ and the flux Φ_{ion} of incoming ions enters using $\Phi_{ion}/\cos(\theta)$ [60].

$$\frac{\partial z}{\partial t} = -\frac{\Phi_{ion}\Omega\,\delta(E_0,\theta)}{\tan(\theta)} \quad \nabla^2 z, \qquad \delta = \sum_i \Delta x_i \tag{2.9}$$

A linear relation is found between the displacement magnitude δ of the currents and the surface slope [64]. The energy dependent saturation of the impact induced smoothing is likely caused by the increase of implantation depth for higher energies. In this case a major part of the impact energy is released in the bulk and is no more available for surface currents.

Vauth and Mayr [60] have shown by molecular dynamic simulations that surface diffusion is a non-relevant surface smoothing mechanism for semiconductor glasses at room temperature. Depending on the wavelength of periodic surface structures, either surface viscous flow or ballistic smoothing dominates for smaller or larger structures, respectively [60].

Redeposition

The mechanism of redeposition describes the influence of sputtered particles which do not leave the surface entirely but are redeposited at a different distant location. This mechanism becomes increasingly important in the case of a highly corrugated surface with high aspect ratio [25]. Particles on ridges are primarily moving away from the target whereas those from the valleys frequently reattach to the neighboring sidewalls [65]. The net current of material from higher to lower lying regions is explained by the forward peaking of the sputtered particle distribution in the direction of flight of the impinging ion [25]. Hence, redeposition leads to a higher deposition rate in the depressions compared to the hillocks and associated with this the erosion velocity decreases from the top of the mountains to the lowest points of the valleys [65]. Bradley [66] showed recently that redeposition which was considered to be a prime mechanism for dot pattern formation is a nonlinear local effect and thus not the physical mechanism responsible for the formation of hexagonal arrays of nanodots.

2.4 Roughening Mechanisms

Statistical Roughening

Every single impinging ion forms an impact crater on the target surface and leads to a roughening on the atomic scale. The crater shape depends primarily on the ion energy, ion mass and angle of incidence; in our case of an amorphous Si target, due to high ion fluences the influence of crystallographic directions is not applicable. An ion impact redistributes the target surface atoms. Low energy Ar^+ ion impact craters on Si surfaces were already investigated experimentally by STM [67] and as well analyzed by molecular dynamic simulations [68].

On the basis of Benninghoven's observation of the successive ion beam etching of surface layers, Carter outlines a stochastic roughening mechanism [69; 70]. The

random statistical arrival in time and space of individual ions onto the surface leads to distinct sputtering events. The outermost surface layer is eroded and simultaneously exposes atoms in the layer below to ions arriving afterwards. With increasing fluence deeper layers are exposed to the incident ions and are sputtered gradually which leads to etch pit structures [71]. The erosion process which consists of independent discrete random occurrences can be described by a Poisson distribution. The sputtered depth conforms with the mean depth $\langle z \rangle$ of erosion and represents the expected value of the poisson distribution [70]:

$$\langle z \rangle = \frac{\Phi\, t\, Y(\vartheta)}{n} \tag{2.10}$$

The standard deviation of $\langle z \rangle$ identifies the roughness σ and is equal to:

$$\sigma = \sqrt{\frac{\Phi\, t\, Y(\vartheta)}{n}} \tag{2.11}$$

While the sputtered depth increases linearly with fluence the roughness σ increases with the square root of the fluence.

Curvature Dependent Roughening

Sigmund introduced a roughening mechanism that depends on the surface curvature. By analyzing the shape of the ion induced collision cascade, the author approximates the deposited energy profile inside the solid by a Gaussian [72]. The absolute value of deposited energy at the surface depends on the surface curvature. The elliptical contours in figure 2.3 illustrate the deposition of the impinging ion energy inside the bulk. The erosion velocity normal to the surface at a point (x, y) at the surface is proportional to the total energy deposited there from ion impacts at nearby points. The total energy deposited at a surface point at a crest is lower in comparison to the energy deposited at a surface point in a valley. This relation is indicated in figure 2.3 by differing distances from the considered ion impact points to the nearby

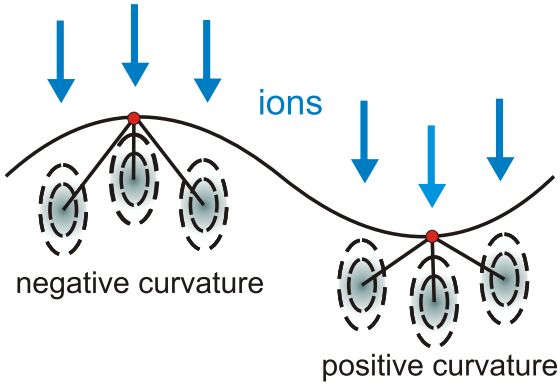

Figure 2.3: Schematic view of the near surface energy deposition by energetic ions (see text).

centers of energy deposition. Therefore, sputtering in valleys is enhanced relative to crests which leads to a surface roughening [72].

Scattering

When a surface is rough resulting in features with a high slope, incoming ions may be reflected at the steep feature flanks; thereby the energy transfer is small. Using ions of oblique incidence, the scattering effect may take place at even lower feature slopes as the relative angle between the ion beam and the local surface must be small. The reflected ions with marginally reduced kinetic energy contribute to erosion so that the etching rate is higher at the bottom of the features [73; 74].

Coarsening Mechanism

Hauffe investigated the coarsening of a faceted surface during ion beam erosion experiments. At each fluence facets from small to large exist while the average and maximum pattern wavelength increase with ion fluence [75]. The coarsening mechanism is sketched in figure 2.4.

The main idea is that ions reflected at facets contribute to erosion whereby the

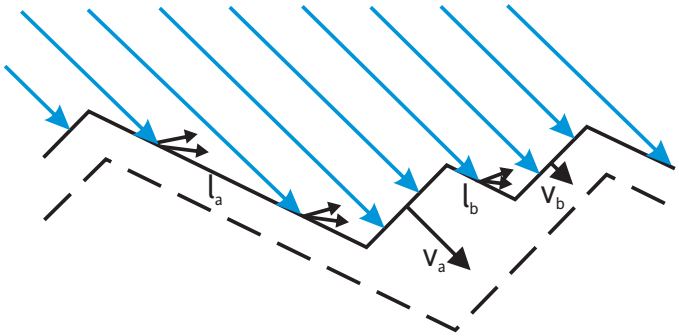

Figure 2.4: Coarsening mechanism: Small facets disappear next to larger facets according to $v_a > v_b$ [75].

erosion is enhanced on an arbitrary area and depends on the size of adjacent facets. As diagrammed the surface element l_a is larger than l_b. From this it follows that the number of reflected ions is larger at l_a. As reflected ions hit the neighbouring facets, the erosion velocity v_a is larger than v_b. Ergo, small facets next to larger facets disappear as displayed by the dashed line which represents the resulting surface.

Furthermore, Hauffe proposes this mechanism in order to enforce roughening. The mechanism begins to work at very small dimensions of relief. Thereby the start relief could be produced by random ion impacts leading to critical hole nuclei. To gain roughening the single pit erosion velocity on the bottom has to be higher than the erosion velocity of the initial surface which can be realized by additional sputtering by means of ions reflected at the slopes of the pit [75].

Shadowing

Shadowing stands for the effect that incoming particles do not reach certain surface points due to nearby surface features which block the particle stream [74].

Due to the larger receiving solid angle on a crest in comparison to a valley, in the case of ion irradiation valleys are less eroded while in the case of deposition the growth in valleys is diminished. This means that in the case of ion erosion, shadowing represents a smoothing mechanism while in the case of deposition it

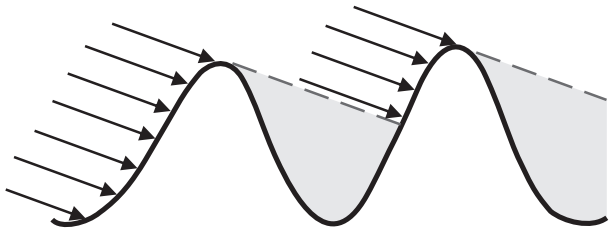

Figure 2.5: Illustration of the shadowing mechanism. The shadowed surface area (coloured grey) receives less incoming particles due to nearby surface features which block the particle stream.

leads to a roughening and a growth instability of the surface [74].

2.5 Gradient Dependent Surface Topography Development

Early theoretical work in the continuum theory approximation considered the dependence of the sputtering yield Y on the angle θ of the ion beam with respect to the *local* surface normal as a decisive factor for surface topographical evolution [76–79]. It is assumed that surface changes occur only as a result of atomic ejection, so that surface relaxation due to diffusion and the possibility of redeposition is ignored.

The erosion rate $\nu_\perp$ normal to the surface depends on its orientation θ towards the ion beam [76]:

$$\nu_\perp(\theta) = -\frac{\Phi_{ion}\cos\theta}{n} Y(\theta) \tag{2.12}$$

where $\Phi_{ion}\cos\theta$ is the effective ion flux onto a surface element with the local angle of incidence θ, n the number of atoms per unit volume of the target and $Y(\theta)$ the angle dependent sputtering yield.

The form of the angle dependent sputtering yield $Y(\theta)$ is displayed in figure 2.6 with a minimum at $\theta_\perp = 0$ a maximum at the critical local angle of incidence θ_p and reducing to zero at grazing incidence as $\theta_\parallel \to 90$ [76].

The authors derive conditions for an equilibrium topography for sputtering of

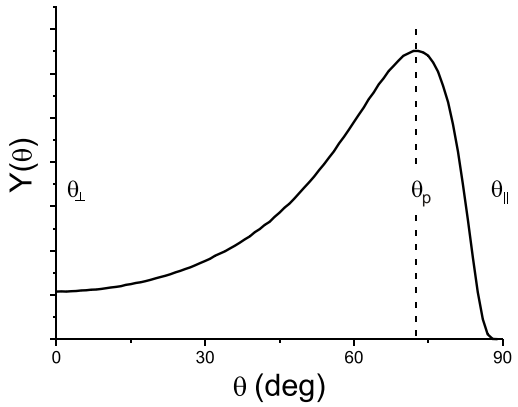

Figure 2.6: Common angle dependent sputtering yield curve (see text).

a particular curved and oriented surface. The change of the surface gradient with time t at position x is identified as follows [77]:

$$\begin{aligned} -\left.\frac{\partial\theta}{\partial t}\right|_x &= -\frac{\Phi_{ion}\cos\theta}{nr}\ \frac{\partial Y(\theta)}{\partial\theta} \\ &= -\frac{\Phi_{ion}}{n}\cos^2\theta\ \frac{\partial Y(\theta)}{\partial\theta}\ \left.\frac{\partial\theta}{\partial x}\right|_t \end{aligned} \tag{2.13}$$

With r being the radius of the local curvature with $1/r = \cos\theta\ \frac{\partial\theta}{\partial x}\big|_t$. Equation 2.13 shows criteria for an equilibrium surface topography by the condition that the surface slope does not change with time $\partial\theta/\partial t|_x = 0$.

Considering the derivative of the angle dependent sputtering yield $\frac{\partial Y(\theta)}{\partial\theta}$ it is zero at normal incidence $\theta_\perp$ and at the angle of highest erosion θ_p due to its minimum and maximum, respectively. The angle dependent sputtering yield curve becomes zero towards grazing incidence $\theta_\parallel$ due to the rising fraction of reflected ions. Depending on its initial local slope and curvature the surface favours to reorientate itself towards one of the above mentioned stable angles [76; 77]. The eroded surface tends to diminish its curvature until it becomes flat. The angular evolution of a surface element can be determined by observing the signs of the derivative of the sputtering

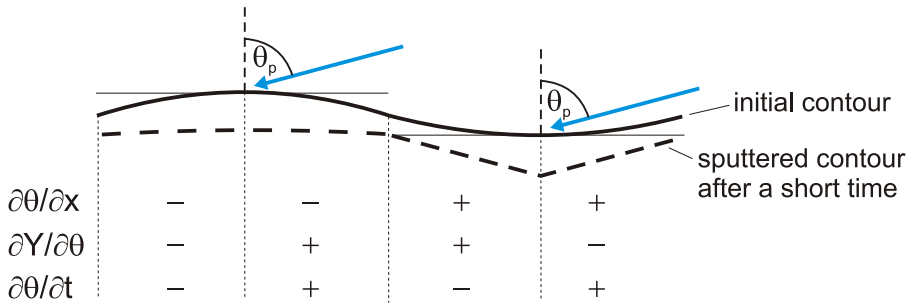

Figure 2.7: Evolution of a curved surface during erosion (see text).

yield curve $\frac{\partial Y(\theta)}{\partial \theta}$ and the curvature $\cos\theta \left.\frac{\partial \theta}{\partial x}\right|_t$ of a specific surface point affecting the sign of $\left.\frac{\partial \theta}{\partial t}\right|_x$. Accordingly, figure 2.7 demonstrates the surface evolution for the special case of ion bombardment at an incident angle of highest erosion θ_p. A convex surface is not stable during sputtering and becomes a flat surface. On the other hand if the surface contour is concave such that $\theta > \theta_p$ they conclude that final equilibrium is reached only if the surface slope is a combination of a local vertical plane $\theta = 90°$ or a local horizontal plane $\theta = 0°$.

2.6 Continuum Modelling

Linear Theories

Since R. M. Bradley and J. M. E. Harper developed a linear partial differential equation in 1988 established as *Bradley-Harper theory*, it was referred to explain the ripple pattern formation mechanism [80]. It predicts the selection of characteristic dominant ripple wavelengths and an exponential pattern growth. Additionally, the theory implies with an increasing angle of incidence ϑ a transition from ripples with the wave vector $\vec{k}$ oriented parallel to ripples with the wave vector $\vec{k}$ oriented perpendicular towards the incoming direction of the ion beam. Based on Sigmund's theory the model implements a curvature dependent sputtering yield which dominates the pattern formation mechanism. The energy distribution deposited by the

impinging ion is assumed to be Gaussian [81]. Thermally activated surface diffusion equation (2.7) is chosen as smoothing mechanism and dominates in their opinion ion bombardment induced diffusion. The theory is limited by a small angle approximation regarding the surface slope.

$$\begin{aligned}\frac{\partial z}{\partial t} = & - \frac{\Phi_{ion}}{n} Y(\vartheta)\cos\vartheta + \frac{\Phi_{ion}}{n}\frac{\partial(Y(\vartheta)\cos\vartheta)}{d\vartheta}\frac{\partial z}{\partial x} \\ & + \frac{\Phi_{ion} a}{n} Y(\vartheta)\left(\Gamma_x(\theta)\frac{\partial^2 z}{\partial x^2} + \Gamma_y(\theta)\frac{\partial^2 z}{\partial y^2}\right) \\ & - \frac{D_s \gamma \Omega^2 \nu}{k_b T}\nabla^4 z\end{aligned} \tag{2.14}$$

Thereby a stands for the average depth of energy deposition and $\Phi_{ion}(x, y)$ is the local ion flux. $\Gamma_x(\theta)$ and $\Gamma_y(\theta)$ govern the dependence of the erosion rate on the curvature of the surface [80] and depend on the local angle of incidence θ, the average depth of energy deposition a and the widths of the distribution $\tilde{\alpha}$ and $\tilde{\beta}$ parallel and perpendicular to the ion beam direction, respectively.

The characteristic feature wavelength arises from a balance between a destabilization invoked by the curvature dependent erosion and the stabilizing effect of surface diffusion.

Even though the Bradley-Harper theory explains aspects of ripple formation qualitatively there are inconsistencies with experiments such as incorrect scaling of the pattern wavelength depending on ion flux, ion energy and temperature and the existence of stable regimes. Therefore this theory was expanded by including higher-order nonlinear expansion terms [24; 82].

The forward-looking work of Norris et al. derives a continuum partial differential equation by considering small length scale craters from individual ion impacts and connecting it with the characteristic scale of pattern formation [83; 84]. Earlier theoretical studies have shown that a small change in the crater shape can lead to substantial changes in the behavior of the macroscopic system [85]. However,

Norris et al. use a crater function which describes the local mass redistribution after a single ion impact. Integrating the crater functions over the locations of several ion impacts and taking into account the responses of nearby ion impact points a nanoscale pattern may be predicted. The crater function itself combines the mechanisms of mass ejection or sputtering and a local mass redistribution. The used formalism is completely general so that e.g. considering only the erosive part of the crater function and inserting Sigmund´s ellipsoidal energy-release mechanism obtained to first order reproduces the results of the Bradley-Harper theory [80; 83]. Focusing solely on redistributive effects of the ion impact craters and inserting singly surface currents due to ballistic atomic drift shows agreement with previous derived diffusion like equations [85; 86]. Recent work identifies the latter mechanism as predominant in the linear regime [87].

Lately Castro and Cuerno presented their hydrodynamic model about *solid flow* which can lead to both smoothing and nanostructuring [41]. The ion induced amorphous surface layer with thickness a_z is described as a highly viscous fluid ($\eta \approx 10^9\,\mathrm{Pa\,s}$). Low energy ion beam erosion creates a large number of defects such as vacancies and interstitial atoms enhancing solid flow artificially by the defect dynamics and accordingly material redistribution. In their consideration ion induced solid flow may act as the only pattern forming mechanism and the erosive contribution is insignificant[1].

The radiation induced viscosity of Si is around fifteen orders of magnitude larger than the viscosity of water. For highly viscous media Stokes flow applies:

$$\rho \frac{\mathrm{d}\mathbf{V}}{\mathrm{d}t} = \nabla \cdot \mathbf{T}_{ij} + \vec{b} = 0 \tag{2.15}$$

The flow of the amorphous layer is assumed to be incompressible $\nabla \cdot \mathbf{V} = 0$, where $\mathbf{V}$ is the velocity field and of stationary thickness. The density ρ of the target

[1]The erosive contribution is incorporated in the solid flow theory solely because of misguiding results in the experimental data, which recently were revised [22; 30; 88].

in the amorphous phase remains almost a constant. $\mathbf{T}_{ij}$ is the stress tensor and $\nabla\mathbf{T}_{ij}$ describes viscous forces acting solely as a shear effect for incompressible flow. At the amorphous-crystalline interface a no-slip condition is taken into account. The ion beam is incorporated as a body force $\vec{b}$ and contains the residual stress created in the target due to ion induced mass redistribution.

The mechanism of solid flow is similar to a liquid flowing down an inclined plane with inclination angle ϑ. In this analogy the external body force $\vec{b}$ replaces gravity. In contrast to gravity the body force is not constant and is larger in those locations where the surface faces the external beam.

The physical origin of the instability for oblique incident ions with $\vartheta > \vartheta_c = 45°$ is the net difference between the force on both sides of an undulation. The amplitude of the undulation grows due to incompressibility and makes it shrink laterally. Thereby the characteristic pattern wavelength Λ is given by:

$$\Lambda = 2\pi\sqrt{-\frac{2\gamma}{\frac{\varsigma}{a_z}\cos(2\vartheta)}} \tag{2.16}$$

with the surface energy γ, the ion induced residual stress ς, and the thickness of the amorphous layer a_z. The theory is able to capture the lack of pattern formation at small incidence angles and the existence of the morphological transition from a flat to a rippled surface by increasing the angle of incidence ϑ. In the low fluence range it predicts the pattern wavelength dependence on the global angle of incidence reasonably [30; 41].

Nonlinear Theory

As some experimental findings could not be explained by the common Bradley-Harper theory the attention was drawn to expand the linear theory by nonlinear terms. In principle the linear theory utilizes a small angle approximation and is sufficient to describe pattern evolution only in the low fluence stage. Therefore nonlinear terms were considered to predict observed phenomena as e.g. the satura-

tion of the ripple amplitude with increasing fluence [89], a temperature independent smoothing mechanism [24] or well-ordered dot patterns [25–27; 90]. The nonlinear models are based typically upon a modified nonlinear *Kuramoto-Sivashinsky* equation [91–93].

However, today there is still disagreement about an adequate linear theory. Therefore, it is less conducive to discuss the manifold possible solutions of nonlinear theories since a comprehensive nonlinear theory has to be based on a coherent linear theory. Furthermore, it is nontrivial to assign physical mechanisms to the considered mathematical terms.

2.7 Modelling Metal Assisted Ion Beam Pattern Formation

In recent years also pattern formation theory has discovered the relevance of multicomponent systems for expanding the opportunities and our understanding of ion beam patterning [94–96]. Even co-deposition situations are now analyzed theoretically [95–97].

Shenoy et al. [94] recommend that the combination of preferential sputtering and a variation in the diffusivity of the target components may lead to a modulation of the height and a decomposition of the alloy within the surface. They show conditions where the topography and composition modulation is in or out of phase. Based on this work Bradley and Shipman advanced the theory to a nonlinear theory which includes also dot pattern formation with hexagonal order as observed frequently experimentally [96].

Moreover, previous work in the field of phase separation during film growth shows that phase separation in a thin surface layer may lead to a composition modulation. Even though from this perspective no erosion is taken into account some relevant conclusions appear. Based on the fundamental work of Cahn on spinodal decomposition in the bulk [98] the theory was modified considering thin film growth [99–102].

The theory of spinodal decomposition describes that the total free energy which includes chemical free energy, gradient energy due to composition inhomogeneity, and elastic energy can be lowered by allowing the components to separate.

The Cahn-Hilliard-type diffusion along the surface as derived by Fukutani is given by [100; 102]:

$$\frac{\partial c}{\partial t} = M_s \nabla^2 \left(\frac{\partial f(c)}{\partial c} - \kappa \nabla^2 c \right) + v_d \quad \frac{c_0 - c}{\delta} \tag{2.17}$$

with c_0 and c being the overall composition of one component and the local composition of a certain phase, respectively. $f(c)$ is the chemical free energy density (potential of phase separation) and κ is the gradient energy coefficient defining the chemical potential $\mu = \left(\frac{\partial f(c)}{\partial c} - \kappa \nabla^2 c \right)$. M_s, v_d, and δ are the surface mobility, deposition rate, and surface diffusion thickness, respectively.

The above examination is valid for deposition experiments [101; 102], simultaneous ion erosion is not taken into account. As the thesis at hand elaborates the influence of metal assisted ion beam patterning on Si the above theory has to be expanded according to the contribution of ion bombardment. We expect that simultaneous ion beam erosion changes the time dependent deposition constant v_d due to additional erosion. Furthermore, the surface diffusion is enhanced by the energy transfer of the ions to the target atoms.

The influence of phase separation on ion beam pattern formation was already used to interpret ion beam induced patterns on Si with simultaneous metal seeding [34; 35].

2.8 Previous Work

First investigations on low energy ion beam erosion as a tool for pattern formation appear at least since 1959 on metals [103; 104]. Whereas patterns were generated and investigated on the micrometer scale in the beginning, in the last decades scanning probe microscopy made ion beam induced patterns on the nanometer scale

accessible.

As mentioned in the introduction, recently it turned out that trace amounts of impurities co-deposited unintentionally during sputtering of silicon influence ion beam pattern formation strongly. The present thesis contributes to the cognitive process of understanding the mechanisms behind ion beam pattern formation in pure and as well metal assisted erosion experiments. From this point of view it is reasonable to itemize previous published work classified into the two mentioned categories. This is not a simple task, since a classification of previous work in pure erosion experiments and experiments affected by the unintentional seeding of impurities is not in every case unequivocal. Nevertheless, to some extent the classification is possible, since some working groups retroactively carried out valuable work by analyzing their samples and the influence of impurities within their setup after the significance of impurities revealed [30; 105–107].

Low Energy Pattern Formation on Si(001)

Ozaydin et al. ascertained that under clean conditions a silicon surface remains smooth after normal incidence 1 keV Ar^+ bombardment [29]. A smooth surface was also found for fluences of $\approx 5 \times 10^{21}$ ions m^{-2} using normal incident 100 eV – 500 eV Ar^+ and 5 keV Xe^+ [35; 108].

In experiments and theory the ion incidence angle was pointed out to be a crucial parameter. Madi et al. systematically varied the angle of incidence and the ion energy to get a pattern overview and framed a phase diagram. Using Ar^+ with energies between 250 eV and 1 keV and for low fluences of $F \approx 3.2 \times 10^{21}$ ions m^{-2} they find a smooth surface for sputtering angles $\vartheta < 50°$, ripples oriented perpendicular for $50° \leq \vartheta \leq 80°$ and parallel for $\vartheta \geq 80°$ to the incoming ion beam[1] [88]. Nevertheless, performing ion energy dependent experiments Vishnyakov and Carter show that even Ar^+ bombardment at an incident angle of $\vartheta = 45°$ leads to ripple

[1]Recently their misguiding experimental results constituting ripple patterns in the angular range $\vartheta \leq 45°$ [22; 30] recently were revised by them [88].

pattern formation if the energy is high enough. Sputtering in the medium energy bombardment range they define a cut off energy between 10 keV and 20 keV [109].

Zhang et al. investigated the ripple rotation from perpendicular to parallel oriented ripples with respect to the projection of the oblique incident 5 keV Xe^+ beam. Analyzing ripple structures in the angular range of $70° \leq \vartheta \leq 85°$ they found the critical angle of ripple rotation to be at $\vartheta_c = 80°$ for fluences of $1 \times 10^{22}\,\mathrm{m}^{-2}$ [110]. Fluence dependent measurements at the critical ripple rotation angle of $\vartheta_c = 80°$ show at a low fluence of $1 \times 10^{20}\,\mathrm{ions\,m}^{-2}$ a ripple like structure composed of elliptic grains with the long axis perpendicular to the ion-beam direction which crosses over to a *tiled roof* pattern found at a fluence of $3 \times 10^{20}\,\mathrm{ions\,m}^{-2}$ [110]. Regarding the roughness they find two ion fluence regimes. Below an ion fluence of $1.5 \times 10^{20}\,\mathrm{ions\,m}^{-2}$ the roughness increases exponentially $\sigma \sim e^{0.27\,\Phi}$ while at fluences above the given value the roughness increases by a power law $\sigma \sim \Phi^{0.34}$ [110]. Fluence dependent measurements were also performed by Keller et al. [111] with 300 eV – 500 eV Ar^+ and an incident angle of $\vartheta = 67°$. The quality of ripple patterns strongly depends on the applied ion fluence. The pattern defect density passes through a minimum with sputtering time. At high fluences they observe an evolving superposed quasi-periodic pattern, which is oriented parallel to the beam direction with a larger spatial periodicity of $\Lambda \approx 900\,\mathrm{nm}$ and a lower degree of order [112]. Furthermore, the order and regularity in the ripple morphology may be enhanced by sputtering a present ripple pattern subsequently parallel to the ripple ridges with grazing incident ions. With increasing fluence the ripples become longer and more pronounced [113].

Fluence dependent measurements were also performed by Lewis et al. [114]. At an incident angle of $\vartheta = 50°$ and Ar^+ energy of 8 keV a ripple pattern evolves while the critical fluence for the arising ripple pattern can be estimated at a relative high fluence of $\approx 3 \times 10^{22}\,\mathrm{ions\,m}^{-2}$. The wavelength increases with fluence and a pattern coarsening becomes apparent.

The orientation of single-crystalline Si surfaces has no influence on the pattern

morphology of the amorphous surface and crystalline subsurface. Using substrates with an intentional miscut from the [001] direction and a [111] oriented wafer Hanisch et al. showed that the ion beam induced ripple wavelength, pattern amplitude, and the degree of order are independent of the surface orientation [115].

The other way round starting from a rough prepatterned surface Frost et al. pointed out ion beam erosion to be convenient for surface smoothing. By sputtering Si(001) with a 500 eV Ar^+ beam of small divergence at an incident angle of $\vartheta = 45°$ they observed a smoothing an from initial roughness of $\sigma \geq 2\,\text{nm}$ to $\sigma \leq 0.2\,\text{nm}$. Thereby, surface irregularities with small wavelength are smoothed out rapidly, while large wavelengths require longer sputter times [116].

Carter et al. investigated the influence of the ion species in the pattern formation mechanism. The experiments were performed with a focused static ion beam in the medium ion energy range and an incident angle of $\vartheta = 45°$. While at room temperature 20 keV Ne^+ bombardment of Si(001) no patterns form, 20 keV Ar+ and Xe^+ bombardment leads to a faceted ripple structure. According measurements of the ratio of implanted to incident ions of Ne, Ar, and Xe in silicon show that the fraction decreases with increasing ion mass from 0.6, 0.4 to 0.3, respectively [117]. However, a higher ion mass promotes pattern formation and the mass dependent differences suggest a correlation with the cascade geometry. Carter et al. suppose that the defect concentration increases with the ion mass and thus defect migration and flow processes lead to the species dependence of pattern formation [117].

Even though most investigations were carried out on experiments at room temperature nevertheless temperature dependent measurements are highly interesting inasmuch as some theories attach great importance to this fundamental parameter and smoothing mechanisms as diffusion and viscous flow are temperature dependent.

Carter et al. investigated that sputtering at temperatures below room temperature in the medium ion energy range promotes pattern formation for the investigated ion species Ne^+, Ar^+, and Xe^+ [117]. While in the case of 20 keV Ne^+ sputtering with $\vartheta = 45°$ at temperatures above 200 K no patterns form, a well developed ripple

pattern evolved at 120 K. Further, it was discovered by sputtering silicon with 20 keV Xe^+ and $\vartheta = 45°$ that at low temperatures the initiation of pattern formation sets in at lower fluences [117].

Quite some observations of temperature dependent ion beam erosion experiments with oblique incident ions refer to elevated temperatures in the crystalline regime [118–120]. Erlebacher et al. [118] use 750 eV Ar^+ with oblique incidence and the ripple pattern wavelength increases in the temperature range between 750 K and 870 K which is interpreted as increase in the surface diffusion of the mobile surface atoms. While Erlebacher et al. find no increasing wavelength on Si(001) with fluence at temperatures ≈ 855 K, Brown et al. [120] find at ≈ 970 K an increasing wavelength on Si(111) with the ion fluence. These findings let one assume that at high temperatures where the eroded surface keeps being crystalline during ion bombardment the crystal orientation of the sample surface might play an important role. In contrast by sputtering in the medium ion energy range Carter reveals that the wavelength appears to be temperature, and almost ion species, independent. They use oblique 40 keV Xe^+ ions in the temperature range from 100 K – 700 K where the near surface ranges from amorphous to largely crystalline during erosion. Thereby the pattern amplitude decreases with increasing temperature [117; 121].

Low Energy Pattern Formation on Si(001) with Impurities

Co-deposition of trace amounts of foreign species during ion erosion has been found already long time ago to give rise to microstructure formation [122; 123]. Robinson and Rossnagel [124; 125] seeded Fe and Cu at elevated temperatures during ion erosion of Si and found a microstructured surface covered with cones with high slopes and spacing in the range of 500 nm. Currently co-deposition is used as a tool for surface texturing on nanometer scale [32; 34; 126].

As already mentioned, recently some observations pointed out that trace amounts of unintentionally deposited impurities influence pattern formation. Mo co-sputtered from sample clips during ion erosion was found to foster dot formation at normal

incidence [29; 30; 127; 128]. The ion flux and fluence were found to affect the amount of Mo and Fe deposited on the sample from the ion source and thereby to change normal incidence dot and hole patterns [105; 129; 130].

Also prior to this realization regular nanodot patterns were observed on silicon but the phenomenon was not associated to the presence of impurities. Normal and slightly off normal incidence noble gas ion erosion with energies up to a few keV and at temperatures in the amorphization regime led to pronounced patterns [131–136]. Gago et al. [137] pointed out that with fluence the average height of the nanodots, the surface roughness and the surface nanodot density reach an essentially constant value. Another class of exemplary patterns are ripple ones with the ripple wave vector $\vec{k}$ parallel to the ion beam azimuth. The most regular ripples evolved for slight off-normal conditions with $\vartheta \approx 15°$ using noble gas ions with energies up to a few keV [136; 138–140].

Other measurements on Si established a threshold of impurity concentration before pattern formation initiates. While Zhou et al. [141] estimated a necessary stationary metal incorporation above $\approx 8 \times 10^{18}$ Fe m^{-2} for normal incidence 1.2 keV Ar^+ sputtering Zhang et al. [35] rate the onset of dot and ripple formation in the range between 2×10^{19} and 6×10^{19} Fe m^{-2} for normal incident 5 keV Xe^+. These varying results indicate that the threshold might depend on ion energy and species.

An extensive ion beam patterning study was published by Ziberi et al. [135; 136; 138–140; 142] while the influence of impurities on these measurements was precisely characterized afterwards [106; 107]. Using a divergent ion beam metal is co-deposited on the Si sample due to simultaneous erosion of a cylindrical-shape steel lining[1] Increasing the angle of incident ions and thus increasing the sputtering yield the steady state concentration of the co-deposited metal decreases [106].

Contrary to pure ion beam erosion experiments on Si, in the presence of impurities patterns form also in the case of $0° \leq \vartheta \leq 40°$. These ripple and dot

[1]The ion beam divergence and thus the impurity flux is proportional to the ion source grid acceleration voltage.

patterns generated by the use of near normal incident ions and simultaneous metal co-deposition show an exceptionally high regularity. For $40° \leq \vartheta \leq 60°$ likewise a smooth surface is found [136]. A pattern transition from ripples to dots was observed for 1 keV – 2 keV Xe^+ by increasing the angle of incidence in the range of $20° \leq \vartheta \leq 40°$ as well as by reducing the ion beam divergence. Thereby a decrease of the characteristic pattern wavelength from $\Lambda \approx 70\,\text{nm}$ to $\Lambda \approx 40\,\text{nm}$ and a decrease in roughness from $\sigma \approx 2\,\text{nm}$ to $\sigma \approx 0.2\,\text{nm}$ was observed by increasing the angle of incident Xe^+ from $\vartheta = 5°$ to $\vartheta = 40°$ [136]. From this it follows that by reducing the impurity concentration the patterns are less pronounced.

As the pattern wavelength is a significant feature the exploration of its dependence on several parameters was determined. By raising the Kr^+ ion energy from 800 eV to 2 keV an increase of the ripple wavelength from $\Lambda \approx 40\,\text{nm}$ to $\Lambda \approx 65\,\text{nm}$ was found [136]. Furthermore, the variation of the 2 keV Xe^+ ion flux between $80\,\mu\text{A/cm}^2$ – $300\,\mu\text{A/cm}^2$ has no influence on the ripple pattern wavelength [140]. Fluence dependent measurements show that the wavelength of ripple structures generated with slightly off-normal incident ions remains constant with increasing ion fluence while the lateral ordering increases [136; 138; 139]. In the initial ripple pattern formation process the surface roughness grows exponentially with fluence until it saturates at $\sigma \approx 1\,\text{nm}$ at a fluence of $\approx 1 \times 10^{22}\,\text{ions}\,\text{m}^{-2}$ [136]. Finally, it should be mentioned that less regular ripples were generated with oblique incident ions which coarsen with increasing fluence [137].

For ion species with lighter mass than the target, usually no structures are observed. Once structures form, their characteristics like pattern wavelength, regularity, homogeneity and height are independent on the ion species used [136; 138].

Furthermore, the dependence of the pattern wavelength on the temperature during ion beam erosion experiments with metal co-deposition was evaluated [127; 129; 132]. Ozaydin-Ince et al. [127] seeded the Si(100) surface with Mo during normal incidence 500 eV Ar^+ bombardment. From room temperature up to 720 K nanodots form. The pattern amplitude and accordingly the roughness trends to decrease from

$\sigma \approx 0.7\,\text{nm}$ to $\sigma \approx 0.3\,\text{nm}$ as the substrate temperature increases. It is suggested that the primary effect of thermal energy is promoting surface smoothing rather than increasing the diffusion of seed atoms to form protective clusters. Raising the temperature to 920 K the surface remains crystalline. Nanodot formation is not clearly visible and the seeding has little effect on the surface evolution.

A similar trend with temperature was observed by Gago et al. who as well investigated nanodot patterns [132]. Retroactively the formation of dots in their experiments was assigned to Fe and Mo impurities present during erosion [105; 129]. In their measurements the temperature is irrelevant below 400 K; a progressive decrease in the dot amplitude and characteristic pattern wavelength was found between 400 K and 500 K [132].

Sánchez-García et al. characterized the temperature dependence for nanohole patterns on Si which were generated by normal incident 1 keV Ar^+ and simultaneous Fe and Mo deposition stemming from the ion source itself and the sample surroundings. Below a threshold temperature of 350 K the nanohole pattern becomes denser thus the characteristic pattern wavelength decreases with increasing temperature. For temperatures above 350 K the nanohole pattern disappears [129].

Zhou et al. performed steel co-sputter deposition experiments with normal incident 1.5 keV Ar^+ on Si(001) at $\approx 770\,K$. The resulting surface was covered with unordered densely distributed cones with an average height of $\approx 350\,\text{nm}$ and width of $\approx 250\,\text{nm}$. The cones are crystalline with metal-enriched apexes and due to their high aspect ratio the light absorption of the surface is enhanced by more than 25% [143].

Temperature Dependent Iron-Silicide Formation

Figure 2.8 shows the Fe-Si phase diagram and its complexity (modified from [144]). Depending on the alloy composition and temperature silicon forms with Fe stable silicides such as Fe_3Si, Fe_2Si, $FeSi_2$, Fe_2Si_5 etc.

Different observations were made by annealing Si(001) with a deposited thin film

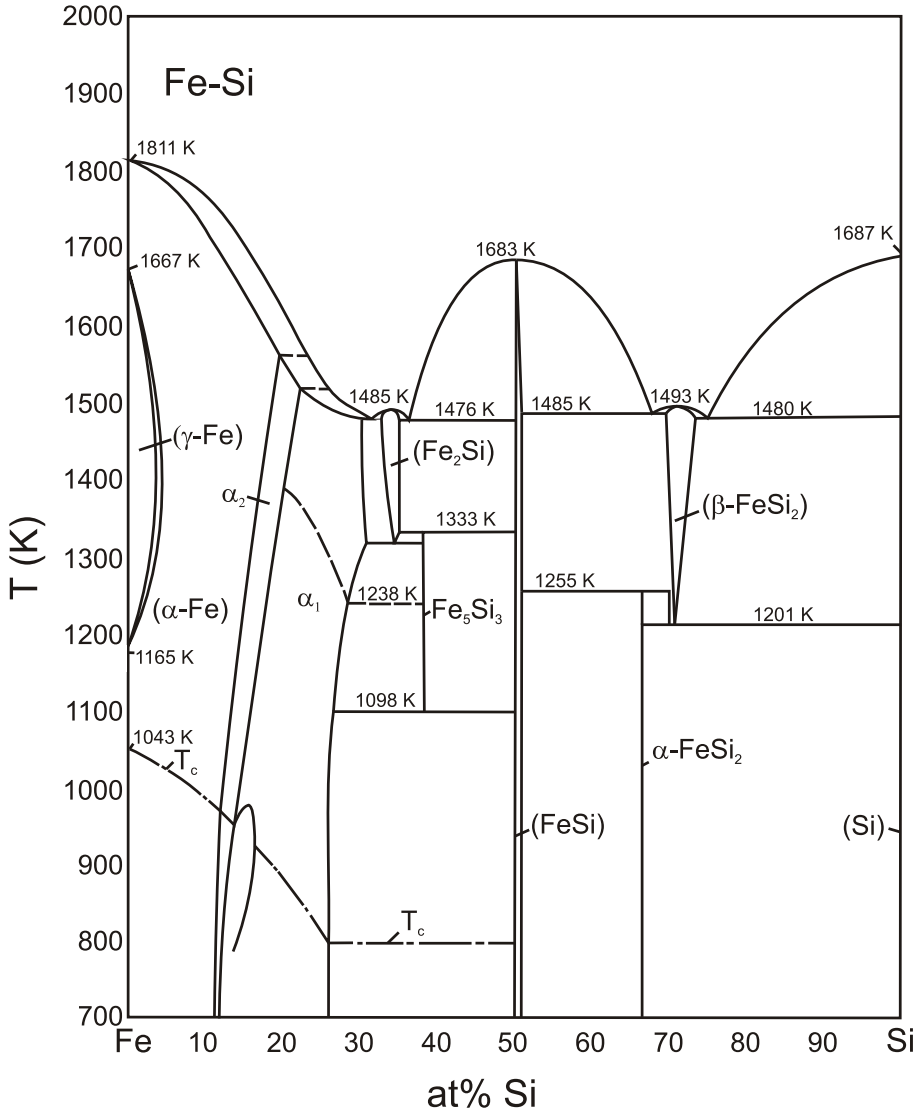

Figure 2.8: Fe-Si Phase diagram (modified from [144]).

of Fe. Gallego et al. have annealed 30 monolayers of Fe on Si(001) and made Auger electron spectroscopy under ultra high vacuum conditions [145]. The interface composition changed depending on the sample temperature. While in the temperature range of $T \approx 350\,\mathrm{K} - 450\,\mathrm{K}$ Fe_3Si was found, the silicide composition changed to FeSi in the temperature range of $T \approx 620\,\mathrm{K} - 720\,\mathrm{K}$.

However, it seems there is a strong dependence on the Fe layer thickness. Zhu et

al. performed similar experiments with a thin film of Fe with a thickness less than 10 monolayers and did not find the Fe_3Si phase [146]. In their studies FeSi forms while heating to temperatures of about 670 K and is stable up to 800 K. $FeSi_2$ forms at about 820 K and is stable up to 940 K.

The mentioned publications might be useful for orientation which iron-silicides form depending on the amount of deposited Fe on Si at certain temperatures. However, predicting the iron-silicide composition during sputtering an Fe-Si compound target at different temperatures is more complex. Due to the additionally ion induced energy impact and the associated thermal spike as well as the ion induced intermixing and diffusion the resulting iron-silicide composition might differ.

3 Experimental

3.1 UHV System *Athene*

The experiments were performed in the ultra high vacuum system *Athene* with a base pressure $p < 6.0 \times 10^{-11}$ mbar. The notable low pressure was established by two turbo-molecular pumps (1) an ion getter pump (2) a liquid N_2 cooling trap localized in the rear chamber walls (3) and a Ti sublimation pump (not shown in sketch). The manoeuvrable and rotatable manipulator (4) allows one to position the sample precisely relating to the equipment attached to the chamber. The Si sample sits on small sapphire balls and is fixed with tungsten clips onto a molybdenum sample holder (iii). A heating stage is realized by a tungsten filament positioned below the sample surrounded by a focusing cup in the center of the base plate. Applying a high voltage between filament and sample leads to electron bombardment and thus heating of the sample. The heating stage allows outgassing and flashing of the sample as well as experiments at elevated temperatures. Otherwise the sample may be cooled with compressed air, liquid N_2 or liquid He attached to the cryostat. In order to maximize the thermal conductivity the base plate (iv) made of copper is connected via tempered Cu braids to the cryostat cold finger (v) facilitating sample temperatures down to $T \approx 40\,\mathrm{K}$. The sample temperature may be measured in a twofold manner; at low temperatures via a moveable type K thermocouple which is exposed to the sample occasionally (ii) and at elevated temperatures by an infrared pyrometer (5).

The sample surface is positioned in the axis of rotation. The angular adjustment of the sample orientation in particular towards the electron beam evaporator (6) and (6´) and towards the ion source (7) is within one degree of accuracy. For the

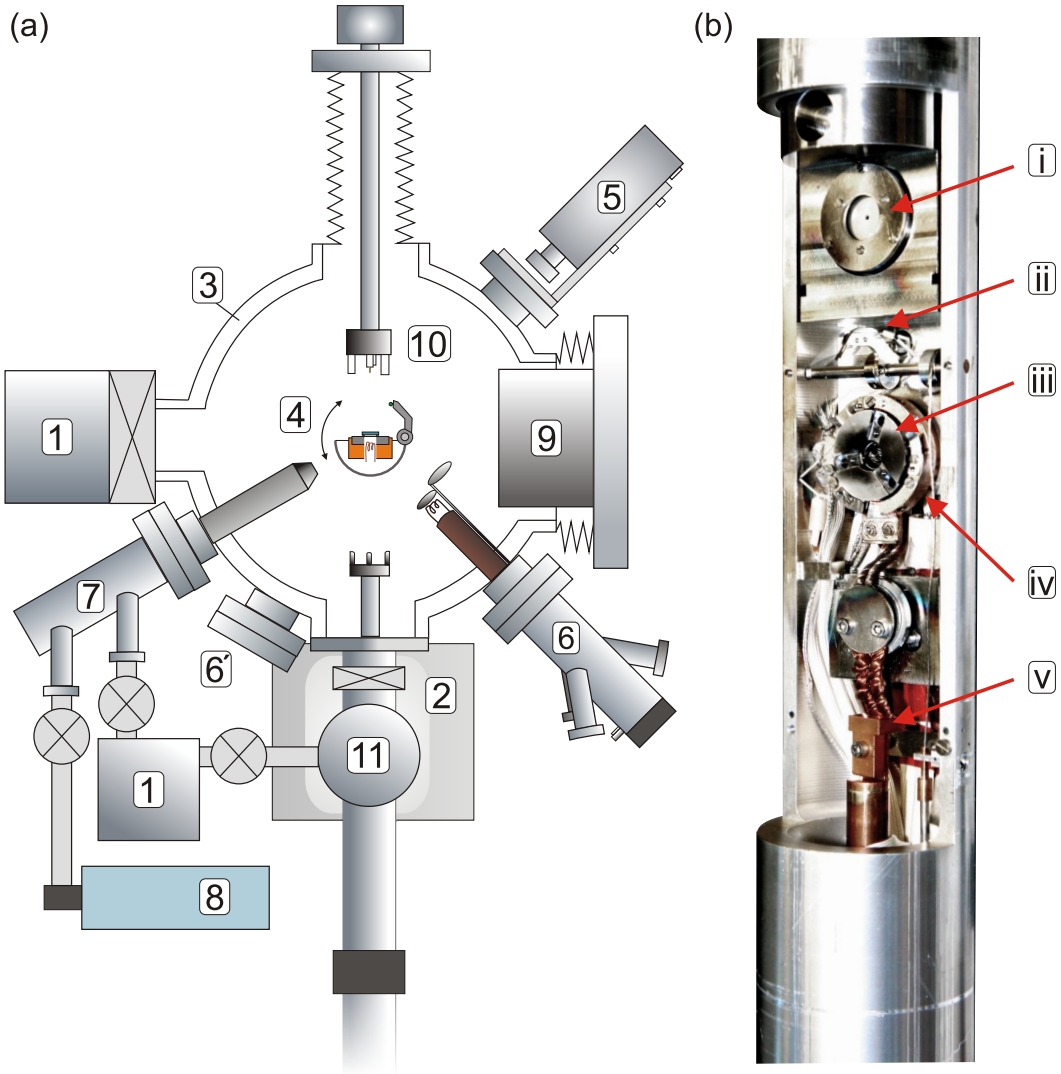

Figure 3.1: (a) Schematic cross-sectional sketch of the variable temperature scanning tunneling microscopy apparatus *Athene* (modified from [147]). (1) Turbo-molecular pumps, (2) ion getter pump, (3) liquid N_2 cooling trap, (4) rotatable manipulator with sample holder, heating stage and temperature measurement system, (5) pyrometer, (6) and (6´) mounting positions of the electron beam evaporator, (7) ion source, (8) noble gas reservoir, (9) LEED system, (10) STM, (11) load lock. (b) Rotatable manipulator with (i) Faraday cup, (ii) moveable type K thermocouple, (iii) sample holder, (iv) base plate and (v) cryostat cold finger.

erosion experiments a *KREMER IQ100* fine focus differentially pumped ion source (7) was used with Kr as sputter gas (8). The ion beam current is measured by a Faraday cup (i) within the nA range. Mounted on the manoeuvrable manipulator the Faraday cup may be moved precisely into the sample position.

For surface analysis the apparatus is equipped with a low energy electron diffraction (LEED) system (9) and a scanning tunneling microscope (STM) (10). As durable STM tip we use a pure Ir wire of 0.25 nm diameter which was electrochemically etched producing a sharp ended tip [147]. A load-lock (11) for sample transfer allows one to perform additional *ex situ* measurements with the specifically prepared sample.

3.2 *ex situ* Measurement Methods

After preparation and imaging the samples by in situ STM, additionally, the sample topography was analyzed by *ex situ* by atomic force microscopy (AFM), scanning electron microscopy (SEM), and by a compact phase-shifting interferometer.

The structure of surface patterns was studied by high-resolution transmission electron microscopy (TEM). For the cross-sectional imaging a *Titan 80-300* electron microscope equipped with a field emission gun working at 300 keV and an image corrector to minimize spherical aberrations was used.

For the high resolution TEM measurements, a carbon layer of a few hundred nm was evaporated locally on selected positions. Right there lamellae were cut out of a sample using a focused ion beam (FIB) system (*ZEISS NVision 40*). After its fabrication each lamella was subsequently glued onto a copper grid and thinned using a 5 keV Ga^+ beam.

The surface chemical composition was analyzed with high lateral resolution by electron energy loss spectroscopy (EELS) and energy dispersive X-ray spectroscopy (EDX) within the dedicated scanning TEM. The scanning mode of the TEM allows the measurement of EELS line scans along a defined path.

Further analysis of the surface chemical composition was done by time-of-flight secondary ion mass spectrometry (ToF-SIMS) using 15 keV Ga^+ and 250 eV O_2^+.

The crystal lattice structure was analyzed by grazing incidence X-ray diffraction (GI-XRD). The measurements were performed by an optimized X-ray laboratory setup using Cu-K_α radiation with a relatively high flux and a beam size of 200 µm. The scattered X-ray signal was detected using a position sensitive detector.

3.3 Sample Preparation

For our experiments we use polished Si(001) wafers with a diameter of 9 mm. The tolerance within the surface orientation is less than $\pm 0.5°$.

After removal of the protective adhesive tape, the Si sample was mounted with cleaned plastic tweezers to the pure molybdenum sample holder. The Si sample lies on three small sapphire balls and is fixed at its edges to the sample holder through three tungsten leaf springs. Prior to insertion to the load lock, dust was blown off with a He gas beam. Samples cleaned this way display a roughness ≤ 0.2 nm, after removal of the native oxide through a normal incidence ion fluence of $F = 2 \times 10^{20}$ ions m^{-2}. Note that fluxes and fluences given are values on the sample plane and not in a plane normal to the ion beam, as frequently specified. In general in the presented experiments the sample is sputtered without prior outgassing, flashing, and removal of the thin native oxide layer.

For our erosion experiments we use Kr as sputter gas. It was found out that ion beam pattern formation on Si is practicable with several ion species. To avoid additional effects of reactive sputtering we chose a noble gas. Furthermore there is a trend that heavy ions as Kr^+ and Xe^+ generate a larger pattern amplitude compared to Ne^+ and Ar^+ [117; 136; 138]. The matter of expense makes Kr^+ favourable in comparison to Xe^+.

Pure Erosion Experiments of Silicon

The samples were exposed to a low energy Kr^+ focused ion beam with full width at half maximum $\approx 1\,\mathrm{mm}$ scanned over a sample area of about $4\,\mathrm{mm} \times 4\,\mathrm{mm}$ resulting in a time averaged ion flux Φ_{Kr^+} in the range of $4 - 7 \times 10^{17}\,\mathrm{ions\,m^{-2}\,s^{-1}}$. Due to differential pumping of the ion source during ion exposure the working pressure was $p < 9.0 \times 10^{-8}\,\mathrm{mbar}$. After ion exposure the pressure dropped quickly into the $10^{-11}\,\mathrm{mbar}$ range and imaging by STM was performed subsequently.

In figure 3.2 the ion beam scan area is made visible by sputtering a plate coated with tantalum oxide.

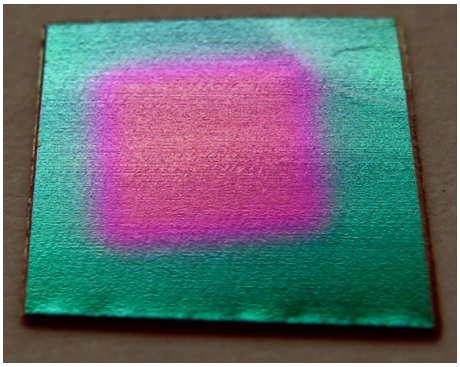

Figure 3.2: A plate coated with tantalum oxide after sputtering with normal incident $2\,\mathrm{keV}$ Kr^+ within a scan area of $4\,\mathrm{mm} \times 4\,\mathrm{mm}$.

Erosion thins out the initial green coloured film so that according to erosion time the colour shifts over blue to violet due to interference at thin films. From figure 3.2 it is evident that the scan area of the ion beam is homogeneous with sharp borders where the ion flux drops rapidly. Measurement by the moveable Faraday cup reveals that within the entire scan area the uniformity of the ion flux is better than 10 %, within the area 0.5 mm away from the edges of the scan area it is better than 5 %.

Co-sputter Deposition

For the co-sputter deposition experiments, a piece of angle iron made from stainless steel (Fe 84% and Cr 13%) was mounted on the Si(001) sample by clamping it together with the Si wafer under two of the three tungsten leaf springs (see figure 3.3). The stainless steel piece exposed an area 1.4 mm high and 6.0 mm wide to the ion beam, vertical with respect to the Si sample. For reproducibility and prior to each experiment, the stainless steel piece received a finish with P180 sand paper and supersonic rinsing in propanol.

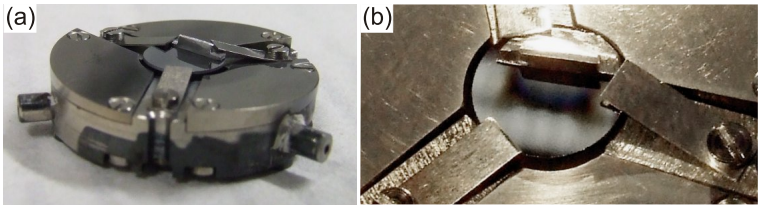

Figure 3.3: (a) Sample holder with Si wafer with a mounted steel plate. (b) Detail of sample after a co-sputter deposition experiment at a temperature of 660 K.

For brevity we will refer to the co-deposited material in text and figures frequently as "Fe". A 2 keV Kr^+ ion beam with a full width at half maximum of ≈ 1 mm was then scanned over the sample and the steel target resulting in simultaneous erosion and metal deposition on the Si sample. The ion beam was impinging at an angle $\vartheta = 30°$ with respect to the surface normal onto the Si sample and with an angle $\vartheta_t = 60°$ onto the stainless steel target [compare figure 3.4].

The scanned area was 4 mm in the direction parallel to the stainless steel plate. In the direction along the x-coordinate as indicated in figure 3.4 the ion beam was covering the exposed area of the stainless steel piece and a distance of almost 6 mm on the sample. Without the stainless steel piece the scanned area would have been from $x = -1.2$ mm to $x = 5.8$ mm. The time averaged flux of primary Kr^+ ions arriving at the Si sample was $\Phi_{Kr} = 3.4 \times 10^{17}\,\mathrm{ions\,m^{-2}\,s^{-1}}$. Prior and after each

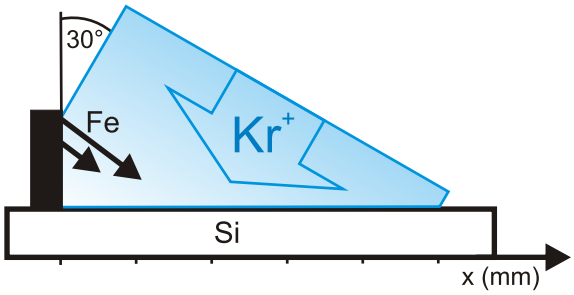

Figure 3.4: Sketch of the sputter co-deposition setup (see text).

experiment, the ion flux was checked by the Faraday cup. The ion fluence to the sample was only $F = 5.9 \times 10^{21}\,\mathrm{ions\,m^{-2}}$ but still sufficient to guarantee pattern development. The working pressure was $p < 1 \times 10^{-7}\,\mathrm{mbar}$ and after ion exposure, the pressure dropped quickly into the $10^{-11}\,\mathrm{mbar}$ range.

Co-evaporation

We also performed co-evaporation experiments using the same stainless steel material as for sputter co-deposition. The ion species, energy, fluence and flux were identical to the ones used for co-sputter deposition. In these experiments, no stainless steel plate was mounted on the Si sample. Instead, stainless steel was co-evaporated from an e-beam evaporator during ion exposure.

The electron beam evaporator was calibrated through a quartz crystal micro balance in a separate high vacuum chamber before mounting it to the UHV system *Athene*. Figure 3.5 shows the evaporation rate which was controlled through the evaporation temperature measured by a thermocouple directly attached to the evaporating stainless steel plate. The amount of co-evaporated material is characterized by the atom-to-ion arrival ratio $\Phi_{\mathrm{Fe}}/\Phi_{\mathrm{Kr}}$.

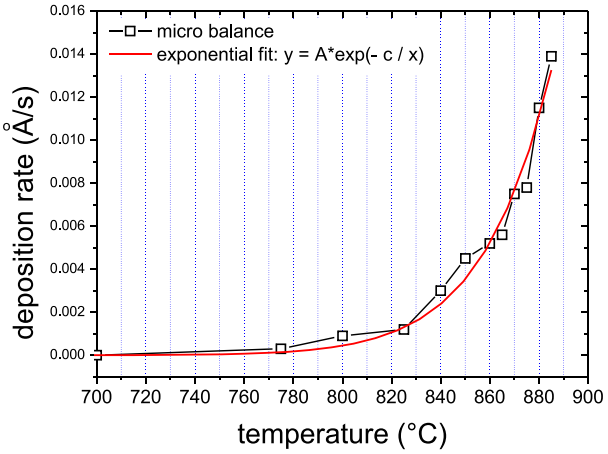

Figure 3.5: Calibration curve for the electron beam evaporator.

3.4 Data Evaluation

Quantitative STM and AFM image analysis was conducted by the computer program WSxM [148].

Colour Scale

In this work for all STM and AFM images the *prodas.lut* colour scale presented in figure 3.6 is used.

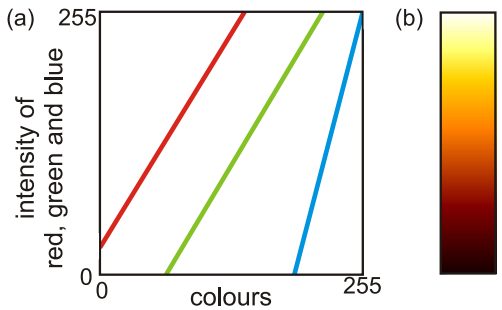

Figure 3.6: (a) Parameters for the colour scale. (b) Resulting colour scale used for STM and AFM images.

Figure 3.6(a) displays that the red, green and blue colour intensity curves grow linearly within the colour space with height. Anyhow, their relative shift leads to a non-linear colour scale since the total brightness is additively composed of the individual colours [figure 3.6(b)].

To show images with a maximum contrast the overall surface height of an image is adjusted to the colour space of the colour scale. Within some image compilations it is desirable that the image corrugation Δz of several images is comparable. Therefore, a fixed Δz (adapted to the image with highest corrugation) is used for the images to be compared. For a well-balanced image the mean value of the image height $\langle h \rangle$ has to be centered within the colour scale which is done by shifting the *user z scale offset* in the program as follows:

$$user\ z\ scale\ offset = \langle h \rangle - \frac{\Delta z}{2} \tag{3.1}$$

Surface Roughness Estimation

A measure for the surface roughness is the root mean square roughness which is defined by the vertical deviations of each surface point from the average surface height. The roughness of a STM or AFM image with $N \times M$ pixels is commonly calculated as follows [149]:

$$\sigma = \sqrt{\frac{1}{(N-1)(M-1)} \sum_{i=1}^{N} \sum_{i=1}^{M} (z_{ij} - \langle z \rangle)^2} \tag{3.2}$$

In general for roughness analysis at first a global plane substraction was applied from the original STM or AFM data; after that a flatten process was carried out by subtracting the average of each line in the image. Images including partial highly rough features on a flat surface were flattened by discarding the rough features (command: *flatten using paths* [148]). Anyhow, after applying the flatten filter also the rough features were incorporated in the final roughness estimation.

Facet Analysis

The facet analysis of a patterned Si surface was done by evaluating STM and AFM image data. Topography images showing facet structures were manipulated by the SPM-analysis software WSxM [148]. Applying a global plane subtraction of an SPM image was necessary to adjust the global normal of the surface. The facet slope was analyzed manually. Thereby surface profiles aligned parallel to the projection of the ion beam onto the surface were evaluated taking solely into account the linear range with steepest slope of the facet gradient. Figure 3.7 shows exemplary how the range of highest slope was estimated. Only profiles aligned perpendicular to a facet ridge were evaluated.

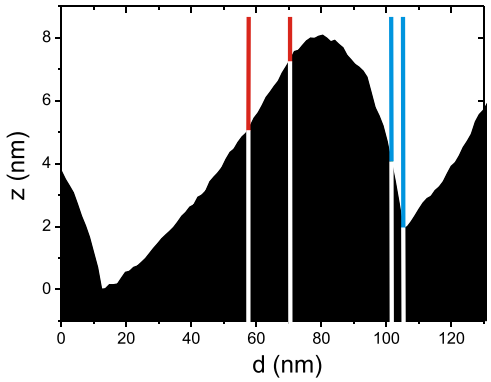

Figure 3.7: Exemplary evaluation of the facet slope. The linear range of highest slope is considered only as shown by the limiting red and blue lines on the flat and steep facet, respectively.

Estimation of Collision Parameters

Calculations of the ion incidence angle dependent sputtering yield for Si, Ag, Pd, Fe and Fe-Si compounds as well as differential energy and angular distribution calculations over the polar emission angle for sputtered atoms and reflected ions were performed with TRIM.SP (program version: November 1995) [57; 150] (see section 2.2).

The data for angular distribution diagrams over the polar emission angle of backward sputtered particles, backscattered projectiles as well as backscattered energy of projectiles were extracted from the according matrices "azimuthal angle versus polar angle in cos-intervals". The data for the angular distribution of the energy of backward sputtered particles was extracted and added up from the according matrices "energy versus polar angle in cos-intervals" and then averaged over the number of particles passing through each solid angle element. All presented data points are positioned in the center of the interval of each solid angle element.

Moreover, we used parameters calculated by TRIM.SP for the comparison of our results with the Bradley-Harper theory [80]. The function Γ_x depends on the local angle of incidence θ, the average depth of energy deposition a and the widths of the distribution $\tilde{\alpha}$ and $\tilde{\beta}$ parallel and perpendicular to the ion beam direction, respectively [80]. We estimated a, $\tilde{\alpha}$, and $\tilde{\beta}$ by TRIM.SP using the mean penetration depth for the incoming ions as a, its straggling as $\tilde{\alpha}$ and the mean lateral spread as $\tilde{\beta}$.

4 Ion Beam Pattern Formation on Si(001)

4.1 Ion Beam Induced Amorphization of Si(001)

Introduction

The ion beam induced amorphization of Si depending on the ion fluence was previously investigated by Bock et al. who performed LEED measurements on Si(111) after ion bombardment with 100 eV – 3 keV Ar^+ ions. They found that the ion fluence at which Si becomes entirely amorphous decreases with increasing ion impact energy. For 2 keV Ar^+ ions on Si(111) the fluence required for amorphization is about 1.6×10^{18} ions m^{-2} [50]. To assure the amorphization at very low fluences for our experiments we verified their findings by sputtering a Si surface with 2 keV Kr^+ ions at an incident angle of $\vartheta = 30°$.

Results

Figure 4.1 demonstrates the ion beam induced amorphization of a flashed Si surface by STM and LEED measurements. Figure 4.1(a) shows Si terraces with a 2×1 reconstructed Si surface after a flash at $T \approx 1470$ K for 10 s. The dimer rows switch their direction by 90° at every adjacent terrace indicating monoatomic step edges. The according LEED image authenticates the 2×1 reconstruction. Figure 4.1(b) and (c) display the same sample after an ion fluence of $F \approx 3.2 \times 10^{18}$ ions m^{-2} at a scale of 150 nm × 150 nm and 30 nm × 30 nm, respectively. The above ion fluence equates approximately to the number of atoms contained in half of a Si(001) layer.

No crystallinity is found neither in the STM images nor in the according LEED image [inset figure 4.1(b)].

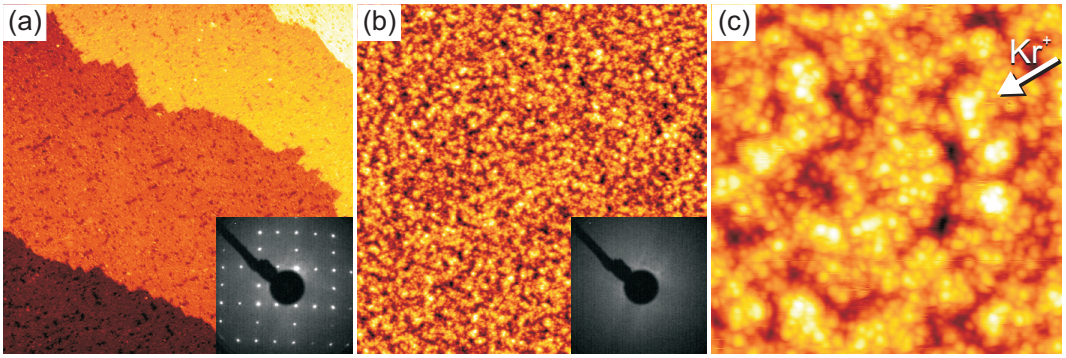

Figure 4.1: STM images of Si(001) before and after erosion with 2 keV Kr^+. (a) Flashed Si(001) surface. Inset shows the LEED image recorded at 110 eV of the Si(001) surface reconstruction. (b) and (c) show the same sample after 2 keV Kr^+ bombardment with a fluence of $F \approx 3.2 \times 10^{18}$ ions m^{-2} at a global incident angle of $\vartheta = 30°$. The inset of (b) displays the LEED screen with a vanished pattern. The image sizes are for (a) and (b) 150 nm × 150 nm and for (c) 30 nm × 30 nm. The image corrugation Δz is in (a) 0.4 nm (b) 0.8 nm and in (c) 0.8 nm. The white arrow in (c) indicates the incoming direction of Kr^+ for the eroded surface displayed in both (b) and (c).

4.2 Ion Beam Incidence Angle Dependence

Introduction

Ion beam erosion experiments depending on the *global* angle of incidence ϑ give information about angular ranges where under ion bombardment the surface becomes stable or unstable. As described in section 2.8 the experimental results in this regard differ considerably.

As the idea came up that the observed irreproducible results in different laboratories originate from trace metal surface contamination [29], we present in the following angle dependent erosion experiments on Si under highly pure conditions.

Results

The dependence of the surface morphology on the global angle of incidence ϑ after ion bombardment is shown in figure 4.2. For global incident angles in the range of $0° \leq \vartheta \leq 55°$ no patterns form and the roughness remains very low with $\sigma \approx 0.2\,\mathrm{nm}$ [compare figures 4.2(a)–4.2(d)]. The according insets show the amorphized surface

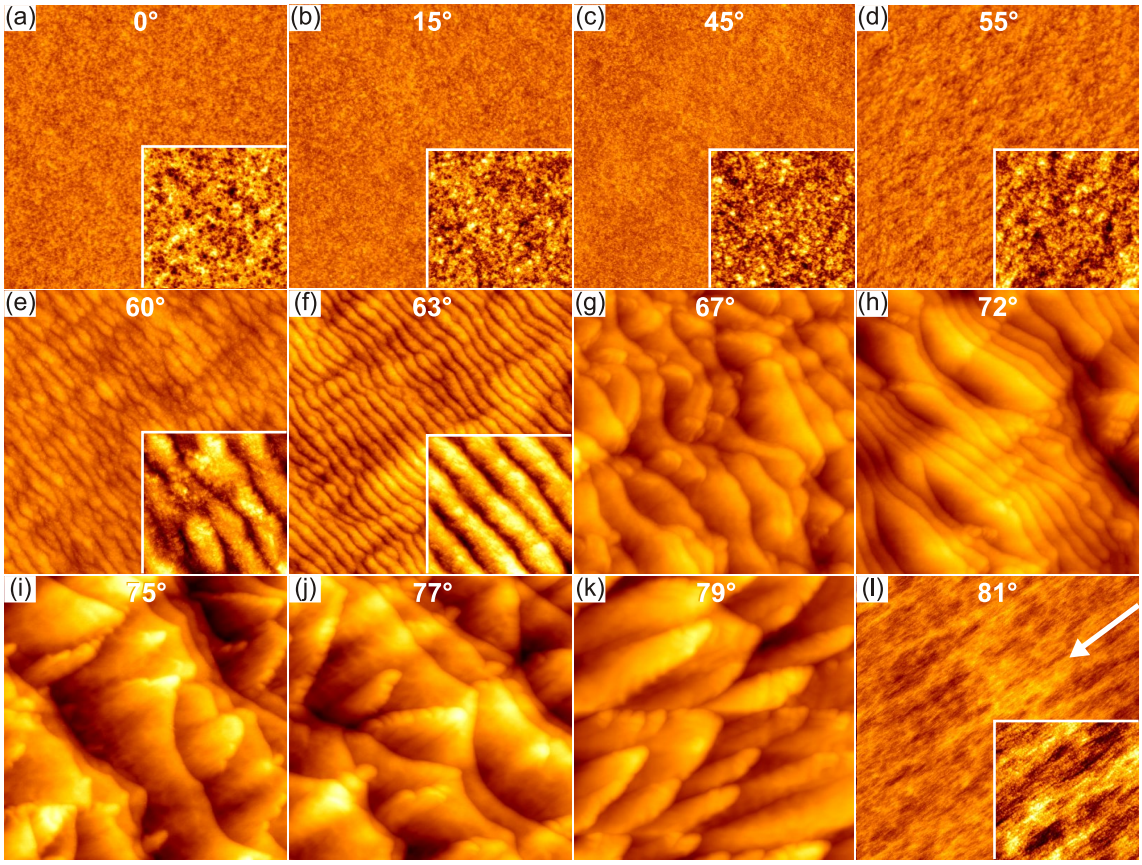

Figure 4.2: STM images of Si(100) after erosion and 2 keV Kr^+ with fluences $F \approx 1 \times 10^{22}\,\mathrm{ions\,m^{-2}}$ at 300 K. The angle of incidence ϑ with respect to the surface normal is noted at the top of each image border. The image size is always $1\,\mu\mathrm{m} \times 1\,\mu\mathrm{m}$, (insets $200\,\mathrm{nm} \times 200\,\mathrm{nm}$). The white arrow in (l) indicates the ion beam azimuth for images (b)–(l). The corrugation Δz is in (a)–(d) and (l) 3 nm, in (e) and (f) 10 nm and in (g)–(k) 40 nm (insets always with optimized image contrast).

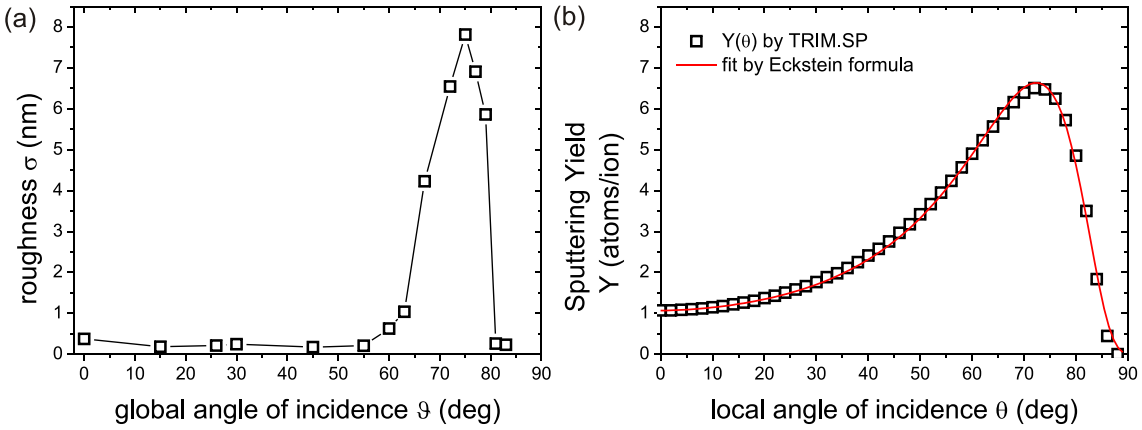

Figure 4.3: (a) Roughness σ as a function of the *global* angle of incidence ϑ for the experiments represented by figure 4.2 (lines to guide the eye). (b) Sputtering yield $Y(\theta)$ as a function of the *local* angle of incidence θ for 2 keV Kr^+ on Si as calculated by TRIM.SP [57]. Red line represents the according data fit [150].

more in detail. For $60° \leq \vartheta \leq 63°$ as shown in figures. 4.2(e)–(f) ripples with a small amplitude and wave vector $\vec{k}$ parallel to the ion beam azimuth developed. For the well-ordered ripples generated at oblique ion beam incidence of $\vartheta = 63°$ we obtain an average wavelength of $\lambda \approx 43\,\text{nm} \pm 9\,\text{nm}$. Still the surface does not destabilize to any significant extent: At $\vartheta = 63°$ the roughness is just $\sigma \approx 1.0\,\text{nm}$ after removal in the order of 1 µm of material. The ripple pattern regularity is apparently improved increasing the angle of incidence from $\vartheta = 60°$ to $\vartheta = 63°$. Pronounced pattern formation takes place in a narrow angular range $67° \leq \vartheta \leq 79°$ represented by figure 4.2(g)–(j), just around the angular range of maximum sputter yield $Y(\vartheta)$. In this angular range we find a pronounced faceted pattern with a sawtooth profile and a maximum roughness of $\sigma = 7.8\,\text{nm}$ at $\vartheta = 75°$. At $\vartheta = 79°$ represented by figure 4.2(k) we find a *tiled roof* pattern [110]. The structures are now elongated along the ion beam and if one would like to assign a $\vec{k}$ to them (which is not justified), it would now be normal rather than parallel to the ion beam azimuth. The roughness is with $\sigma = 5.9\,\text{nm}$ still relatively high. Note also that the

facet structure of the roof tiles in figure 4.2(k) has similarities, but also discrepancies compared to figures 4.2(g)–(j). The roof tiles also display extended facets while the facets normal to the ion beam direction visible in figure 4.2(k) became arrow tips. In figure 4.2(l) for $\vartheta = 81°$ the surface is extremely smooth again with $\sigma = 0.2\,\mathrm{nm}$. A faint ripple pattern with $\vec{k}$ normal to the ion beam azimuth is visible; however, the amplitude of the pattern is marginal. If forced to define a critical angle of ripple rotation, we would set it to $\vartheta_c = 78°$, in reasonable agreement with previous work [110] finding a $\vartheta_c = 80°$ for 5 keV Xe^+ ion erosion of Si.

Figure 4.3(a) summarizes the evolution of the roughness σ already discussed during the presentation of the STM data above. Figure 4.3(b) displays the sputtering yield $Y(\theta)$ as a function of the angle θ of the ion beam with respect to the *local* surface normal calculated by TRIM.SP for 2 keV Kr^+ on Si [57]. The according data fit represented by the red line was done by the use of Eckstein's fit formula [150] and coincides very good with the simulated data.

Figure 4.4 displays the analysis of the facet angles with respect to the incoming ion beam for the angular range $60° \leq \vartheta \leq 79°$ where pattern formation was observed. The points of measurement represent facet segments with linear increase and maximum slope of faceted patterns generated at different *global* ion incident angles ϑ. It is conspicuous that according to the increase of the global angle of incidence the orientation of the facet's local surface normal to the ion beam increases with the same gradient. The local angle of incidence θ_1 of the flat facet is shifted by $\approx 7° \pm 1°$ above the global angle of incidence. The steep facet is shifted for $67° \leq \vartheta \leq 79°$ by $\approx 22° \pm 3°$ below the global angle of incidence. Exceptions are the orientation of the steep facet at $\theta_2 = 60°$ and 63° where the ripple pattern profile is rather symmetric exhibiting a non sawtooth profile and therefore being topographically different.

A constant shift of the facet angles related to the global angle of incidence ϑ stands for a steady facet slope independent of the direction of the incoming ion beam. This relation becomes clear by means of figure 4.5. The border of the

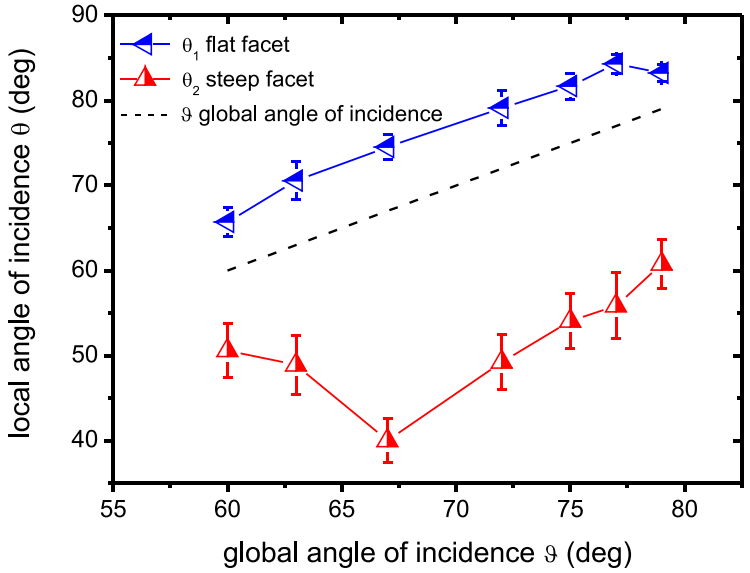

Figure 4.4: Analysis of the pattern facet angles relative to the incoming 2 keV Kr^+ ion beam estimated from STM images presented in figure 4.2. Blue sidewards and red upright oriented triangles show the *local* angle of incidence θ of the flat and steep facet, respectively (lines are to guide the eyes). The dashed line specifies the correlation of the *local* and *global* angle of incidence θ and ϑ.

coloured triangle represents the shape of a possible sawtooth ripple profile restricted to a facet orientation parallel and normal related to the ion beam. The ripple wavelength in each figure is conformed to the lateral position $d = 1.0$. The area within the coloured triangle represents the parameter space of a ripple profile with a defined combination of facet angles. Apparently, both facet angles are defined by setting the position of the apex of the ripple sawtooth profile inside of the coloured triangle. We are exclusively interested in the facets angular alignment so that height and lateral position coordinates are displayed with same scale resulting in an angle-preserving diagram. The colour scale illustrates the *effective sputtering yield* (see below). Hence the according *effective sputtering yield* for a chosen facet angle combination is represented by the colour localized at the specified apex position.

We apply the theory of gradient dependent surface topography development explained in section 2.5 to estimate the erosion rate of a facet combination i.e. a

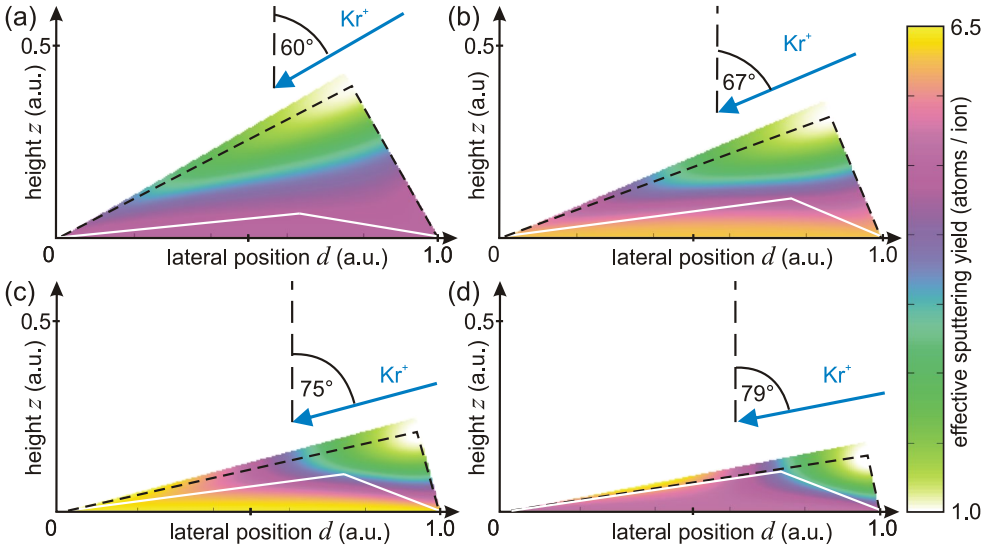

Figure 4.5: Comparison of the calculated sawtooth profile with lowest sputtering yield with the experimentally estimated facet orientation. Choosing a point as position of the apex of the sawtooth profile within the coloured triangle defines the flat and steep facet orientation. The according colour localized at the apex position represents the *effective sputtering yield* (see text) for the defined sawtooth profile with its facet orientations. The dashed black line represents a sawtooth profile of calculated lowest *effective sputtering yield* and the white line represents the experimentally estimated facet orientation. Comparisons are shown for global angles of incidence (a) $\vartheta = 60°$, (b) $\vartheta = 67°$, (c) $\vartheta = 75°$ and (d) $\vartheta = 79°$. Abscissa and ordinate are presented with the same scale so that the illustration is isogonal.

given sawtooth profile. Therefore, we take into account the function of the angle dependent sputtering yield $Y(\theta)$ calculated for 2 keV Kr^+ on Si [fit in figure 4.3(b)] for each facet with its distinct orientation. Furthermore we implement the number of ions impinging on each facet per time unit $\jmath_a$ and $\jmath_b$ resulting in an *effective erosion rate* $\nu_{eff}(\theta_1, \theta_2)$ characteristic for the specific ripple profile:

$$\nu_{eff} = \jmath_a\, Y(\theta_1) + \jmath_b\, Y(\theta_2), \qquad \jmath_a + \jmath_b = const. \tag{4.1}$$

For our calculations we do not use the absolute number of impinging ions per time unit but we exclusively consider the relative fraction of incoming ions per each

facet (see appendix B). Consequently the units are modified to an *effective sputtering yield* Y_{eff} characteristic for a distinct sawtooth ripple profile:

$$Y_{eff} = \frac{\jmath_a}{\jmath_a + \jmath_b} Y(\theta_1) + \frac{\jmath_b}{\jmath_a + \jmath_b} Y(\theta_2) \tag{4.2}$$

The sawtooth profile with a facet combination of minimum *effective sputtering yield* estimated by the calculation above is highlighted within figures 4.5(a)–(d) by a dashed black line. The facet angles evaluated by experiment are demonstrated by the white lines[1].

Discussion

While in figures 4.5(a) and (b) for global incident angles $\vartheta = 60°$ and $\vartheta = 67°$ the flat facets of the calculated profile with lowest *effective sputtering yield* are much steeper than the ones estimated experimentally, merely the flat facets in figures 4.5(c) and (d) for global incident angles $\vartheta = 75°$ and $\vartheta = 79°$ determined by calculation and experiment almost coincide. In fact for global incident angles of $67° \leq \vartheta \leq 79°$ the sawtooth profile always consists of a flat elongated facet with an almost grazing orientation towards the incoming ion beam and a short steep facet facing the incident ion beam. Frequently the facet orientation of a sawtooth profiled pattern was explained with the theory of gradient dependent surface topography development [31; 76; 77; 109; 151; 152] as deduced in section 2.5. The theory predicts that the surface shape is stable with erosion time when flat facets develop and each facet is oriented with respect to the ion beam in the manner that the sputtering yield is minimized ($Y(\theta) = 0° \vee 90°$) or maximized ($Y(\theta) = \theta_p$. However, it is evident by comparing the calculated data with the experimental data that there is a discrepancy: Both facet angles are stable in a quite large angular interval ($67° \leq \vartheta \leq 77°$) and do not change by varying the global angle of incident ions. Therefore, we can rule out the gradient dependent surface topography development as a dominant pat-

[1]Note that the evaluated facet angles represent the steepest slope of each facet. Therefore the real shape of the facets is essentially flatter and partly curved.

terning mechanism to cause the alignment of the facet angles for noble gas ion beam pattern formation on silicon in the low energy range.

Analyzing the facet angle orientations is a valuable examination to prove theoretical treatises. Unfortunately, at that time there is no reasonable theory explicating our findings. Our results show that both the steep and the flat facet seem to have an upper limit. One possible approach may be derived from the observations made on sand dunes where it was found that the height and steepness of the sand dune windward side increases with stronger wind and with increasing fineness of the sediment [153; 154]. In the context of ion beam induced pattern formation the wind strength and fineness of sediment may be representative for the ion energy and the viscosity of the present material, respectively. Therefore, a theoretical study on the facet angle orientation for energy dependent measurements in the high fluence range at oblique ion incidence angles could prove the suggested hypothesis. It should be mentioned that the theoretical work on *solid flow* [41] pursues a similar approach but is restricted to the low fluence regime so that no evidence may be given on the facet angle orientation (see chapter 2.6, p. 23).

Conclusion

Our presented ion incidence angle dependent erosion measurements under highly pure conditions disclose that in a wide angular range even at high fluences the Si surface is stable.

The pattern formation scenario we observe here can hardly be reconciled with models based on the Bradley-Harper theory. A curvature dependent yield as destabilization mechanism neither explains the extended angular range of stability nor the rather abrupt angle-dependent transitions from smooth surfaces to faceted patterns and back to smooth surfaces, i.e. abrupt transitions from surfaces with zero curvature to ones with curvature singularities.

Recently, the smoothing action for near normal incident ions into an amorphous film was reasoned by ion beam induced compressive stress and a resulting mass

redistribution [41; 88].

Patterns with a sawtooth profile generated in the angular range $67° \leq \vartheta \leq 79°$ of incoming ions discover that the facet slope is independent of the incoming direction of ions. So far there is no corresponding theory describing our presented results. Eventually the facet angle orientation is another attribute to prove upcoming theories.

4.3 Ion Beam Induced Smoothing

Introduction

It appears that the absence of roughening for $\vartheta \leq 55°$ is no coincidence, but a result of an inherent smoothing action of the ion beam. To support this idea we bombarded an initially rough surface with normal incident ions.

Results

The initial rough surface was generated by eroding the Si surface with 2 keV Kr^+ incident from $\vartheta = 75°$ [figure 4.6(a)]. After STM imaging of the rough faceted pattern with $\sigma = 9.7\,\text{nm}$, we gradually exposed it to a fluence of $F \approx 2.7 \times 10^{21}\,\text{ions}\,\text{m}^{-2}$ [figure 4.6(b)] and $F \approx 5.4 \times 10^{21}\,\text{ions}\,\text{m}^{-2}$ [Figure 4.6(c)] of 4 keV Kr^+ at normal incidence, thereby halving the roughness to $\sigma \approx 4.8\,\text{nm}$. The fluence dependent sequence discussed above makes evident that first the short wavelengths get smoothed. Figure 4.6(c) discloses that the facet ridges with its high curvature already disappeared while large wavelengths with small curvature still are present. The insets in figures 4.6(b) and (c) demonstrate the small-scale appearance of randomly distributed grains on the smoothed Si surface as usually found on amorphous Si surfaces.

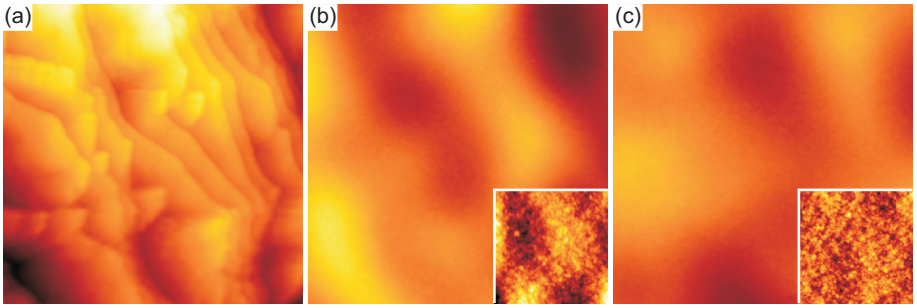

Figure 4.6: STM images of Si(001), image size and image corrugation is always $1\,\mu m \times 1\,\mu m$ and $\Delta z = 50\,nm$, respectively. (a) Rough surface after $2\,keV$ Kr^+ ion bombardment at $\vartheta = 75°$ with a fluence of $1 \times 10^{22}\,ions\,m^{-2}$ (roughness $\sigma \approx 9.7\,nm$). The same Si sample after $4\,keV$ Kr^+ bombardment of (b) $2.7 \times 10^{21}\,ions\,m^{-2}$ ($\sigma \approx 8.2\,nm$) and (c) $5.4 \times 10^{21}\,ions\,m^{-2}$ ($\sigma \approx 4.8\,nm$). The insets show the surface with optimized contrast and a scansize of $200\,nm \times 200\,nm$.

Discussion

Our findings are in agreement with previous work identifying the ion impact induced lateral mass redistribution to lead to short length scale smoothing while nonlinearities are held responsible for a long length scale roughening [29; 116; 127].

4.4 Fluence Dependent Pattern Evolution

Introduction

To investigate the pattern evolution with time we performed fluence dependent erosion experiments. An incident angle of $\vartheta = 75°$ was chosen [see figure 4.7(a)] which is about the maximum in the angle dependent sputtering yield curve for $2\,keV$ Kr^+ [see figure 4.3(b)]. Sputtering at the critical angle θ_p is interesting for the following particular reasons: At this exceptional angle of incidence with the highest erosion rate we expect the fastest pattern development and the highest roughening potency.

Results

The resulting topographies and representative profiles are shown in the STM images of figures 4.7(b)–(f). Figures 4.7(b)—(e) belong to one series of measurement whereupon one and the same sample was exposed to the ion beam and imaged after every particular fluence step. The STM image presented in figure 4.7(f) is measured at a different sample which was eroded without interruption. At this point it should be mentioned that the following results in this section must be considered with caution. With hindsight further experiments disclosed that the fluences given in the experiments (b)–(e) are by a factor of ≈ 6.4 lower than specified. In this series of measurement unfortunately the STM measurements were carried out at the boundary region of the scan area. That means the effective fluence is lower than the below indicated fluence.

However, although we do not know the absolute fluences of the experiments shown in figures 4.7(b)—(e) the trend of the data is unequivocal due to imaging the same sample after every additional fluence step so that we can make proper conclusions nevertheless.

In the initial stadium the smooth surface roughens and a characteristic grain size of $\approx 31\,\mathrm{nm}$ becomes visible [figure 4.7(b)]. No regular pattern is found and the roughness of $\sigma \approx 0.3\,\mathrm{nm}$ is still in the range of the initial wafer roughness. With increasing fluence the roughening proceeds and ripples arise with a characteristic wavelength of $\Lambda \approx 33\,\mathrm{nm}$ oriented with the ripple wave vector $\vec{k}$ parallel towards the ion beam [figure 4.7(c)]. The according profile shows a sinusoidal surface contour with a low amplitude of about 1 nm, the roughness in this stage amounts to $\sigma \approx 0.4\,\mathrm{nm}$. The surface topography of figures 4.7(d)—(f) is composed of facets. The roughness increases with fluence from $\sigma \approx 2.1\,\mathrm{nm}$ in figure 4.7(d) up to $\sigma = 7.8\,\mathrm{nm}$ in figure 4.7(f). Also the wavelength increases with fluence from $\Lambda \approx 61 \pm 17\,\mathrm{nm}$ in figure 4.7(d) to $\Lambda \approx 103 \pm 73\,\mathrm{nm}$ in figure 4.7(f). Obviously, with increasing fluence the pattern coarsens and simultaneously the regularity of the characteristic

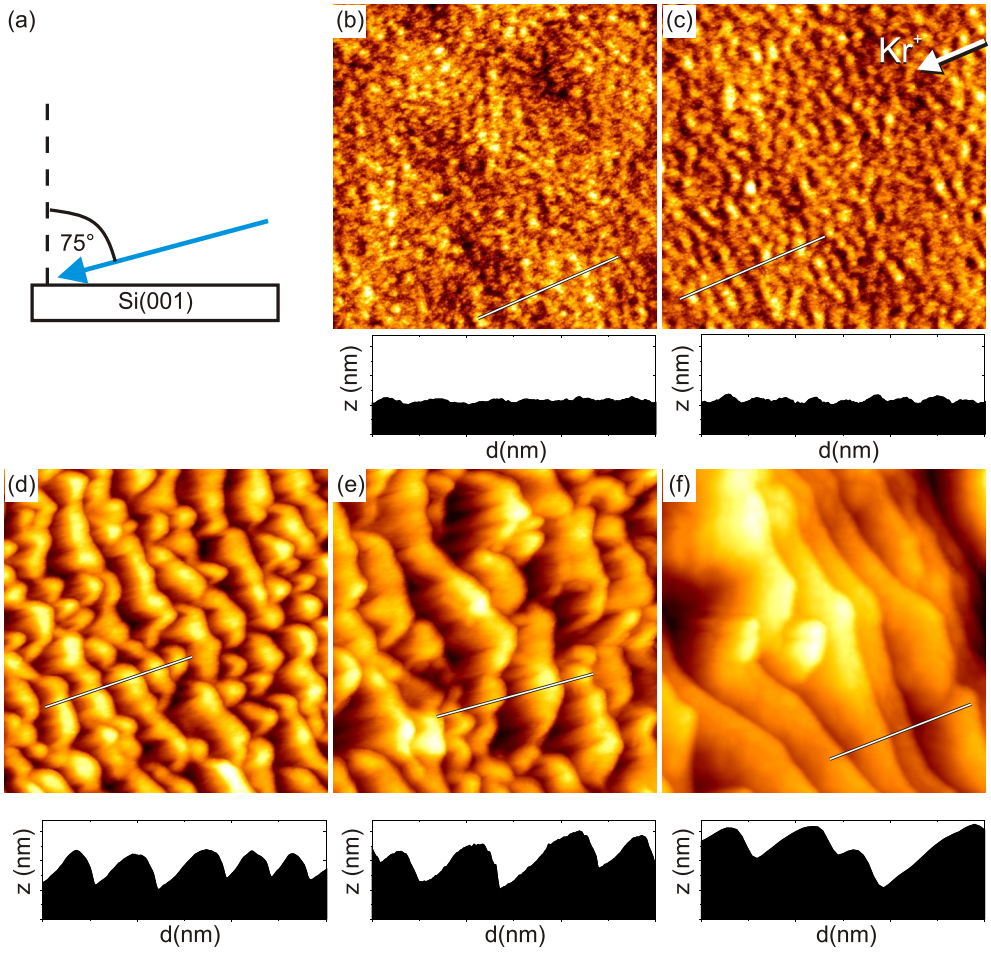

Figure 4.7: (a) Sketch of the sputtering geometry. The angle of incidence ϑ with respect to the surface normal is 75°. (b)–(f) STM topographs of Si(001) after a fluence *at the utmost* of (b) $F < 0.2 \times 10^{21}\,\mathrm{ions\,m^{-2}}$, (c) $F < 0.6 \times 10^{21}\,\mathrm{ions\,m^{-2}}$, (d) $F < 1.7 \times 10^{21}\,\mathrm{ions\,m^{-2}}$, (e) $F < 5.8 \times 10^{21}\,\mathrm{ions\,m^{-2}}$ and (f) $F \approx 10 \times 10^{21}\,\mathrm{ions\,m^{-2}}$ with 2 keV Kr^+ (see text). Each image displayed with optimized contrast. The image size is always 600 nm × 600 nm and the white arrow in (c) indicates the direction of incoming Kr^+ for all images. Below each STM image height profiles along the lines in the according STM images are shown. All profile charts represented with the same scale: height z = 22 nm and width d = 300 nm

pattern wavelength decreases.

Figure 4.8(a) summarizes the evolution of the roughness σ and the characteristic pattern wavelength Λ depending on the fluence already discussed during the

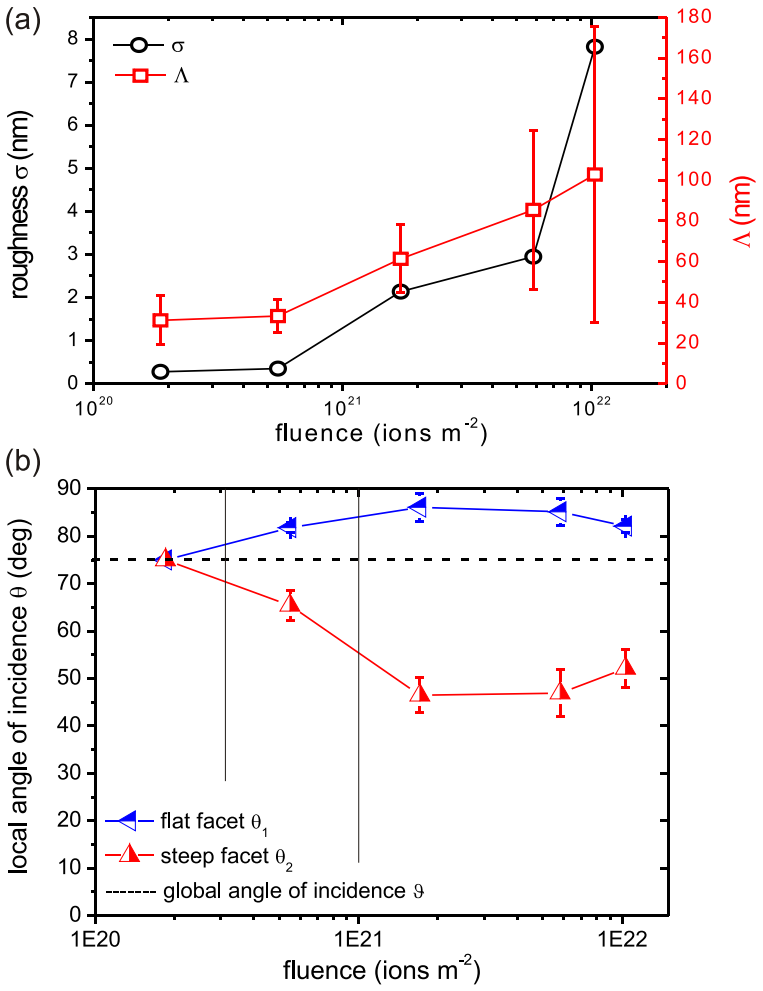

Figure 4.8: Analysis of fluence dependent measurements with 2 keV Kr^+ at $\vartheta = 75°$ on Si(001). (a) Roughness σ (black circles) and facet wavelength Λ (red squares) as a function of the fluence for the experiments represented by figure 4.7. (b) Facet angle analysis of STM images presented in figure 4.7. Blue sidewards and red upside oriented triangles show the local angle of incidence θ of the flat and steep facet, respectively (lines are to guide the eyes). The dashed line crossing $\theta = 75°$ assigns the global angle of incidence of the incoming ion beam.

presentation of the STM data above. Both roughness σ and characteristic pattern wavelength Λ are strictly monotonic increasing with fluence. The experimental data in the investigated fluence range of $F \leq 1 \times 10^{22}$ ions m^{-2} indicates that a saturation in roughness and wavelength is still not reached. The error bars in the determination of the characteristic pattern wavelength show the standard deviation of the

wavelength distribution. Being a measure for pattern regularity the error bars are increasing with fluence.

An analysis of the fluence dependent facet orientation along the projection of the ion beam is displayed in figure 4.8(b). In the initial stage of roughening the located grains are not oriented correlative to the ion beam and we define the facet angles as zero. With increasing fluence ripple ridges arise with a nearly sinusoidal contour defining two facets with $\theta_1 > \vartheta > \theta_2$ [figure 4.7(c)]. The orientation of the opposite ripple facets of this low amplitude pattern related to the incoming ion beam direction with $\vartheta = 75°$ shows a small asymmetry $\theta_1 - \vartheta = 6.8° < \vartheta - \theta_2 = 9.6°$. From this evidence we may deduce already in the initial stage of ripple formation an asymmetric facet orientation. For further ion beam erosion the opposite facets diverge and figure 4.8(b) points out that for a given fluence both the flat and steep facet reach a stable state with $\theta_1 \approx 84° \pm 3°$ and $\theta_2 \approx 49° \pm 4°$, respectively. The last three points of measurement of both facets in figure 4.8(b) belonging to the STM images presented in figure 4.7(d)–(f) show that even though the facet angles reach a stable state the coarsening proceeds as the pattern wavelength grows continuously [see figure 4.8(a)]. Furthermore, the disorder increases simultaneously as characterized by the according error bars of the last three data points of Λ in figure 4.8(a).

Discussion

The fluence dependent pattern evolution may be divided into three stages: In the first stage a roughening takes place. Based on the irregularity of the grain structure the stochastical roughening mechanism comes into consideration (section 2.4).

The second stage represented by figure 4.7(c) is characterized by a ripple pattern with low amplitude where a small angle approximation and a linear approach are still adequate. The angles with steepest slope on both sides of the sinusoidal surface contour are still diverging and the ripple amplitude grows attended by an increasing surface curvature. A determined ripple wavelength $\Lambda = 33\,\mathrm{nm}$ is present

which might be explained by two competing mechanisms. First, a roughening mechanism which predominantly supports the growth of small wavelengths in comparison with large wavelengths and second, a smoothing mechanism which predominantly smooths wavelengths on small scale [155].

The theory of Bradley and Harper with its implemented curvature dependent roughening mechanism is not able to explain the observed results. The continuous function $\Gamma_x(\theta)$ (see [80]) characterizes the curvature dependence of the erosion rate and depends on the energy distribution deposited by the incident ions. Thereby $\tilde{\alpha}$ and $\tilde{\beta}$ represent the widths of the energy distribution parallel and perpendicular to the ion beam direction, respectively [80]. Inserting the average depth of energy deposition $a = 5.4\,\mathrm{nm}$, $\tilde{\alpha} = 17\,\mathrm{nm}$, and $\tilde{\beta} = 14\,\mathrm{nm}$ as calculated by TRIM.SP into $\Gamma_x(\theta)$ together with the global ion beam incident angle $\vartheta = 75°$ leads to a curvature dependent erosion rate of $\Gamma_x > 0$ [155]. From this it follows that the curvature dependent erosion leads to a smoothing instead of a roughening of the surface [80]. Even if the ratios of $\tilde{\alpha}/a$ and $\tilde{\alpha}/\tilde{\beta}$ are changed by 40% still $\Gamma_x > 0$ would apply [155].

We use the *solid flow* model to evaluate our estimated wavelength $\Lambda = 33\,\mathrm{nm}$ within the experiment in the second stage. The surface tension of an amorphous Si layer was estimated by molecular dynamics simulations to $\gamma = 1.36\,\mathrm{J\,m^{-2}}$ [60]. TRIM.SP simulations for 2 keV Kr^+ amount the amorphous layer thickness for normal incident ions to $a = 8\,\mathrm{nm}$ [155]. Substituting the values into equation 2.16 and using a global incident angle of $\vartheta = 75°$ the resulting ripple wavelength of $\Lambda = 33\,\mathrm{nm}$ is found for a hypothesized stress of $\varsigma = 900\,\mathrm{MPa}$. Literature renders values for ion bombardment induced stress with Si as a target material in the range from 200 MPa [30] to 1.62 GPa [156; 157] so that our hypothesized value for the stress ς is reasonable. However, the denoted tolerance of the stress ς allows wavelengths $25\,\mathrm{nm} \leq \Lambda \leq 70\,\mathrm{nm}$ so that the above calculation has only a limited significance.

The third stage presented in figures 4.7(d)–(f) is characterized by stable facet angles and a pattern coarsening with fluence. The pattern is rough and the small

slope approximation is not valid anymore. As evaluated the flat facet of the pronounced ripple pattern is oriented nearly parallel with $\theta_1 \approx 84°$ to the incoming ion beam and the steep facet faces the ion beam with $\theta_2 \approx 46°$. It is evident that such a sawtooth profile considerably reduces the global erosion rate. At the first view these findings could be explained by the theoretical view of gradient dependent surface topography development [76; 77] as discussed in section 2.5. However, the discussion of the facet analysis in section 4.2 revealed that the above mentioned theory is not applicable in a wide range of global incident angles as the facet orientations are independent of the incoming ion beam. Thus the theory of gradient dependent surface topography development may also not be suitable for the present situation.

However, the pattern coarsening with ion fluence may be explained by the coarsening mechanism deduced from Hauffe as explained in section 2.4, p. 17. The mechanism describes how large structures grow at the expense of small structures due to reflected ions which contribute to erosion [75]. In fact TRIM.SP calculations [57] estimate that with a local angle of incidence on the flat facet of up to $\theta_1 \approx 84°$ about 92% of the incoming ions are reflected [155]. Therefore, once the flat facet is developed, the coarsening mechanism becomes strong and even increases with fluence as the flat facets grow.

Complementary to our results Keller et al. have shown that in the investigated fluence range for ripple patterns generated with an ion beam incident angle of $\vartheta = 67°$ the pattern roughness and wavelength increase following a power law until both saturate at high fluences [112; 158].

Conclusions

Analysis of the fluence dependence of pattern formation in the unstable range with $\vartheta = 75°$ discloses that the flat surface develops small amplitude, regular ripple patterns which then evolve to large amplitude, irregular patterns. The well-ordered ripple pattern transforms through a coarsening mechanism to a faceted pattern. The orientation of both ripple facets reaches a stable state at low fluences of $F \approx 1.7 \times 10^{21}\,\mathrm{ions\,m^{-2}}$.

4.5 Fabrication of Crystalline Ripple Patterns

Introduction

From the perspective of application it might be interesting to combine the properties of a patterned surface with the materials electrical and optical properties. The electronic structure of Si has a sensitive dependence on the crystallinity and affects the optical properties [159; 160]. Furthermore, crystalline ripple patterns may be used as templates for epitaxial growth. In both cases a crystalline ripple pattern, rather than an amorphous one, may be of advantage.

Results

A Si(001) wafer was sputtered with 2 keV Kr^+ with a global angle of incidence $\vartheta = 67°$ and a fluence[1] $F < 10^{22}\,\mathrm{ions\,m^{-2}}$; the projected ion beam was oriented along the [110] direction. As a result an amorphous ripple pattern of high regularity oriented with the ripple wave vector $\vec{k}$ parallel to the incoming ion beam developed [figure 4.9(a)]. The ripple wavelength amounts to $\Lambda = 36 \pm 8\,\mathrm{nm}$ with a roughness of $\sigma \approx 1.0\,\mathrm{nm}$.

Subsequently, the ripple pattern was annealed until the LEED screen displayed spots of a crystalline Si(001) surface. Figure 4.9(b) shows the according STM image; still ripples are present even though levelled and with flat terraces on top. The roughness seems not to be affected still we find $\sigma \approx 1.1\,\mathrm{nm}$.

By subsequent high temperature sputtering at $T \approx 910\,\mathrm{K}$ with 2 keV Kr^+ from $\vartheta = 67°$ the previously described ripples vanish while the surface remains crystalline. The roughness slightly decreases to $\sigma \approx 0.9\,\mathrm{nm}$ [figures 4.9(c) and (d)].

Figures 4.9(e)–(g) show the according LEED images to the above discussed STM topographs in figures 4.9(a)–(c), respectively. While the surface is amorphous after

[1] As described already in section 4.4 unfortunately the STM measurement after the present experiment was performed at the edge of the scan area of the ion beam, so that only an upper value for the fluence may be given.

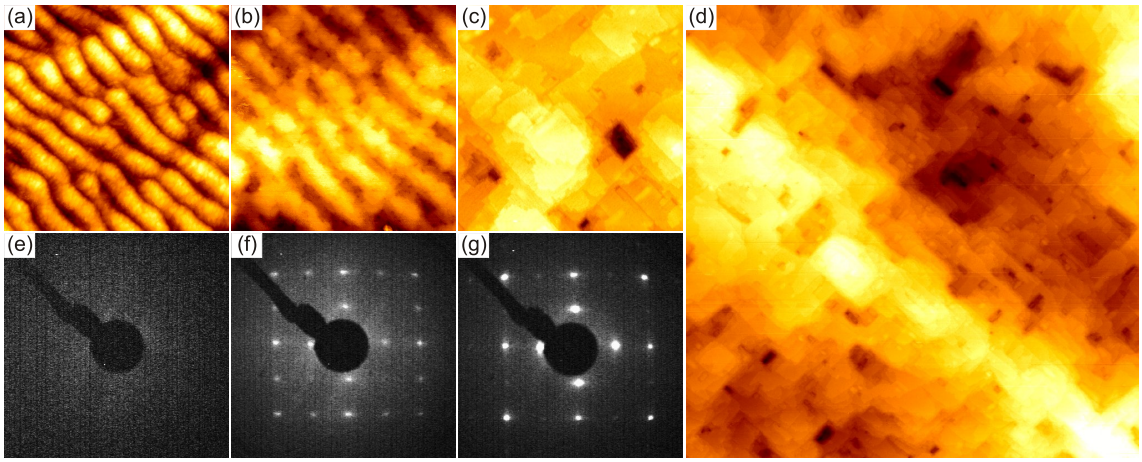

Figure 4.9: (a)–(d) STM images of (a) a ripple pattern generated at room temperature with 2 keV Kr^+ erosion at $\vartheta = 67°$ and a fluence $F < 10^{22}$ ions m^{-2}. (b) Ripple pattern of the same sample after annealing at $T \approx 910$ K without simultaneous erosion, (c) and (d) the same sample after 2 keV Kr^+ erosion at $\vartheta = 67°$ and a fluence of $F < 1 \times 10^{21}$ ions m^{-2} at $T \approx 910$ K. The image size in (a)–(c) is 300 nm × 300 nm and in (d) 1.3 µm × 1.3 µm. The image corrugation Δz is in (a), (b), and (d) 6 nm and in (c) 2 nm. Below each STM image the according LEED image is displayed. While in the LEED image of (e) no spots are found, (f) and (g) show spots of a 2 × 1 reconstruction of a crystalline Si(001) surface.

room temperature sputtering [figure 4.9(e)], after annealing the sample to $T \approx 910$ K a LEED pattern of a 2 × 1 reconstructed crystalline Si surface becomes visible [figure 4.9(f)] and remains crystalline during high temperature sputtering [figure 4.9(g)].

Discussion

Previous results by Erlebacher et al. and Brown et al. on high temperature sputtered silicon carried out in a comparable temperature range of 770 K – 930 K with 500 eV to 1.2 keV Ar^+ at oblique incidence ($\vartheta = 60°$ and 67.5°) but about 30 times higher fluxes and about 60 times higher fluences show as a result a ripple patterned surface with wavelengths between 300 nm and 600 nm [118; 120]. The publications

mentioned above are inconsistent to each other concerning the ripple orientation. While Erlebacher et al. observe for all ion fluxes and fluences ripples oriented with the wave vector $\vec{k}$ parallel to the ion beam only, Brown et al. found both parallel and perpendicular oriented ripples depending on fluence, temperature and ion flux. However, the discussed dimension of wavelengths between 300 nm and 600 nm is in the order of magnitude of the measurable scan width of our STM. Two out of three of our STM topographs on larger scale of the high temperature sputtering experiment [one of them shown in figure 4.9(g)] show a ridge oriented perpendicular to the projected ion beam. These findings arise suspicion that a large scale rippled surface might be existent. If in fact the investigated ridge belongs to a ripple pattern with a wavelength Λ of about 1 µm, due to the very low fluence in our experiment, it would be one in the very early stage of formation.

Conclusion

As a basic result it can be stated that crystalline ripple patterns on silicon can be realized by high temperature oblique incidence sputtering [118; 120] as well as by sputtering and subsequent annealing. Notably, here for the first time crystalline ripples with wavelengths below 100 nm were generated by the latter method.

5 Impurity Assisted Ion Beam Patterning on Si(001)

5.1 Impurity Induced Pattern Morphologies by Co-sputter Deposition

Introduction

To substantiate our claim that impurities resulting from the sputtering process are in fact responsible for the various number of patterns resulting for ion erosion with $\vartheta \leq 55°$ on Si(001) we performed dedicated co-sputter deposition experiments.

Results

As sketched in figure 5.1(a) the ion beam was impinging at $\vartheta = 30°$ onto the sample surface, i. e. at an angle where no pattern formation is expected. Additionally the ion beam hits a piece of stainless steel (Fe 84% and Cr 13%) at an angle $\vartheta_T = 60°$, from which some material is sputter deposited onto the eroding Si surface. This setup is similar to the arrangement used for surfactant sputtering [32].

We took advantage of the fact that in the deposition geometry used, gradients result in the concentration of co-deposited stainless steel species and of primary noble gas ions reflected from the sputter target to the sample surface. These gradients give rise to a pattern manifold as a function of sample location in a single shot experiment.

The STM images were taken along a line normal to the center of the steel plate. As obvious from figures. 5.1(b)–(g) the resulting morphologies strongly depend on

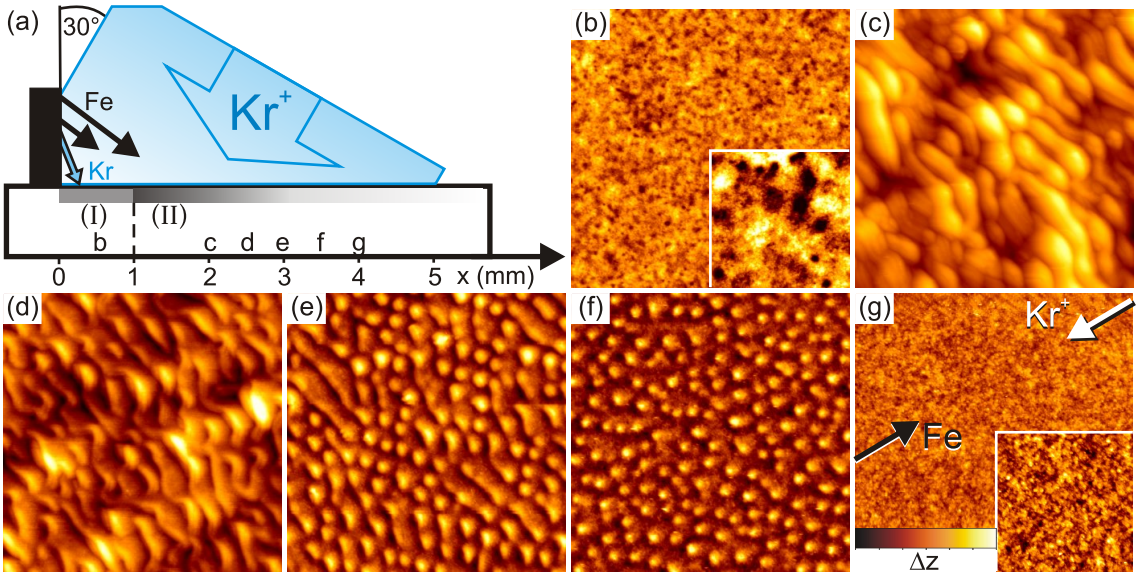

Figure 5.1: (a) Sketch of co-sputter deposition geometry. The gray shading of the upper layer of the substrate schematically visualizes the concentration of co-sputter deposited atoms; dark: high concentration, light: low concentration (see text). The recording positions of the STM topographs shown in (b)–(g) are indicated. (b)–(g) STM topographs of Si(001) after a fluence of $\approx 5 \times 10^{21}$ ions m^{-2} 2 keV Kr^+ at 300 K at $\vartheta = 30°$. The image width is always 625 nm; the inset size in (b) and (g) is 100 nm × 100 nm The ion beam and Fe influx direction is indicated representative for all images by a white and black arrow in (g), respectively. The corrugation Δz is (b) 2 nm, (c) 45 nm, (d) 20 nm, (e) 8 nm, (f) 4 nm and (g) 2 nm.

the normal distance x to the stainless steel plate. Figure 5.1(b) displays a relatively smooth surface with small hole structures as highlighted by the inset (compare also [105]). With increasing x the roughness σ shoots up beyond 10 nm and ripples with the wave vector $\vec{k}$ parallel to the ion beam azimuth form [compare figures 5.1(c) and (d)]. Upon further increase of x the roughness σ decreases again and the ripple pattern transforms [figure 5.1(e)] to a dot pattern [figure 5.1(f)]. Eventually, for the largest distance measured, the roughness σ is comparable to a situation without co-sputter deposition and patterns are absent [compare insets of figures 5.1(b) and (g)].

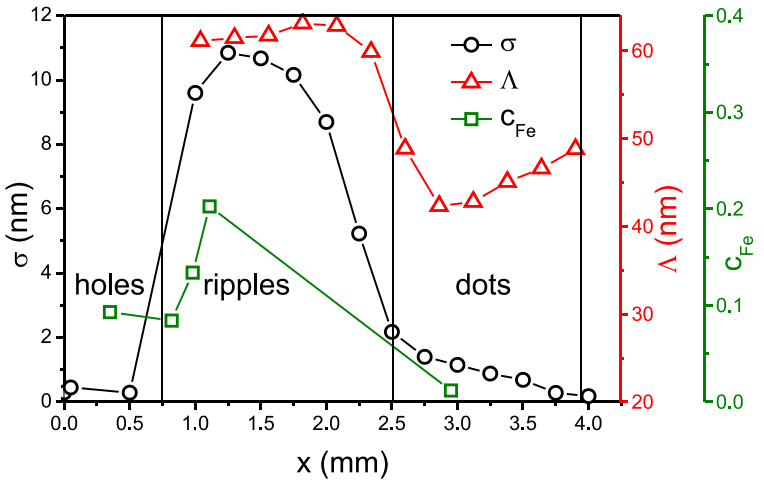

Figure 5.2: Roughness σ (open dots, left y-axis) and feature separation Λ (open triangles, right inner y-axis) of morphologies obtained in the co-sputter deposition visualized in figure 5.1 as a function of the distance x from the stainless steel plate. Maximum iron concentration c_{Fe} normalized to the Si concentration as function of x is shown on the outer right y-axis (open squares). Lines to guide the eye.

Not every co-sputtered material induces patterns. We used the same set-up with a plate of highly oriented pyrolytic graphite instead of stainless steel. The entire Si wafer remained smooth with a roughness $\sigma \approx 0.2\,\mathrm{nm}$ and no patterns formed.

Figure 5.2 displays the roughness σ (open dots, left y-axis), the feature separation Λ (open triangles, right inner y-axis) and the Fe concentration c_{Fe} (open squares, right outer y-axis) for the patterns on the Si wafer as function of x. Schematically in figure 5.2 four pattern ranges are distinguished: nanoholes with $x = 0\,\mathrm{mm} - 1.0\,\mathrm{mm}$, ripples with $x = 1.0\,\mathrm{mm} - 2.5\,\mathrm{mm}$, dots with $x = 2.5\,\mathrm{mm} - 3.8\,\mathrm{mm}$ and a smooth surface for $x > 3.8\,\mathrm{mm}$. The roughness displays a pronounced maximum in the ripple range with $\sigma \approx 10\,\mathrm{nm}$, fades gradually away in the dot range with $\sigma < 2\,\mathrm{nm}$ and is very low in the nanohole and smooth surface range with $\sigma \approx 0.3\,\mathrm{nm}$. The characteristic feature separation varies unspectacularly from a typical ripple wavelength $\Lambda \approx 80\,\mathrm{nm}$ to a typical dot separation with $\Lambda \approx 50\,\mathrm{nm}$. Based on the variety of patterns we expected an inhomogeneous Fe concentration c_{Fe}. For

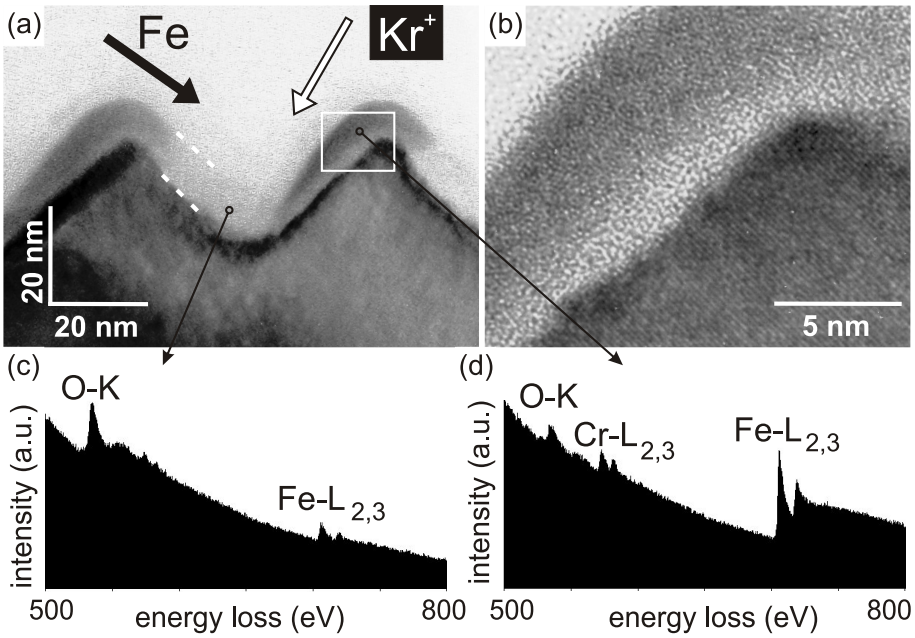

Figure 5.3: (a) Cross-sectional bright-field TEM image of ripples generated by sputter co-deposition at 300 K [according to figure 5.1(c)]. The dashed white lines highlight the ion beam amorphized Si layer. The area enclosed by the white box is shown as high resolution TEM image in (b). The circle in the valley at the origin of the left arrow and the circle close to the ripple ridge at the origin of the right arrow indicate the selected areas, where EELS spectra were taken, which are displayed in (c) and (d), respectively. The arrows labelled Kr^+ and Fe give the directions of the primary ion beam and the sputter co-deposited material flux, respectively.

chemical analysis we performed secondary ion mass spectrometry. Quantification of our data is based on the tables of SIMS impurity signals in Si obtained for 8 keV O_2^+ sputtering [161; 162]. Here we used 250 eV O_2^+ to minimize implantation and mixing and achieve a high depth resolution. The surface roughness and the potentially inhomogeneous Fe distribution makes our quantification problematic, which therefore should be considered with caution. We measure a maximum of the relative iron concentration $c_{\mathrm{Fe}} \approx 0.20$ in the ripple range. Still $c_{\mathrm{Fe}} \approx 0.02$ is sufficient to induce the dot range.

Figure 5.3(a) is a cross-sectional bright-field TEM image of a ripple pattern at

$x \approx 2.5\,\mathrm{mm}$ created at 300 K. Figure 5.3(b) is a high resolution micrograph of the area indicated by the white box in figure 5.3(a). The brightness of the amorphous layer varies due to the concentration variation of co-sputter deposited material. The darker patches result from the stronger electron scattering of the elements Fe and Cr with higher atomic number. It is apparent that the sputter co-deposited material has its highest concentration on the facet facing the incoming particle flux as indicated by the black arrow in figure 5.3. This interpretation is confirmed by EELS spot analysis (beam diameter: 1 nm) of a bright location in the amorphous surface layer [circle at origin of left arrow in figure 5.3(a)] and a dark location [circle at origin of right arrow in figure 5.3(a)], which are represented in figures 5.3(c) and (d), respectively. The EELS spectrum in figure 5.3(c) displays a strong oxygen O-K core loss peak and an Fe-$L_{2,3}$ ionization edge of considerably lower height. In contrast, the EELS spectrum of figure 5.3(d) is dominated by the peak of the Fe-$L_{2,3}$ shell ionization, an additional Cr-$L_{2,3}$ loss peak is visible and the loss peak of the O-K shell ionization is diminished. Apparently, the enhanced concentration of the sputter co-deposited material on the facet facing the stainless steel plate in turn reduces also post-oxidation.

In the high resolution TEM image of figure 5.3(b) the crystalline structure of the substrate is visible. In addition, within the Fe-rich parts of the amorphous layer small crystalline patches are visible. It appears plausible that due to ion beam induced mixing the co-sputtered Fe forms a silicide in the surface near layers as it has been found for normal incidence ion bombardment through an alternating cold cathode ion source [105]. However, referring to grazing incidence X-ray diffraction measurements examined in section 5.2 and 5.4, no crystalline iron silicide forms at the room temperature co-sputter deposition experiment at hand. Therefore, we interpret the small crystalline patches visible in figure 5.3(b) as indications for nano-crystalline iron-silicide.

The next relevant observation based on the EELS analysis shown in figure 5.3 is that the sputter co-deposited material is non-uniformly distributed over the pat-

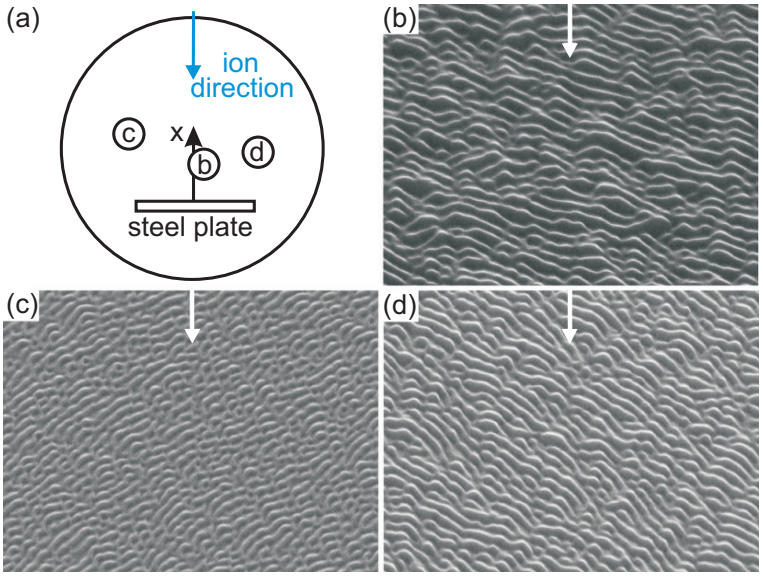

Figure 5.4: (a) Top view sketch of the Si sample indicating the positions, where images (b)–(d) were taken by scanning electron microscopy (SEM) after the erosion experiment visualized by figure 5.1 had been conducted. x-axis indicates the normal to the center of the steel plate. The direction of e-beam illumination is at 45° with respect to the surface normal and the e-beam energy 15 keV. The image width in (b)–(d) is 2 µm.

terned surface. In fact, the material forms a chemical pattern in phase with the topographic pattern. The same conclusion was already obtained several times [35; 141] and was obvious also much earlier from bright-field TEM images that displayed dark shadows on the ripple ridges in registry with the pattern (compare [131; 139]). These dark shadows are due to an enhanced electron scattering at the high atomic number impurities.

We further explored the pattern at locations displaced from the normal to the center of the stainless steel plate (i.e. left and right of the x-axis) by scanning electron microscopy. Figure 5.4(a) sketches the locations of the SEM micrographs displayed in figures 5.4(b)–(d). It is obvious that the ripple wave vector $\vec{k}$ depends on the position with respect to the stainless steel plate. Apparently $\vec{k}$ is parallel to the average azimuthal direction of the atoms sputter deposited from the stainless steel plate onto the Si wafer.

Discussion

The co-sputter situation is complex and in order to prepare an understanding of pattern formation in this situation it is mandatory to consider energy, direction and species of the particles impinging onto the Si wafer. The region adjacent to the stainless steel plate with $0 \leq x \leq 1\,\mathrm{mm}$ and indicated as (I) in figure 5.1(a) receives $2\,\mathrm{keV}$ Kr^+ ions, sputtered Fe atoms (we neglect Cr atoms in the following discussion for simplicity) and Kr particles reflected from the stainless plate. Therefore, we performed TRIM.SP simulations to get more insight even though the simulated results in the first place describe the situation qualitatively rather than absolute. Figure 5.5(a) displays the differential Fe sputter yield $\frac{dY_{\mathrm{Fe}}}{d\Omega}(\vartheta)$ averaged over the azimuthal angular range $\varphi \in [-30°, 30°]$ as calculated by TRIM.SP [42]. The distribution of the Fe atoms is anisotropic with a broad peak of emission centered at about $\vartheta \approx 37°$. As the Si wafer can be imagined horizontally under the polar diagram, the main flux of sputtered Fe atoms is directed towards the Si wafer. The total yield Y_{Fe} per $2\,\mathrm{keV}$ Kr^+ is substantial and amounts to $Y_{\mathrm{Fe}} = 6.4$.

Figure 5.5(b) shows the differential backscattering coefficient $\frac{dR_{\mathrm{Kr}}}{d\Omega}(\vartheta)$ of the Kr^+ particles backscattered from the stainless steel plate and averaged over the azimuthal angular range $\varphi \in [-30°, 30°]$. The distribution of the backscattered particles is peaked at an exit angle of $\vartheta \approx 68°$. In average the backscattered Kr particles will hit the Si wafer closer to the stainless steel plate than the sputtered Fe atoms, i.e. at a smaller distance x. The total backscattering coefficient amounts to $R_{\mathrm{Kr}} = 0.24$.

Figure 5.5(c) displays the energies E of the sputtered Fe atoms and of the backscattered Kr particles as a function of the polar emission angle ϑ. The data plotted is averaged over the azimuthal angular range $\varphi \in [-30°, 30°]$. The energy of the sputtered Fe atoms is moderate with a maximum of $\approx 210\,\mathrm{eV}$ for $\vartheta \approx 74°$. Note that at the most probable angle of emission of sputtered Fe atoms $\vartheta \approx 37°$ the energy of the sputtered Fe atoms is only about $65\,\mathrm{eV}$ in the presented azimuthal angular range. The average energy of the Fe atoms sputtered in the azimuthal an-

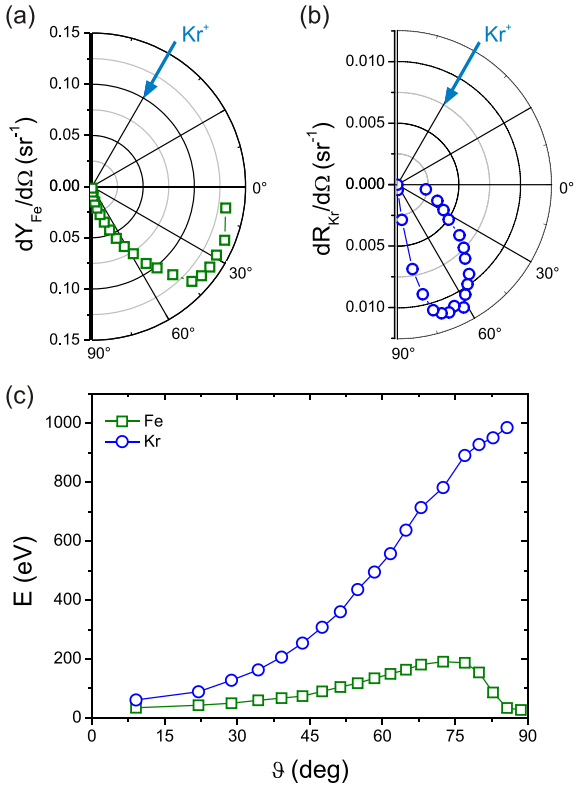

Figure 5.5: (a) Differential sputtering yield $\frac{dY_{\mathrm{Fe}}}{d\Omega}$ and (b) differential backscattering coefficient $\frac{dR_{\mathrm{Kr}}}{d\Omega}$ of 2 keV Kr^+ impinging on the steel plate plotted as a function of the polar emission angle ϑ. The data shown is averaged over the azimuthal angular range $\varphi \in [-30°, 30°]$. The arrows indicate the direction of the impinging Kr^+. (c) Average energy of the sputtered Fe atoms or backscattered Kr particles as a function of their polar emission angle ϑ. The data shown is averaged over the azimuthal angular range $\varphi \in [-30°, 30°]$. All data calculated by TRIM.SP [57].

gular range $\varphi \in [-30°, 30°]$ is 112 eV, the average energy of all atoms sputtered in forward direction with $\varphi \in [-90°, 90°]$ is 72 eV. Though substantial, the energy of the Fe particles is insufficient to cause significant sputtering of the Si wafer. The energy of the backscattered Kr particles increases monotonically with their emission angle ϑ and reaches ≈ 1200 eV for $\vartheta \approx 90°$. Note that at the most probable emission angle of $\vartheta \approx 68°$ the energy of the emitted particles is about 755 eV. Due to a rather narrow angular distribution the backscattered particles will therefore cause strong

erosion of the Si wafer near the steel plate. The average energy of the backscattered Kr particles in the presented azimuthal angular range $\varphi \in [-30°, 30°]$ is 583 eV, the average energy of all particles backscattered towards the Si plate in the angular range $\varphi \in [-90°, 90°]$ is 470 eV. These findings ascertain that in the region indicated as (II) in figure 5.1(a) with $x > 1$ mm the flux of Kr^+ scattered from the target is absent.

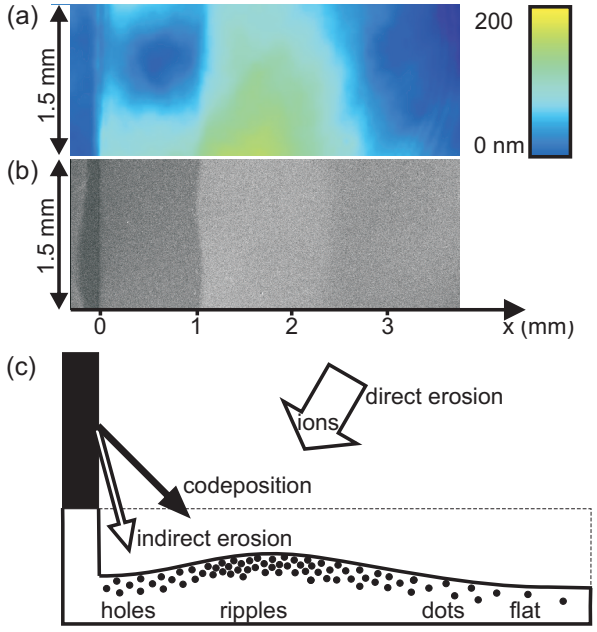

Figure 5.6: (a) Detail of the topography of the Si wafer measured by phase-shifting interferometry. Center of the long image axis identical with coordinate x. Dark blue contrast for the area with $x < 0$ indicates the position of the steel plate and not height. (b) Large scale SEM image of the Si wafer. The position of the stainless steel plate during the erosion experiment is indicated. (c) Schematic sketch of the erosion situation with co-sputter deposition (see text).

Figure 5.6(a) displays a section of a height topograph of the Si-wafer after co-sputter deposition measured by phase-shifting interferometry. We attribute the hill in the height profile in the range 1 mm $\leq$ x $\leq$ 2.5 mm with a height of $\approx$ 75 nm to the significant amount of co-sputtered Fe in this range. Note that the hill does not consist entirely of Fe – actually most of the co-sputter deposited Fe has been resput-

tered by the Kr^+ ion beam. However, the co-sputter deposited Fe partly shielded the Si from being removed by the direct Kr^+ ion beam resulting in a significantly reduced erosion depth. The trough next to the stainless steel plate for $0 \leq x \leq 1\,\mathrm{mm}$ results from the additional sputtering caused by the energetic component of the Kr particles reflected from the stainless steel plate. According to micro phase interference patterns at the edge of the scanning area of the ion beam the average erosion depth is $\approx 300\,\mathrm{nm}$. The SEM topograph in figure 5.6(b) shows a contrast change at the onset of the co-sputter hill caused by the transition from the smooth nanohole to the rippled surface. This is also consistent with the pattern sequence as observed by STM in figure 5.1. In view of the significant flux and energy of the reflected Kr particles arriving in the trough area, there the lower c_{Fe} is a consequence of the enhanced resputtering. Dot patterns form beyond the co-sputter deposition hill, where the arriving flux of Fe atoms is lower resulting in a lower c_{Fe}. Figure 5.6(c) summarizes the discussion schematically and displays the link between the arriving particles, the erosion depth and the patterns formed.

We mentioned that by using graphite as a sputter target instead of stainless steel the surface remained smooth and no patterns formed. It should be noted that due to the low mass of C the energy transfer by the Kr^+ ions is less efficient compared to Fe so that the sputtering yield of C is lower by approximately 50%. From this it follows that the impurity flux is halved and the comparability of the experiments is questionable. In this context, other interesting materials for a sputter target would be especially Pd and Ag having comparable masses, a comparable sputtering yield[1], but in combination with Si a quite different phase diagram. While Pd builds silicides [163], Ag has a negligible solubility in silicon and builds no compounds [164]. By comparison of Pd and Ag co-sputter deposition experiments one could learn if either collision details as preferential sputtering or chemical reaction of the deposited species with the target are decisive for the pattern formation process.

[1] $Y_{Pd}(60°) = 6.4$ atoms/ion, $Y_{Ag}(60°) = 7.8$ atoms/ion, calculated by TRIM.SP.

Conclusions

Intentional co-sputter deposition of stainless steel from a plate hit together with the Si sample by the ion beam leads to a complex sequence of patterns in dependence of the distance from the steel plate. These patterns form at angles ϑ, where no patterns result for clean ion erosion.

Based on the data the three following conclusions are obtained: (i) Dot patterns form during 2 keV Kr^+ ion beam erosion with $\vartheta = 30°$ for moderate co-sputtered Fe concentrations c_{Fe} and in the absence of reflected Kr particles, i.e. in the absence of a second component of energetic particles impinging from a different direction onto the substrate. (ii) Ripple patterns form on the Si substrate for high co-sputtered Fe concentrations: As the flux and the energy of the reflected Kr particles arriving in the ripple pattern area $1\,\text{mm} \leq x \leq 2.5\,\text{mm}$ are small, their presence appears not to be necessary for ripple pattern formation. (iii) Erosion by the direct beam together with strong sputtering by particles from a different direction (here through the reflected energetic Kr particles) prevents formation of a pronounced and rough pattern. Although we detect a significant amount of Fe for $x \leq 1\,\text{mm}$ in region (I), the area remains rather smooth and the nanohole pattern is neither pronounced nor well ordered.

However, our investigations reveal the chemical modulation of the pattern to be in phase with the height modulation. Furthermore, the direction of impingement of the co-sputtered Fe atoms determines the orientation of the ripple wave vector $\vec{k}$. Whether ripple orientation towards the stainless steel plate is due to the additional directed energy of the arriving Fe particles or due to the directed attachment of the Fe particles to elevations (ripple slopes) in their line of sight can not be resolved by the present experiment and will be ascertained in section 5.5.

Our observations are consistent with the observation of Mo-seeding at $\vartheta = 0°$ [29; 127; 128] and the absence of patterns without Mo-seeding [29; 127].

As a global key result of our experiments we consider the fact that supply of a sec-

ond chemical species is mandatory for pattern formation on Si in a large parameter range, specifically for $\vartheta \leq 55°$. Whether co-sputter deposition must be considered also for pattern formation of other materials or other energy ranges outside the 1 keV region as a hidden parameter, remains to be investigated.

5.2 Temperature Dependence

Introduction

In the previous chapter the co-deposition of a second chemical species during ion beam erosion of Si was identified to destabilize the surface. As pattern formation is always the result of the interplay of a destabilizing mechanism and a stabilizing or smoothing one, the nature of the latter needs to be explored as well. Temperature as a fundamental parameter attached importance in theoretical [80] and numerous experimental publications [117; 118; 120; 129; 132; 165].

The section at hand specifies the influence of temperature on ion beam pattern formation with co-sputter deposition. The following measurements are limited to a temperature range in which the surface remains amorphous or in other words does not recrystallize during ion bombardment. We perform co-sputter deposition experiments at very low and elevated temperatures to test the relevance of thermal diffusion.

Measurements on metal assisted ion beam erosion in the crystalline temperature range will be obtained afterwards in section 5.4.

Results

Figure 5.7 gives an overview on the temperature dependent morphologies as a function of the distance x to the steel plate. The three rows correspond to the erosion temperatures of 140 K, 300 K, and 440 K (from bottom to top), the four columns correspond to distances $x \approx 0.5$ mm, $x \approx 2.5$ mm, $x \approx 3$ mm and $x \approx 4.5$ mm (from left to right).

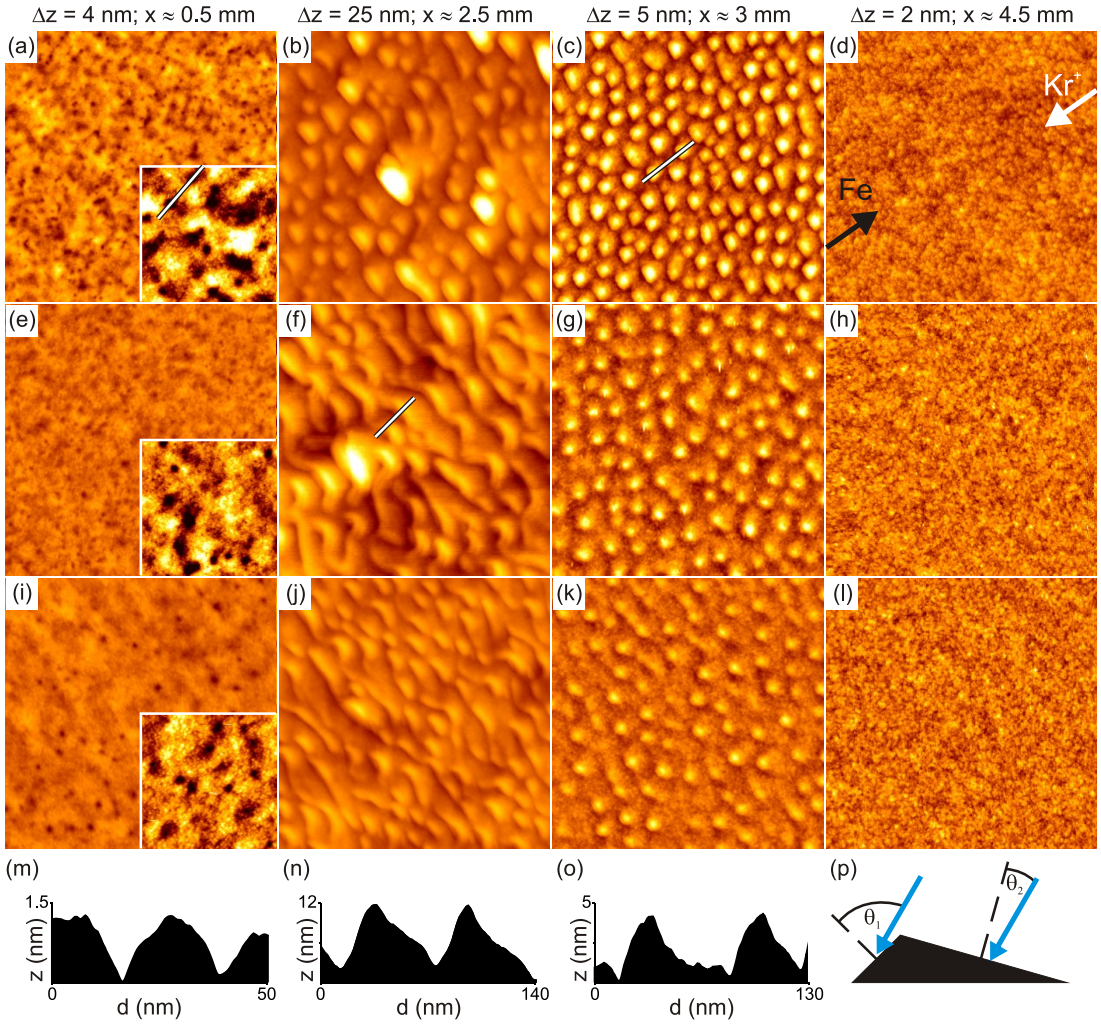

Figure 5.7: STM images of Si(001) taken after a fluence of $F \approx 5 \times 10^{21}$ ions m^{-2} 2 keV Kr^+ in the sputter co-deposition geometry. The temperature of ion exposure is fixed for each row: (a)–(d) 440 K, (e)–(h) 300 K, and (i)–(l) 140 K. The distance x normal to the stainless steel plate and the height difference Δz spanned by the image contrast between white and black are indicated above the columns. Note the large differences in Δz for the four columns. The black and white arrows in (d) visualize the projected directions of incoming sputtered Fe atoms and of the primary Kr^+, respectively. Image size is always 500 nm × 500 nm, the size of the insets in (a), (e) and (i) is 100 nm × 100 nm. Height profiles along the lines in the inset of (a), in (f) and (c) are shown in (m), (n) and (o), respectively. (p) Sketch defining the local angles of incidence θ of the facets.

It is obvious from figure 5.7 that the patterns in each column are similar, irrespective of the temperature during ion exposure: The first column with $x \approx 0.5\,\mathrm{mm}$ [figures 5.7(a), (e), and (i)] represents a flat surface with randomly distributed holes. The roughness of this hole pattern is low with $\sigma \approx 0.25\,\mathrm{nm}$. At 440 K, the hole pattern is somewhat more pronounced and has a slightly higher roughness of $\sigma \approx 0.35\,\mathrm{nm}$. The depth of a hole is 1nm–1.5 nm as visible in figure 5.7(m), which displays the height profile along the line in the inset of figure 5.7(a). The second column with $x \approx 2.5\,\mathrm{mm}$ [figures 5.7(b), (f), and (j)] represents a pattern of short ripple segments with the wave vector $\vec{k}$ parallel to the projection of the ion beam on the sample surface. The roughness of the presented ripple patterns is $\sigma \approx 3\,\mathrm{nm}$, with a typical corrugation between valleys and ridges of about 10 nm. The ripple wavelength is $\Lambda \approx 50\,\mathrm{nm}$ and varies only insignificantly with temperature. As apparent from the height profile along the line in figure 5.7(f) shown in figure 5.7(n), the ripples are asymmetric with a steep flank facing the incoming co-sputter deposition flux. Typical angles between the local surface normals of the facet and the primary ion beam are $\theta_1 \approx 15°$ [facet facing the primary ion beam, according to figure 5.7(p)] and $\theta_2 \approx 65°$ [facet facing the sputter co-deposition flux, see figure 5.7(p)]. The third column with $x \approx 3\,\mathrm{mm}$ [figures 5.7(c), (g), and (k)] represents dot patterns. The roughness of the dot patterns is much lower than for the ripple patterns and is around $\sigma \approx 1\,\mathrm{nm}$. The dot density increases slightly with temperature corresponding to a decrease of the typical dot-dot spacing from 45 nm at 140 K to 40 nm at 440 K. Also the dots are asymmetric with a steep flank facing the incoming sputter co-deposition flux. The height profile along the line in figure 5.7(c) is shown in figure 5.7(o). Typical angles between the local surface normals of the dot facets and the primary ion beam are $\theta_1 \approx 50°$ (facet facing the sputter co-deposition flux) and $\theta_2 \approx 20°$ (facet facing the primary ion beam). Based on our SIMS measurements for the 300 K sample, the Fe concentration of the sputter co-deposited material in the surface layer has reduced from its peak value at the onset of the ripple pattern range of $c_{\mathrm{Fe}} \approx 0.20$ to $c_{\mathrm{Fe}} = 0.01 - 0.02$ [compare figure 5.2]. The fourth column with

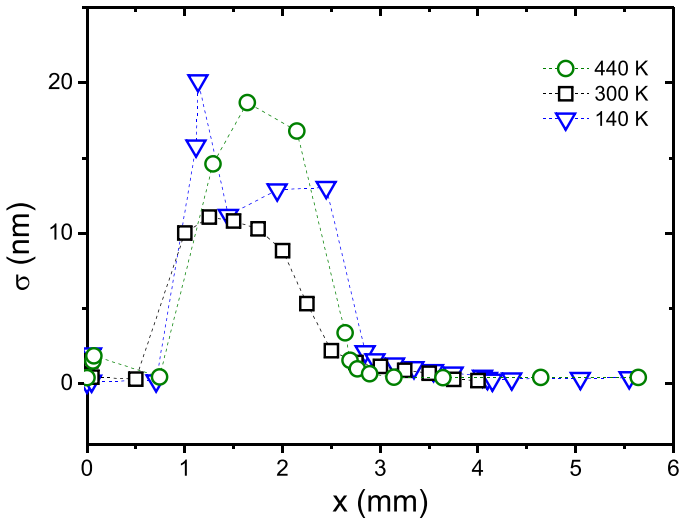

Figure 5.8: Roughness σ as a function of normal distance x to the stainless plate for the erosion temperatures indicated (see text). Lines to guide the eye.

$x \approx 4\,\mathrm{mm}$ [figures 5.7(d), (h), and (l)] represents a flat surface without a pattern. The roughness is $\sigma \approx 0.2\,\mathrm{nm}$ and has a comparable value as would be obtained for ion erosion without co-sputter deposition.

Figure 5.8 represents the result of a systematic roughness analysis based on AFM topographs measured ex situ. Within the AFM it was possible to vary the x-coordinate systematically with high precision at the disadvantage of lower resolution and postoxidation of the wafer. It is apparent that the roughness has for all three temperatures a pronounced and broad maximum reaching $\sigma \approx 10\,\mathrm{nm} - 20\,\mathrm{nm}$ in the x-range between 1 mm and 2.5 mm, i.e. in the x-range where the ripple patterns form. Some scatter in the roughness data is visible around $x \approx 1\,\mathrm{mm}$, caused by the abruptness and inhomogeneity of the pattern changes in this range (see section 5.3).

We conducted additional GI-XRD investigations of the 440 K sample and found no trace of a signal for any of the crystalline iron silicide phases.

Figure 5.9 summarizes the discussion of the phenomenology of patterns in a morphological phase diagram. We distinguish four fundamental types of surface areas as a function of the x-coordinate: the flat hole regime with negligible roughness

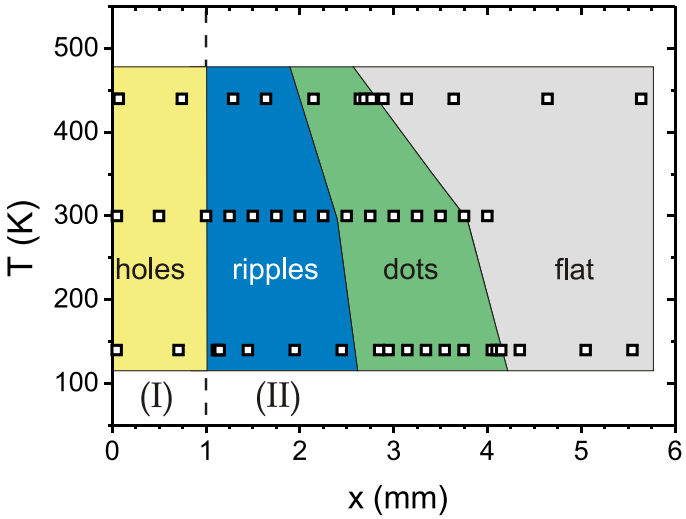

Figure 5.9: Phase diagram of patterns observed as a function of distance x and temperature T (see text).

within region (I) exposed simultaneously to scattered Kr^+. Within region (II) three regimes are found: the rough ripple regime, the dot regime, as well as the flat surface. The transition between the latter three morphological phases is continuous: With increasing x-coordinate, the ripple pattern gradually transforms to a dot pattern which eventually vanishes as the roughness approaches the limiting value of $\sigma \approx 0.2\,\mathrm{nm}$. Therefore, these pattern transitions are not quantitatively defined, but depend slightly on the visual judgment. To the contrary, the transition between holes and ripples is not gradual but locally abrupt with a narrow zone of increasing ripple area fraction. The location of this phase transition is strictly temperature independent, while for the other transitions a tendency for a shift towards lower x-coordinate with increasing temperature is visible.

Discussion

Pattern type and sequence of patterns observed with increasing x-coordinate are temperature independent in a wide temperature range (140 K – 440 K). The pattern transition positions depend only weakly on temperature. Roughness differences for

the same x-position are lower than a factor of two. Wavelength or dot spacings agree to within 20%. Based on these facts we conclude that thermally activated processes are largely irrelevant for pattern formation under sputter co-deposition conditions. Any thermally activated process relevant for pattern formation at room temperature would either decrease or increase its frequency by orders of magnitude through either lowering or increasing the temperature by about 150 K as pursued here. The frequency of a thermally activated elementary process may be expressed by an Arrhenius law $f = f_0\, e^{E_a/k_B T}$ with f_0 being the attempt frequency in the order of a phonon frequency and k_B the Boltzmann constant. If we consider a process as relevant if it proceeds with a frequency $f = 1\,\mathrm{Hz}$ and if we assume a standard attempt frequency of $5 \times 10^{12}\,\mathrm{Hz}$, a process relevant at 300 K has an activation energy of about 0.75 eV. Its frequency at 140 K would be $5 \times 10^{-15}\,\mathrm{Hz}$ and at 440 K $1.3 \times 10^{4}\,\mathrm{Hz}$. As thermally activated processes of diffusion or reaction are irrelevant for the pattern formation with co-sputter deposition, it is probable that the same holds for ion induced pattern formation on Si(001) in the absence of co-deposition. Slight temperature dependencies just outside the experimental scatter are present in our data. The pattern transition lines within region (II) shift towards smaller x with increasing temperature. Both effects may be due to thermally activated processes just becoming visible at 440 K (though not yet relevant) or due to a physical effect with a weaker dependence on temperature than an activated process. One plausible speculation is to assume that the slight changes observed are due to a decrease of viscosity of the amorphous layer with temperature.

The largely temperature independent pattern formation agrees with the findings of Gago et al. [132]. Based on their temperature dependent dot pattern investigations in the range of 300 K to 525 K after normal incidence sputtering with unintentional impurity sputter co-deposition, they state: "In the low-T range $\leq 400\,\mathrm{K}$, the pattern is not significantly affected by T [...]". Also Ozaydin-Ince and Ludwig find in their normal incidence Mo seeding studies in the entire temperature range from $T \approx 300\,\mathrm{K}$ to $T \approx 570\,\mathrm{K}$ only very moderate changes of roughness and wave-

length by less than a factor of two [127]. These statements do not fully coincide with a subsequent normal incidence study by Sánchez-García et al. [129], who find a significant change in their hole pattern roughness by a factor of three already between 300 K and 400 K. It may well be that these differences are linked to the exact nature of the sputter co-deposited material. But all three studies agree on the absence of pronounced or even qualitative changes of patterns with temperature in the temperature range around room temperature.

Conclusions

We find thermally activated processes to be irrelevant for room temperature ion beam pattern formation on Si(001). However, slight changes in the pattern shape for different temperatures were observed. The best pattern homogeneity was realized at low temperatures.

5.3 Morphological Phase Transition: From a Smooth to a Rippled Surface

Introduction

From figure 5.8 in section 5.2 it is apparent that up to now we did not yet present any topographic data from the rough region with 1 mm $\leq$ x $\leq$ 2.5 mm. The reason is simply that – due to the roughness in this range – STM topographs free of tip artefacts are almost impossible to record. In order to discuss this x-range we therefore refer to AFM and SEM data.

Results

Figure 5.10 displays a sequence of AFM images with increasing x-coordinate after ion exposure at 140 K and measurement at 300 K. By comparison of images taken *in situ* at 140 K by STM and taken *ex situ* at 300 K by AFM in the smoother

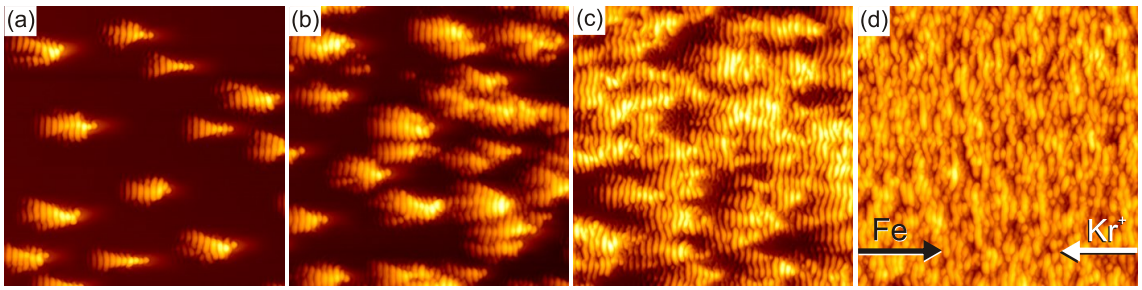

Figure 5.10: AFM images after co-sputter deposition at 140 K taken *ex situ* at 300 K at positions (a) $x = 1.12$ mm, (b) $x = 1.14$ mm, (c) $x = 1.15$ mm, and (d) $x = 1.45$ mm. The directions of the incoming co-deposited Fe and Kr^+ projected onto the surface are indicated in (d). The height difference Δz spanned by the image contrast between white and black is 100 nm for all images. Image size is always 3 µm × 3 µm.

regions with $x \leq 2.5$ mm we find no differences of significance due to the annealing to room temperature and the exposure to ambient conditions. The sequence of AFM images shows that the transition from the hole pattern to the ripple pattern is not gradual and smooth, but abrupt and inhomogeneous. It has not a single sharp boundary, but rough and flat patches coexist for a narrow range of x-coordinate values. Figure 5.10(a) with $x = 1.12$ mm displays on a flat hole pattern background with a very low roughness of $\sigma \approx 0.2$ nm [similar as seen in figure 5.7(i)] the rise of characteristic rippled objects. The rippled structure of such an object mimics the segmented exoskeleton of a pill bug, a brief term for this feature used below. Moving towards larger values of the x-coordinate, the concentration of the pill bugs increases [figure 5.10(b) with $x = 1.14$ mm] until they percolate in figure 5.10(c) at $x = 1.15$ mm. Only small patches of the flat hole pattern are left. Figure 5.10(d) displays an AFM image of the fully developed ripple pattern taken at $x = 1.45$ mm.

The morphological phase transition from the flat area with shallow depressions to the rough ripple pattern is temperature independent. The sequence of SEM images of a sample after sputter co-deposition at 440 K shown in figure 5.11 displays precisely the same pattern transition as the sequence of AFM topographs of fig-

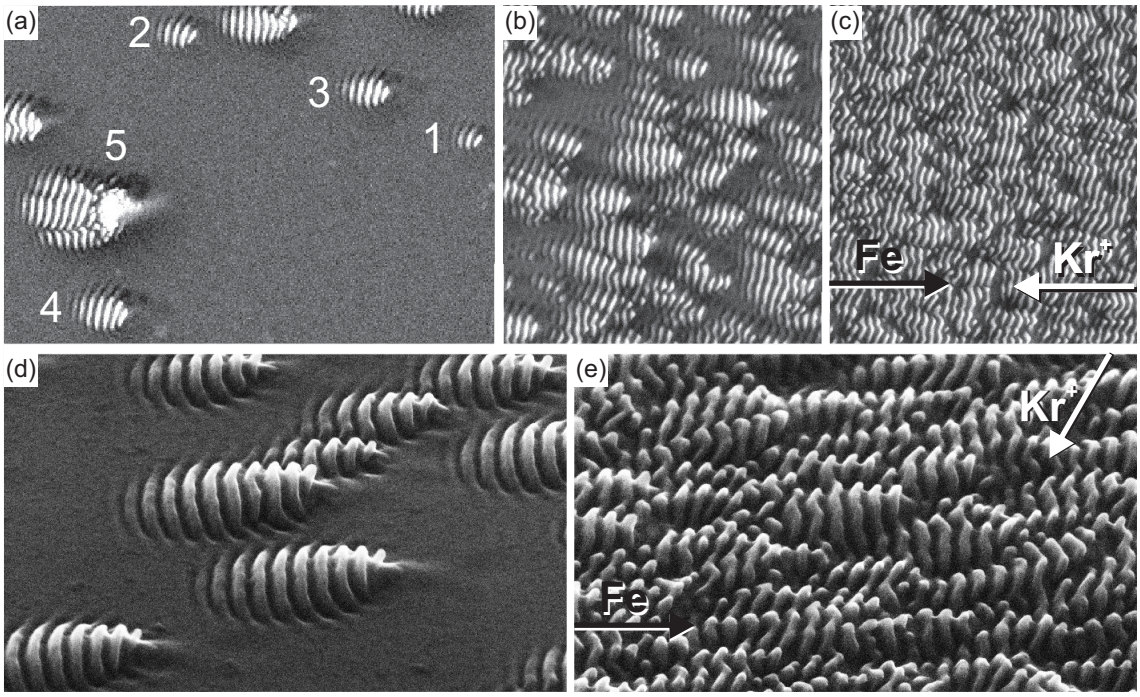

Figure 5.11: SEM images after co-sputter deposition at 440 K. (a)–(c) are top view images taken at (a) $x = 1.12$ mm, (b) $x = 1.19$ mm, (c) $x = 1.24$ mm. The numbers in (a) refer to different stages of pill bug evolution (see text). (d),(e) are tilt-view SEM images. The directions of the incoming co-deposited Fe and Kr^+ are indicated in (c) (projected onto the surface) and in (e). Image widths are (a) 4.4 µm, (b),(c) 2.8 µm and (d),(e) 2 µm.

ure 5.10 after sputter co-deposition at 140 K. With increasing x-coordinate, the flat hole pattern starts to become interrupted by oval-shaped pill bugs [figure 5.11(a)], which become denser and start to coalesce [figure 5.11(b)] until a continuous ripple pattern forms [figure 5.11(c)]. We would like to stress here that for both temperatures there is no coexistence of different evolution levels within the same area. The transition always displays with increasing x-coordinate a monotonic increase of the pill bug concentration until they merge to form a ripple pattern. The x-position of the transition line depends slightly on the y-position, which is likely the result of the finite size and the irregularities of the Fe target.

Figure 5.11(a) highlights also the different stages of pill bug evolution. The

numbers (1) to (4) indicate pill bugs of increasing size containing three to six well developed ridges, respectively. (5) suggests that pill bugs tend to nucleate at surface irregularities. In the presented case (5), it appears that multiple nearby nucleation centres caused the formation of three overlapping pill bugs. The tendency for preferred nucleation of pill bugs at irregularities is supported by the observation of a higher density of pill bugs at a surface scratch (not shown).

The tilt-view SEM images in figure 5.11(d) and (e) make plain, why AFM measurements display roughness variations at the onset of the ripple regime: Not only is the transition from the flat hole pattern to the ripple regime abrupt and inhomogeneous, but the depth of the ripple trenches is very large as well. Their depth is considerably underestimated by AFM due to tip limitations. This makes the observed roughness sensitively dependent on tip sharpness. Therefore the roughness data shown in figure 5.8 has to be considered with care, especially in the range $1\,\mathrm{mm} \leq \mathrm{x} \leq 2\,\mathrm{mm}$. It is visible in the tilt-view SEM images that the ripple ridges are bounded by steep walls almost parallel to the incoming ion beam. The ripple pattern visible in the tilt-view SEM image of figure 5.11(e) displays also a considerable height variation along the ridges, correlated along the x-coordinate. These variations are consistent with the idea that the ripple pattern emerges through coalescence of growing, initially isolated pill bugs.

Figure 5.12 highlights the features of individual pill bugs. The two AFM topographs of figures 5.12(a) and (b) show two pill bugs fabricated at 440 K and 140 K, respectively. Their common features are: (i) Pill bugs have a characteristic extension of 600 nm along the x-coordinate and 300 nm normal to it. (ii) Their maximum height above the flat background is 100 nm – 150 nm. (iii) As shown in the profile of figure 5.12(c), their height linearly slopes down from its maximum value at their head (large x-coordinate) towards their tail (small x-coordinate). (iv) The segmenting of their exoskeleton is uniform with a characteristic wavelength which is slightly temperature dependent. It is 65 nm at 140 K and 75 nm at 440 K. (v) The head of a pill bug usually consists of a short ridge directed precisely towards the ion

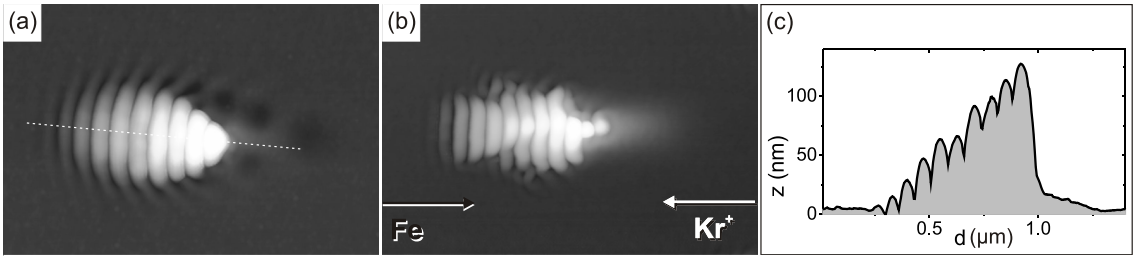

Figure 5.12: (a), (b) AFM images of single pill bugs created at 440 K and 140 K, respectively. The projection of the direction of the incoming co-deposited atoms and of the Kr^+ onto the surface is indicated in (b). Image size in (a) and (b) is 1.5 µm × 1 µm. (c) Height profile along dashed line in (a). Note that due to the large depth of the pill bug trenches (compare figure 5.11), probably the AFM tip does not reach their bottom.

beam [compare SEM image in figure 5.11(d)], i.e. with an angle of 30° with respect to the surface normal. As visible in figure 5.11(d), the segments of the exoskeleton are in fact ridges separated by deep trenches. The ridges are inclined towards the ion beam, similar to the pill bug head. (vi) The pill bugs cause depressions in their surrounding. This is especially visible in figure 5.12(a), where the trenches between the ridges extend into the flat region with depth of 5 nm – 10 nm.

There are slight differences between pill bugs fabricated at different temperatures. Most obvious, pill bugs prepared at 440 K are more regular oval-shaped, while the pill bugs created at 140 K are less regular with a tendency to a triangular appearance. At 440 K, the ridges, trenches, and their extension into the surrounding are slightly curved, with an imaginary centre of curvature on the x-axis somewhere well behind the pill bug head. The trenches extending into the flat area and the depressions in front of the pill bug head remind of patterns caused by the drag of an object through a highly viscous material. The pill bugs appear to be moved backwards, i.e. in the direction of decreasing x-coordinate.

Discussion

The phase boundary between region (I) and region (II) (see figure 5.9) contains patches of highly corrugated area, i.e. the pill bugs, within a sea of flat phase. This observation points to a morphological bifurcation. Inside region (I), all accessible height fluctuations are driven back through the bidirectional ion bombardment. At the edge of region (I), the stabilizing flux of scattered Kr atoms ceases. Still, most fluctuations are driven back by it, but single, rare, and exceptionally large fluctuations bring the system into a strong self-amplification circle of shadowing, silicide formation and corrugation growth around a single height fluctuation. Key to the rapidity of localized pattern formation must be the high Fe flux available in this area.

A possible scenario is sketched in figure 5.13. Starting with a single pointed height fluctuation (i) silicide formation at the exposed flank as well as iron shadowing at the flank pointing to the ion beam take place (ii). The Fe exposed flank is eroded more slowly, rises and quickly becomes so steep that the local angle θ of ion incidence falls beyond the maximum of the erosion rate for Fe at $\theta_p \approx 70°$ (iii). Thereby erosion diminishes and grazing incidence reflection of ions becomes relevant. Focusing of ions to the foot of the protrusion creates a trench in its immediate

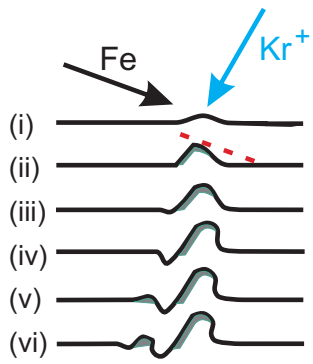

Figure 5.13: Sketch of a pill bug formation scenario. Steps (i)–(vi) are discussed in the text.

surrounding, primarily in its front (iv). While emission of scattered energetic ions is close to the reflection direction, sputtered Fe particles have a broader distribution, but pointed into forward direction [compare figure 5.5(a) and (b)]. Thereby Fe accumulates in front of the trench, an exposed flank forms (v) and the process repeats (vi). Though highly speculative, our model accounts properly for a number of prominent features of the pill bugs. (a) The differing numbers of exoskeleton segments represent simply different stages of their growth which takes place segment by segment. (b) The pointed head of the pill bug and the steep ridges with their flanks nearly parallel to the incoming ion beam [compare Figs. 5.11(d) and (e)] are consistent with the ion reflection assumption. The decreasing height of the pill bugs towards their tail (i.e. towards the Fe flux) as visible in figure 5.12(c) is a natural consequence of their growth process as outlined above. (d) The ridge curvature enclosing the initial height fluctuation is a consequence of the two dimensional distribution of particles scattered from the initial pointed elevation. (e) The key importance of exceptionally large height fluctuations for pill bug formation is underlined by their preferential formation at point [compare figure 5.11(a)] and line defects (e.g. scratches). We note that similar localized rippled objects have already been observed in the past on Si after 20 keV - 40 keV Ar^+ ion bombardment with $\vartheta = 45°$ [109; 166].

Instead of a height fluctuation, one might assume that pill bugs nucleate through the formation of silicide seeds. However, given the absence of crystalline iron silicide on our sample as evidenced by X-ray diffraction and given the high Fe concentration, it is not not easy to imagine why formation of an amorphous silicide seed should be a rare event and why its formation should be so efficiently suppressed through additional scattered Kr atoms in region (I).

Our experiments do not provide a clear fingerprint for the nature of the smoothing mechanism, which is necessary for the selection of a characteristic wavelength. As noted above, the appearance of the pill bug surrounding remind of the pattern caused by the drag of an object through a highly viscous material into the ion beam

direction. Therefore it appears plausible that viscosity of the amorphous layer in conjunction with the surface tension provide the necessary smoothing, in agreement with a recent proposition of Castro and Cuerno [41].

Conclusions

Upon sputter co-deposition, a pattern bifurcation is observed at the location where the flux of scattered Kr atoms ceases. The abruptness and coexistence of fundamentally different patterns side by side indicates that there are conditions where pattern formation does not proceed from a linear to a nonlinear regime, but is a rapid self-accelerated growth process which may be described in terms of pattern nucleation and lateral pattern growth.

5.4 Impurity Assisted Ion Beam Patterning in the Crystalline Phase

Introduction

Our studies on temperature dependence covered in section 5.2 state that the pattern type does not depend on temperature in a wide temperature range (140 K – 440 K). The following results extend the investigation by performing steel co-sputter deposition experiments at a temperature of 660 K where it is expected that the substrate remains crystalline during ion beam erosion.

Results

The co-sputter deposition geometry as well as the ion flux and fluence remain the same as in the experiments at temperatures in the range of 140 K – 440 K (section 5.2). Anyhow, the developed type of pattern morphologies at 660 K differ substantially from the experiments in the lower temperature range.

Figures 5.14 and 5.15 show AFM and SEM images of the resulting surface to-

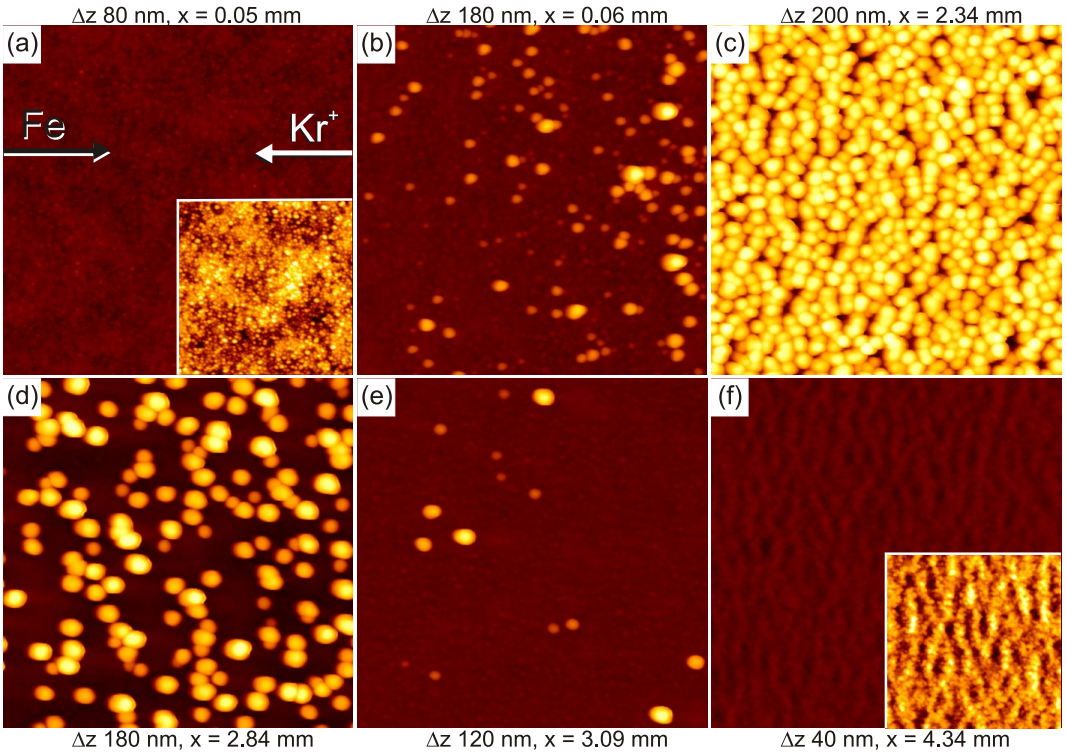

Figure 5.14: AFM images of Si(001) after sputter co-deposition at 660 K depending on distance x. The incoming directions of Kr^+ and Fe for all images are indicated by the white and black arrow in (a), respectively. Size of all images is 2 µm × 2 µm. (a) $x = 0.05$ mm, grained structure, (b) $x = 0.06$ mm, arising nanopillars out of a grained structure, (c) $x = 2.34$ mm, dense packed nanopillars (d) $x = 2.84$ mm separate nanopillars, (e) $x = 3.09$ isolated nanopillars on a grained structured surface and (f) $x = 4.34$ mm, a wave-like structure far away from the steel plate. Insets show the according surface with optimized contrast with size of 1 µm × 1 µm.

pography after an ion fluence of $F \approx 5.9 \times 10^{21}$ ions m^{-2}. We take advantage of the complementary measurement methods. While the AFM is able to give information about the height of topographical features due to a convolution between tip and surface, it typically overestimates their width. Furthermore, for the same reason it is impossible to identify a feature's overhang, if present. On the other hand it is challenging to estimate the feature size with the SEM yet the structures are displayed unaltered and convolution plays no role. Therefore, in the following the

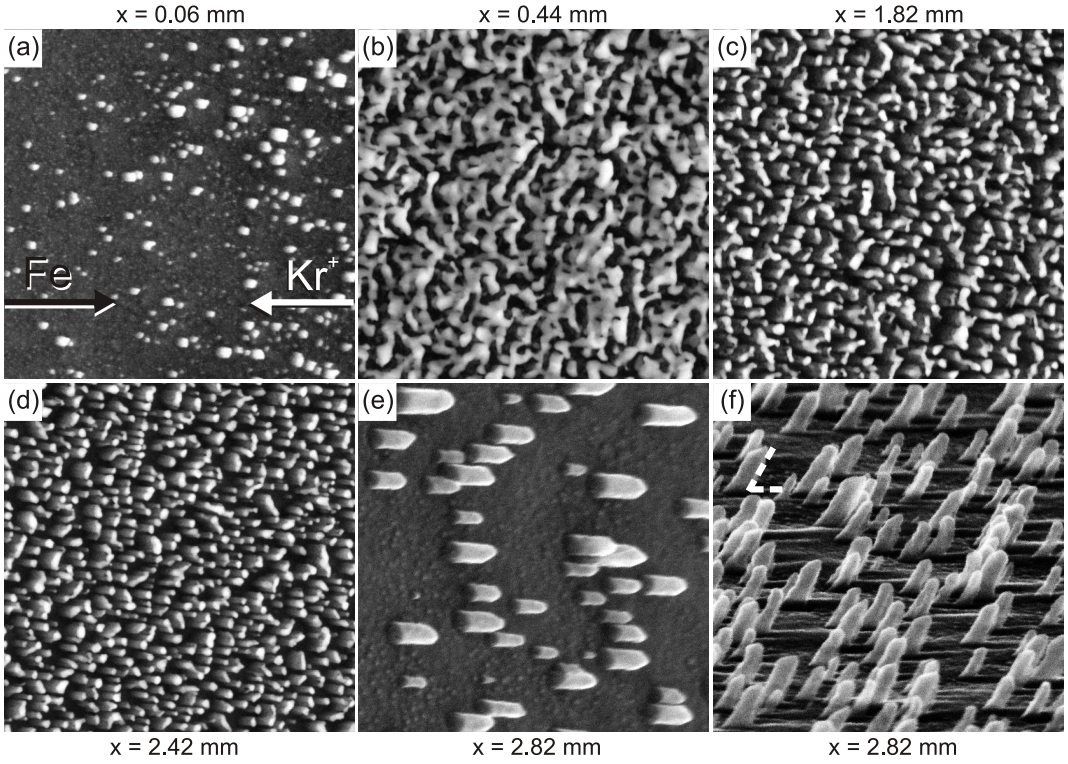

Figure 5.15: SEM images of a steel co-sputter deposition experiment at 660 K with increasing distance x. The incoming directions of Kr^+ and Fe for all images are indicated by the white and black arrow in (a), respectively. (a) $x = 0.06\,\text{mm}$, arising nanopillars, (b) $x = 0.44\,\text{mm}$, sponge like structure, (c) $x = 1.82\,\text{mm}$, transition from the sponge like structure to nanopillars, (d) $x = 2.42\,\text{mm}$, dense packed nanopillars (e) $x = 2.82\,\text{mm}$ separate nanopillars and (f) $x = 2.82\,\text{mm}$, side view of nanopillars (bright dashed lines: angle of 60° between surface normal and pillars). The image width for (a)–(d) is 2 µm and for (e) and (f) 1 µm. Except of (f) perspective of all images is top view.

results of both measurements will be discussed synchronically depending on the distance x relative to the steel plate to get a general view on the observed topographical features.

Close to the steel plate with a distance $x \approx 0.05\,\text{mm}$ a grained surface appears [figure 5.14(a)]. Figures 5.14(b) and 5.15(a) show a comparable region on the sample surface with $x \approx 0.06\,\text{mm}$. The grain size varies strongly so that multiple large grains may be identified as nanopillars growing out of the grained surface. With increasing

distance x the height and density of the nanopillars increases. A rough spongelike structure is found at $x \approx 0.44\,\mathrm{mm}$ as presented in figure 5.15(b). AFM imaging in this range was not possible due to the exceeding roughness and thus resulting images are affected by tip artefacts. The fraction of cavities found in the spongelike structure increases with x. Figure 5.15(c) displays a transition zone between the spongelike structure and nanopillars at a distance $x \approx 1.82\,\mathrm{mm}$. At $x \approx 2.4\,\mathrm{mm}$ separated but densely packed high amplitude nanopillars may be identified [figures 5.14(c) and 5.15(d)]. The amplitude of the nanopillars attains up to 180 nm.

Henceforward the pillar density decreases with x as found in figure 5.14(e) at $x \approx 2.8\,\mathrm{mm}$. The SEM data presented in figure 5.15(e) at $x \approx 3\,\mathrm{mm}$ discloses a cone shaped top of the pillars. A side view of the pillars displayed in figure 5.15(f) ascertains that they point into the direction of the incoming Kr^+ beam. By way of illustration, an angle of 60° is marked (bright dashed lines) in figure 5.15(f) and fits with the direction of the the nanopillars and the surface which is congruent with an ion incidence angle of $\vartheta = 30°$ to the normal.

To characterize the shape of the nanopillars we analyzed AFM and SEM images at $x \approx 2.8\,\mathrm{mm}$. The height of the pillars in this range amounts to $131\,\mathrm{nm} \pm 14\,\mathrm{nm}$ and the width to $113\,\mathrm{nm} \pm 18\,\mathrm{nm}$ (width is overestimated due to tip convolution). Furthermore, we analyzed the angles of the pillar tip within side view SEM images as presented in figure 5.15(f). The local normal of the ion beam facing side of the tip is oriented $50° \pm 16°$ related to the incoming ion beam. The local normal of the Fe influx facing side of the tip is oriented $46° \pm 9°$ related to the incoming ion beam. Thus the average apex angle of the tip from perspective of a side view is about 96°.

Far away from the steel plate at $x = 4.34\,\mathrm{mm}$ where very little Fe is present a shallow wave structure with an amplitude of $\approx 3\,\mathrm{nm}$ with the ripple wave vector $\vec{k}$ parallel to the incoming ion beam develops [figure 5.14(f)].

Figure 5.16 demonstrates the roughness analysis of all temperature dependent co-sputter deposition induced pattern formation experiments depending on the distance x to the steel plate. It can clearly be seen that the roughness curve for the

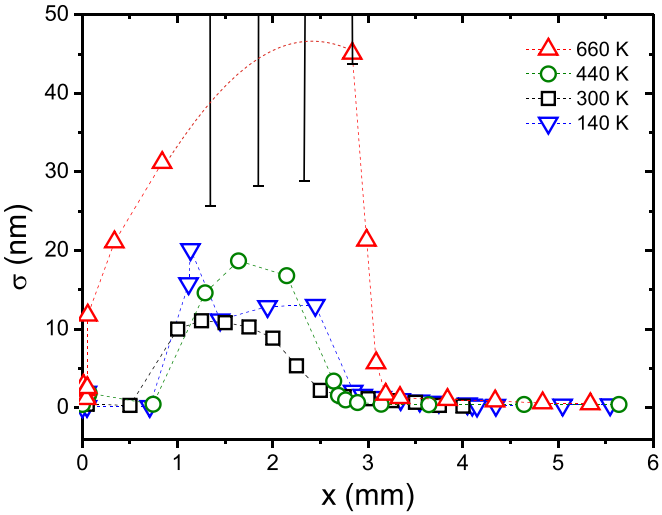

Figure 5.16: Roughness analysis of co-sputter deposition experiments as a function of normal distance x to the stainless steel plate for temperatures indicated. Lines to guide the eye.

experiments between 140 K and 440 K has a comparable progression in shape and height. In contrast the curve representing the 660 K sample roughness differs noticeable with an increased roughness. The roughness shoots up already at positions close to the steel plate. Within the range of a spongelike structure $0.2\,\text{mm} \leq x \leq 1.6\,\text{mm}$ only a minimum roughness could be estimated which is marked by the lower end of the error bars. The real roughness might be far larger. This imprecision is a result of narrow gaps found in the sponge like structure and dense packed nanopillars where the AFM-tip could not penetrate deep enough. At distances $x > 3.2\,\text{mm}$ the roughness of the 660 K curve is marginally higher than for the experiments performed at temperatures between 140 K and 440 K.

We performed grazing-incidence X-ray diffraction (GI-XRD) experiments on the samples sputtered at 440 K and 660 K. For the sample treated at 440 K no crystalline structures could be detected, i.e. a possible X-ray diffraction signal is below the detection limit.

A different situation presents itself for the sample treated at 660 K. Figure 5.17

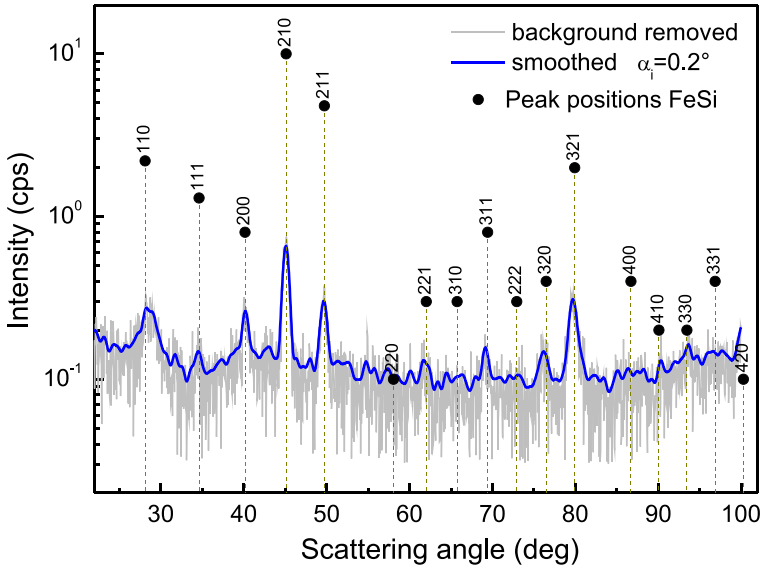

Figure 5.17: GI-XRD diffraction curve for the Si(001) sample eroded by the sputter co-deposition method at 660 K. The blue intensity curve over the scattering angle shows the smoothed X-ray scattering intensity after removal of the background signal (grey). Several characteristic peak positions of FeSi are marked within the diagram (black dots).

shows GI-XRD results where an FeSi diffraction signal is found. Prior to the X-ray diffraction measurement the critical angle of total external reflection of the sample was determined to $\alpha_i^{max} = 0.27°$. The measurements were carried out slightly below that value at $\alpha_i = 0.20°$. Under these conditions the evanescent X-ray wave propagates predominantly at the sample surface so that it is highly sensitive to the surface structure and at the same time less sensitive to bulk scattering.

Figure 5.17 shows the grazing incidence diffraction pattern after removing the background. The black dots show the positions and the relative intensity of a theoretical cubic ε-FeSi structure with a lattice constant of 4.488 Å in a B20 configuration. At least six of the most intense FeSi peaks could be observed. From the measured intensity distribution a powder like phase and an average crystallite size of about 20 nm could be estimated.

As the Fe content changes with the distance x relative to the steel target we addi-

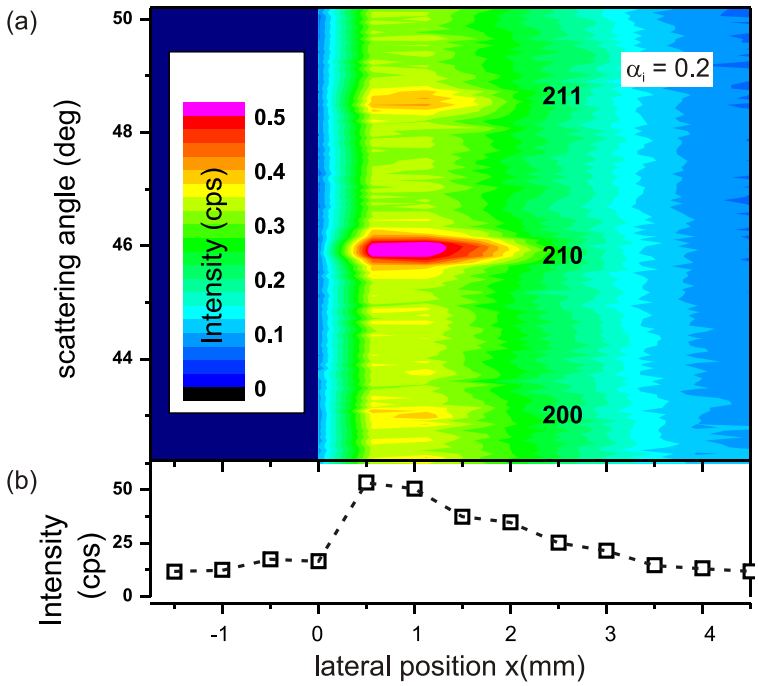

Figure 5.18: GI-XRD signal of the Si(001) sample eroded by the co-sputter deposition method at 660 K. (a) Spatially resolved GI-XRD signal. (b) Intensity curve of the (210) peak depending on the position x. Position $x = 0$ corresponds to the position of the steel plate.

tionally carried out a position dependent diffraction measurement along x. Thereby the X-ray beam crossed the patterned area parallel to the steel plate. The results are presented in figure 5.18(a) where the intensity of the (211), (210) and (200) FeSi peaks depending on x are clearly visible. Additionally figure 5.18(b) shows the intensity of the (210) peak, the most pronounced peak, depending on x. A maximum in intensity is found in the Fe rich range of the spongelike structure 0.2 mm$\leq x \leq$1.6 mm decaying with increasing x just as the fraction of cavities increases [compare figures 5.15(b)–(d)]. At a distance $x \approx 2.4$ mm the diffraction intensity falls below the detection limit.

To get a better understanding of the Fe distribution within the structures transmission electron microscopy (TEM) measurements were performed. Figure 5.19(a) shows a TEM image of a lamella cut out by focused ion beam (FIB) at position

$x \approx 0.45\,\mathrm{mm}$ displaying a side view of the spongelike structure. The features are composed of patches differing in brightness which is an indication for differently oriented crystallites. A coarse substrate below the spongelike features is visible. Separated pillars appear in figures 5.19(b) and (c) at positions $x \approx 1.80\,\mathrm{mm}$ and $x \approx 2.45\,\mathrm{mm}$, respectively. As already presented in the SEM images of figure 5.15(f) the pillars point into the direction of the incoming Kr^+ beam.

Figure 5.19(d) is the result of an image subtraction of two energy filtered TEM images recorded with electron energies just below and above the excitation energy (K_α edge) of Fe. Thus the bright areas in the subtracted image represent a high Fe content. As figures 5.19(a) and (d) are recorded at the same sample position, comparison of the images reveals the Fe to be distributed entirely within the spongelike features. High resolution TEM analyses within the structures presented in figures 5.19(a) and (b) confirms an FeSi structure as found by GI-XRD measurements.

A TEM image of an isolated pillar at $x = 2.45\,\mathrm{mm}$ is shown in figure 5.19(e). Again the patches of different brightness indicate differently oriented crystallites. Two areas are framed by white boxes. Within these areas high resolution TEM images were recorded which are presented in figure 5.19(f). Both areas show an ordered crystalline structure. The according fast fourier transformation (FFT) images are displayed in figure 5.19(g). From the distance and orientation of the FFT spots the crystal lattice structure can be estimated. The FFT image corresponding to the upper part of the pillar with clearly defined spots has a rather complex structure and does not fit to any common iron-silicide [1] structure nor to pure Fe or Si. According data fits of the FFT spots suggest rather a tetragonal $FeSi_2$ or a distorted Fe_2Si structure but both assumptions should be viewed with caution. The FFT analysis of the bottom part of the pillar shows spots according to pure Si oriented in the substrate direction which is Si(001).

[1] Please note that in the following we use the term "iron-silicide" as a generic term for all possible Fe-silicide compositions, while "FeSi" stands for the specific Fe-silicide with an Fe to Si proportion of 1:1.

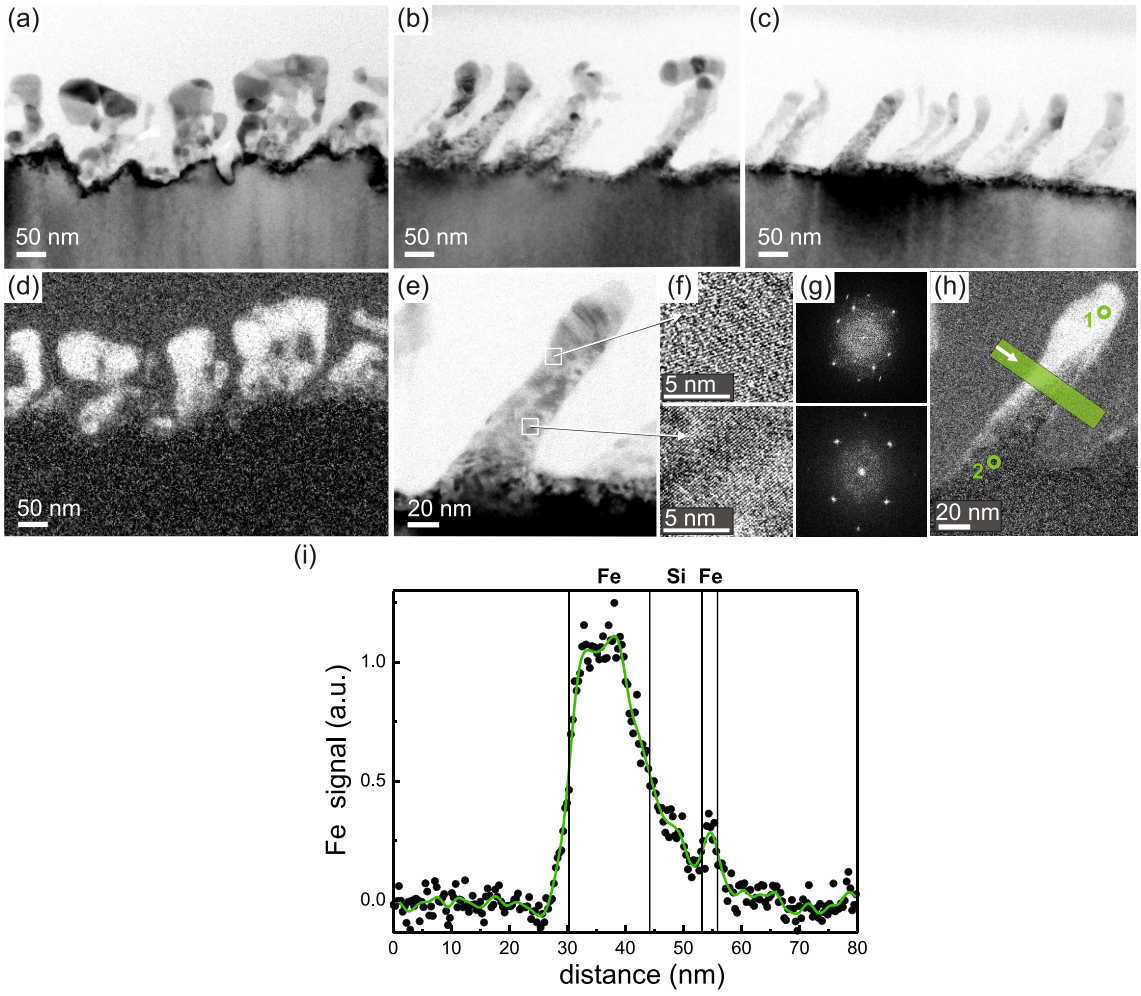

Figure 5.19: TEM analysis conducted of the Si sample sputtered at 660 K in the co-sputter deposition geometry. TEM imaging positions are in (a) $x = 0.45\,\mathrm{mm}$, (b) $x = 1.80\,\mathrm{mm}$, and (c) $x = 2.45\,\mathrm{mm}$. (d) image subtraction of energy filtered TEM measurements: bright regions represent a high Fe content (see text), position x corresponds to (a). (e) TEM image of a nanopillar at $x = 2.45\,\mathrm{mm}$. (f) High resolution TEM images of areas bordered in (e). (g) FFT analysis of regions displayed in (f). (h) Image subtraction of energy filtered TEM measurements of the pillar presented in (e). (i) EELS line scan across the pillar along the green line in (h).

Figure 5.19(h) displays the result of an image subtraction of energy filtered TEM images of the pillar shown in figure 5.19(e); again the bright regions represent areas

with high Fe content. It is conspicuous here that the top of the pillar is Fe rich while the bottom contains no significant amount of Fe. A straight border of the Fe rich pillar region is visible. It crosses the pillar diagonally from the lower part of the pillar on the Fe influx facing side to the upper part of the pillar on the Fe influx averted side. Energy-dispersive X-ray spectroscopy (EDX) was conducted at the top and bottom of the pillar (point 1 and 2, respectively) underlining once again that the Fe content is considerable higher in the region at the top of the pillar compared to the bottom of the pillar (EDX spectra not shown here).

Figure 5.19(i) shows an EELS line scan along the green line in figure 5.19(h) in direction of the indicated white arrow. It is evident that there is a sharp border changing from high Fe content to low Fe content from the Fe influx facing side of the pillar to the Fe influx averted side, respectively. Looking more precisely at the EELS line scan in figure 5.19(i) another yet smaller Fe peak is present disclosing that Fe was even deposited to the Fe influx averted side.

Discussion

The presented results show that the pattern types observed at 660 K differ considerably from the pattern types found between 140 K and 440 K. The pattern amplitude is considerably higher at 660 K which is in particular characterized by the roughness curve (figure 5.16).

It is conspicuous that the roughness curve of the 660 K measurement correlates with the Fe content as it was observed at lower temperatures; whereupon at 660 K the effect is more pronounced. According to the roughness curve in figure 5.16 the largest Fe signal intensity within the GI-XRD measurement is found in the range of the spongelike structure and decreasing with further increasing x.

Another connection of the high temperature patterns to low temperature patterns might be noticeable: The pillars can be considered as high amplitude dots and the transition from pillars to a spongelike structure reminds of the transition from dots to ripples at lower temperatures.

We consider the substrate crystallinity as main qualitative difference between the experiments performed at temperatures in the range of 140 K – 440 K and at 660 K. The GI-XRD measurement constitutes that between 440 K and 660 K there must be a transition from a stable amorphous surface to a stable crystalline surface during ion bombardment.

The high aspect ratio of the spongelike structure and pillars leads to the assumption that at 660 K a real growth process must be involved since atoms cannot be sputtered from the narrow slits in between densely spaced pillars [167]. Furthermore, TEM measurements disclose that the substrate is undulated with mounds below the features and valleys at the structure cavities [figure 5.19(a)]. This might be an indication that during the sputtering process Si rearranges and moves towards the features.

Contrary to amorphous surfaces on crystalline substrates the presence of step edges may change the surface diffusion dynamics. Schwoebel [168] elaborated upon subject of interlayer transport of mobile adatoms across partial layers or islands on crystalline surfaces. Atomic steps on a surface may interact with surface diffusing atoms in a repulsive or attractive sense: For instance the downward atomic jump to the next lowest layer might be inhibited by an interlayer transport energy barrier and hence lead to a roughening.

The influence of the so-called *Ehrlich-Schwoebel diffusion barrier* on ion beam pattern formation was discussed recapitulatory by Chan and Chason [28]. In our context we consider a combination of erosion and a growth mechanism which is a very complex situation. However, the main point is that we want to emphasize here that the surface dynamics during sputtering on amorphous and crystalline surfaces are driven by differing principles.

Our X-ray analysis discloses that we may distinguish two regions. In the range of the spongelike structure a powderlike but homogeneous FeSi phase was found by GI-XRD measurements. The high resolution TEM analysis for $x > 2.4\,\mathrm{mm}$ confirms variably oriented crystallites but the composition and structure can not be

determined unequivocally. A distorted iron-silicide unit cell might be plausible due to a possible composition gradient throughout the pillar. Moreover, the additional relative small Cr content stemming from the steel target could also modify the structure of the crystallites.

Interestingly, TEM and EDX measurements show that within the spongelike structure the Fe is entirely distributed. Otherwise the pillars contain Fe primarily on the Fe influx facing side. This different behaviour makes it difficult to understand the present pattern formation process. While the homogeneous Fe content in the spongelike structure indicates a balanced pattern formation mechanism, the composition of the pillar is suggestive of segregation or shadowing effects. Correspondingly, the present Fe on the Fe influx averted pillar side may be explained by redeposition of sputtered material from a pillar positioned next to the investigated one.

It should be noted that a closer examination of the pillar shape in figure 5.19(c) reveals that some of the pillars are bent upwards. This feature is not found in previous SEM images [figure 5.15(f)]. A simple reason could be that before TEM measurements some of the pillars were deformed during sample transport or sample preparation. Another more interesting but speculative assumption is that after the erosion process the sample cooled down to room temperature and the pillar itself acted due to its composition like a bimetallic strip. Hence the thermally induced stress bent the pillar upwards. In fact the coefficient of thermal expansion of ε-FeSi [169] is by a factor of 16 higher than the thermal expansion coefficient of Si ([170], p. 672 ff.).

Finally, from a visual point of view the processed surface appears black as seen by the naked eye [see figure 3.3(b)]. This is an evidence for an enhanced absorbance. Zhou et al. demonstrated that their high aspect ratio cones, processed with a similar co-sputter deposition setup, reduce the reflectivity and thus increase the absorbance of their surface by 25% [143]. The reduced reflectivity may be attributed to the high aspect ratio of the features which enables multiple scattering of the incoming light

and a continuously increasing refractive index from top to bottom of the patterned film.

Conclusions

Metal assisted ion beam pattern formation at high temperatures gives rise to crystalline, high aspect ratio patterns. As a result a spongelike structure and nanopillars were observed. The patterns differ notably from patterns generated at room temperature. X-Ray and TEM measurements reveal that iron-silicides have formed.

The resulting surface with an increased absorbance reveals its potential to serve as an anti-reflection coating and thus being very promising for optimizing solar cells [4–6] or optoelectronic devices [12; 13].

Furthermore, the combination of a patterned surface consisting of iron silicides might be of technological relevance as in particular β-$FeSi_2$ is known for its photoluminescent properties [171]; thereby the β-$FeSi_2$ was fabricated by ion beam synthesis [172; 173] or by annealing $FeSi_2$ films [174].

5.5 Impurity to Ion Flux Ratio Dependence

Introduction

Co-sputter deposition experiments are a good way to get an overview of possible patterns by a variation of several parameters in one experiment. The disadvantage of co-sputter deposition experiments is the high complexity due to several pattern formation mechanisms taking place simultaneously. Locally there is a gradient in the impurity flux attended by a distribution in the kinetic energy of the impurities. Additionally reflected ions appear close to the steel plate.

In order to gain a deeper understanding of the pattern formation mechanism and to disentangle the effects of a second chemical species with additional energy from a second direction (the latter being at variance with the primary ion beam direction), dedicated experiments are necessary. Therefore, we designed a situation

where the second chemical species is deposited with thermal energies (i.e. through physical vapor deposition) simultaneously with a clean eroding ion beam. Such an experiment might also be able to establish whether the direction of the impinging co-deposited particles with respect to the ion beam and the sample surface is of relevance - irrespective of the energy of the co-deposited particles. Furthermore, co-evaporation experiments enable a tunable impurity flux. Hence investigations on the influence of the impurity-to-ion flux ratio may be conducted.

Within region (II) (see figure 5.9), where the concentration of sputter co-deposited steel gradually vanishes to zero with increasing x-coordinate, smooth pattern transitions from ripples to dots to a flat surface are observed. One may therefore speculate, that these pattern transitions are caused by the decreasing ratio of arriving sputter co-deposited Fe versus primary Kr^+. To test this hypothesis we conducted dedicated experiments, where we controlled the concentration and angle of incidence of the arriving co-deposited material. In these experiments stainless steel was evaporated onto the Si sample while it was ion beam eroded. The stainless steel plate and consequently sputter co-deposition were absent.

Results

We sputtered a Si(001) sample at $\vartheta = 30°$ with simultaneous co-evaporation of Fe. As shown in figure 5.20(a), the ion beam direction was not changed compared to the sputter co-deposition situation and Fe impinges at an angle of incidence of 75° with respect to the surface normal. Though being well defined, this angle is a rough approximation to the angular distribution of incidence for Fe in the sputter co-deposition experiments for $x = 1\,\text{mm} - 4.5\,\text{mm}$ [see figure 5.1(a)].

Figure 5.20(b) shows a ripple pattern generated with an Φ_{Fe}/Φ_{Kr^+} flux ratio of 4%. We estimate the characteristic pattern wavelength to $\Lambda \approx 51\,\text{nm}$ and the surface roughness amounts to 8.7 nm.

A flux ratio of $\Phi_{Fe}/\Phi_{Kr^+} = 3\%$ leads to a nanodot pattern with a characteristic pattern wavelength of $\Lambda \approx 38\,\text{nm}$ and a roughness of $\sigma = 0.6\,\text{nm}$.

Figure 5.21 shows SEM images of a ripple pattern developed with a Φ_{Fe}/Φ_{Kr^+} flux ratio of 8%. AFM measurements (not shown here) amount the characteristic pattern wavelength to $\Lambda \approx 86\,\text{nm}$ and the roughness of the sample surface to $\sigma \approx 10.7\,\text{nm}$. A dust particle which was present already previous to erosion shadowed the incoming Fe atoms. In the shadowed area behind the dust particle even with ion erosion no patterns develop due to absent Fe [figure 5.21(a)]. The transition zone of an Fe exposed area towards an Fe absent area is imaged in figure 5.21(b). A decrease in the ripple wavelength and ripple amplitude is obtained with decreasing flux of Fe. Rudimentary some nanodots are visible.

Discussion

The sequence of patterns with decreasing flux ratio Φ_{Fe}/Φ_{Kr^+} represented by figures 5.20(b)–(d) is the same as the sequence of patterns obtained within region (II) with increasing x-coordinate in sputter co-deposition. This similarity is high-

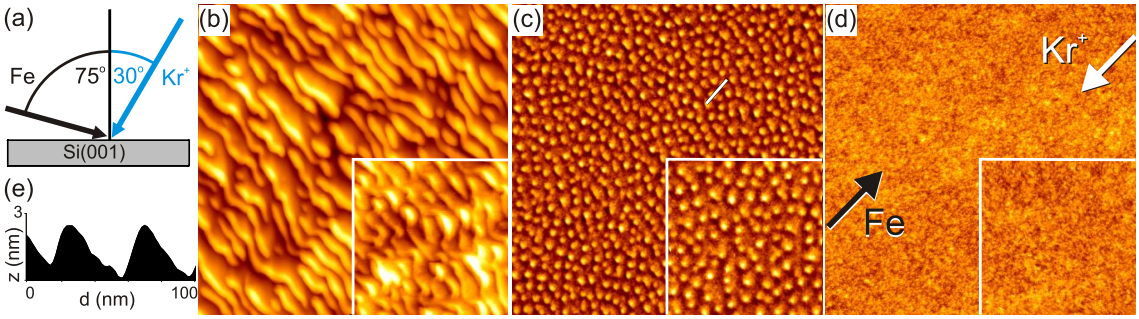

Figure 5.20: (a) Sketch of deposition geometry for co-evaporation experiments. (b)–(d) STM topographs after co-evaporation during a fluence of $6 \times 10^{21}\,\text{ions}\,\text{m}^{-2}$ of 2 keV Kr^+ at 300 K. Atom-to-ion flux ratios are (a) $\Phi_{Fe}/\Phi_{Kr^+} = 4\%$, (c) $\Phi_{Fe}/\Phi_{Kr^+} = 3\%$ and (d) $\Phi_{Fe}/\Phi_{Kr^+} = 1\%$. The black and white arrow in (d) indicate the direction of incoming Fe and Kr^+, respectively. Height differences Δz spanned by the image contrast are (b) 56 nm, (c) 4 nm and (d) 2 nm. Image size is always 1 µm × 1 µm. Insets show corresponding STM topographs obtained after sputter co-deposition at 300 K. Inset sizes are 0.5 µm × 0.5 µm. (e) Height profile along white line in (c).

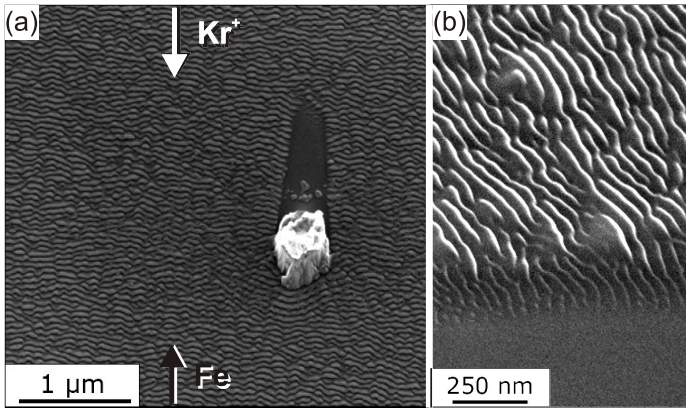

Figure 5.21: SEM images of the co-evaporation experiment sketched in figure 5.20(a) with a Φ_{Fe}/Φ_{Kr^+} flux ratio of 8%. (a) A dust particle present already before erosion shadows the impinging Fe. (b) Transition zone of a shadowing area: With decreasing Fe concentration the pattern disappears.

lighted by the insets of Figs. 5.20(b)–(d), which are taken from the 300 K sputter co-deposition experiment. Even the asymmetric shapes of the pattern features (dots, ripples) with a steep flank facing the co-deposited Fe flux is similar. This is highlighted by a height profile through dots in figure 5.20(c), which is shown in figure 5.20(e).

Both, the concentration dependent co-evaporation experiments presented in figures 5.20(b)–(d) and the transition zone displayed in figure 5.21(b) demonstrate, that the characteristic pattern wavelength Λ increases with an increasing Φ_{Fe}/Φ_{Kr^+} flux ratio.

Conclusions

Comparison of our co-sputter deposition experiments of stainless steel on Si with our Φ_{Fe}/Φ_{Kr^+} flux ratio dependent co-evaporation experiments reveal that details of the angular and energy distribution of the impinging Fe are irrelevant, as long as the global direction of Fe impingement and the ion beam parameters are the same. We find here the flux ratio Φ_{Fe}/Φ_{Kr^+} to be a key parameter determining the resulting pattern as well as affecting the characteristic pattern wavelength Λ.

5.6 Fluence Dependent Pattern Evolution

Introduction

In the present chapter we will show fluence dependent measurements to disclose the metal assisted ion beam pattern evolution with sputtering time. For the sequence of fluence dependent experiments in the presence of metal impurities we use the well defined method of co-evaporation by the setup presented in figure 5.20(a).

Results

The Si(001) sample was irradiated with 2 keV Kr^+ ions with a global angle of incidence of $\vartheta = 30°$. Under these circumstances without metal co-deposition the surface would remain flat. During ion erosion Fe was co-evaporated from $\vartheta = 75°$ to the normal, opposite to the incoming direction of the ion beam. The Φ_{Fe}/Φ_{Kr^+} flux ratio is always $\Phi_{Fe}/\Phi_{Kr^+} \approx 4\%$. According to figure 5.20(d) for the given flux ratio a ripple pattern is expected to develop.

Figures 5.22(a)–(d) show scanning probe microscopy images by using the same image corrugation Δz of 60 nm for all images. Figures 5.22(e)–(h) show profiles along the according lines in the above topography images. After a low fluence of $F \approx 0.2 \times 10^{21}\,\mathrm{ions\,m^{-2}}$ the surface remains flat with a roughness of $\sigma \approx 0.3\,\mathrm{nm}$ [figures 5.22(a) and (e)] which is in the range of the initial roughness preliminary ion bombardment. The inset shows the same experiment on smaller scale with optimized contrast disclosing the general random structure of a smooth amorphous silicon surface. Figure 5.22(b) shows the same sample after a fluence of $F \approx 0.7 \times 10^{21}\mathrm{ions\,m^{-2}}$. A small amplitude ripple pattern with a wavelength of $\Lambda = 38 \pm 9\,\mathrm{nm}$ oriented perpendicular to the incoming ion beam is already visible. The roughness equates to $\sigma \approx 1.3\,\mathrm{nm}$. The profile in figure 5.22(b) discloses that already in this initial pattern formation stage the ripple shape is asymmetric. With increasing sputtering time at a fluence of $F \approx 2.0 \times 10^{21}\mathrm{ions\,m^{-2}}$ [figure 5.22(c) and (g)]

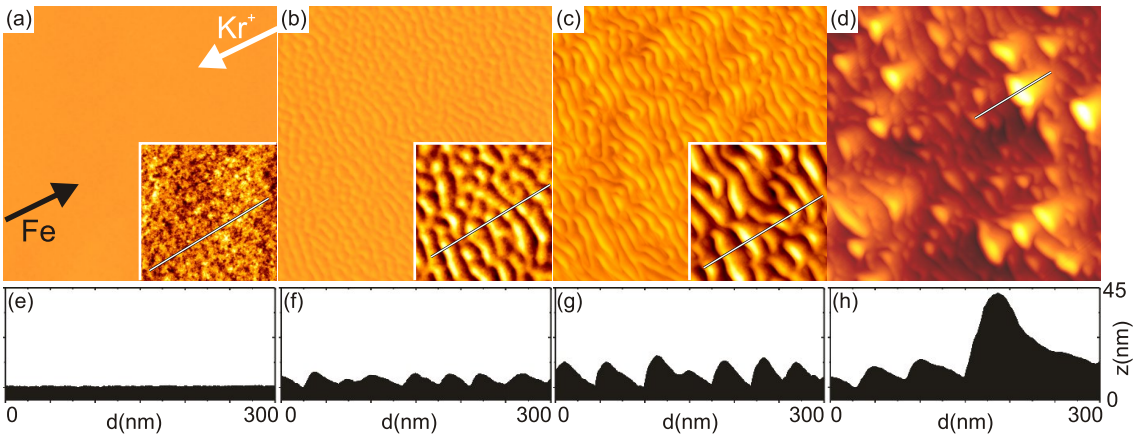

Figure 5.22: (a)–(c) STM images and (d) AFM image of Si(100) after a fluence of (a) $F \approx 0.2 \times 10^{21}\,\mathrm{ions\,m^{-2}}$, (b) $F \approx 0.7 \times 10^{21}\,\mathrm{ions\,m^{-2}}$, (c) $F \approx 2.0 \times 10^{21}\,\mathrm{ions\,m^{-2}}$, and (d) $F \approx 6.9 \times 10^{21}\,\mathrm{ions\,m^{-2}}$ with 2 keV Kr^+ at 300 K. The global angle of incidence ϑ with respect to the surface normal is 30°. Fe was co-evaporated during sputtering opposite to the Kr^+-beam at glancing incidence of 75°. The Φ_{Fe}/Φ_{Kr^+} flux ratio is always $\approx 4\%$ The image size is 1 µm × 1 µm. The white and black arrow indicate the direction of incoming Kr^+ and Fe for (a)–(d), respectively. The image corrugation in (a)–(d) is $\Delta z = 60\,\mathrm{nm}$. Insets show the same experiment with optimized contrast and size of 300 nm × 300 nm. (e)–(h) show a surface profile along the according lines in (a)–(d).

the ripple pattern amplitude grows resulting in a roughness of $\sigma \approx 3.4\,\mathrm{nm}$ and a characteristic pattern wavelength of $\Lambda = 41 \pm 10\,\mathrm{nm}$, the ripple asymmetry emerges as well. While in the so far considered fluence range the pattern itself is very homogeneous with further increasing fluence of $F \approx 6.9 \times 10^{21}\,\mathrm{ions\,m^{-2}}$ displayed in figure 5.22(d) and (h) the pattern coarsens accompanied by a loss of regularity. Neither the pattern amplitude attended by a roughness of $\sigma \approx 7.8\,\mathrm{nm}$ nor the unsteady pattern wavelength of $\Lambda = 64 \pm 30\,\mathrm{nm}$ stays uniform. The statistical evaluation of figure 5.22(d) turns out that small structures with wavelengths of about $\Lambda \approx 60\,\mathrm{nm}$ are of a height of $\approx 10\,\mathrm{nm}$ while large structures with wavelengths of about $\Lambda \approx 180\,\mathrm{nm}$ are of a height exceeding 50 nm [155].

Figure 5.23(a) illustrates the fluence dependent roughness σ and wavelength Λ

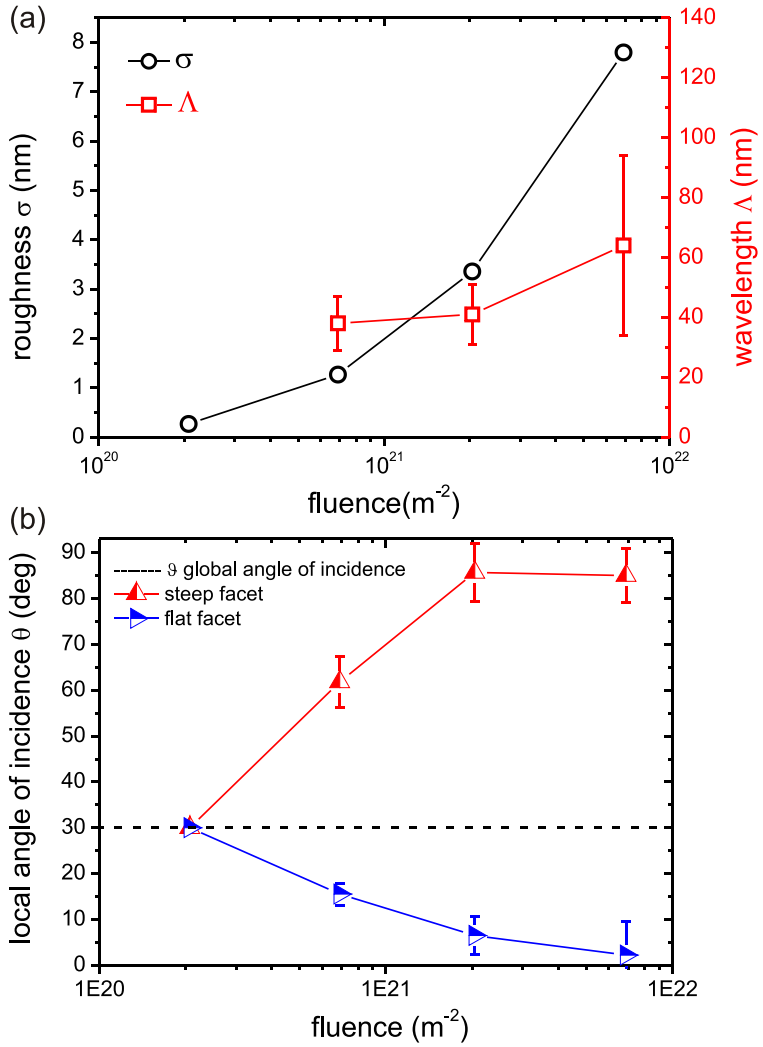

Figure 5.23: Analysis of fluence dependent co-evaporation measurements with 2 keV Kr^+ at $\vartheta = 30°$ on Si(001). The Fe influx is directed 75° to the normal opposite to the incoming Kr^+. (a) Roughness σ (black circles) and facet wavelength Λ (red squares) as a function of the fluence for the experiments represented by figure 5.22. (b) Facet angle analysis of STM images presented in figure 5.22. Blue sidewards and red upside oriented triangles show the local angle of incidence θ of the flat and steep facet, respectively (lines are to guide the eyes). The dashed line crossing $\theta = 30°$ assigns the global angle of incidence of the incoming ion beam.

evolution already discussed in the last paragraph. Both σ and Λ are strictly monotonic increasing with fluence. Furthermore, the error bars in the determination of the

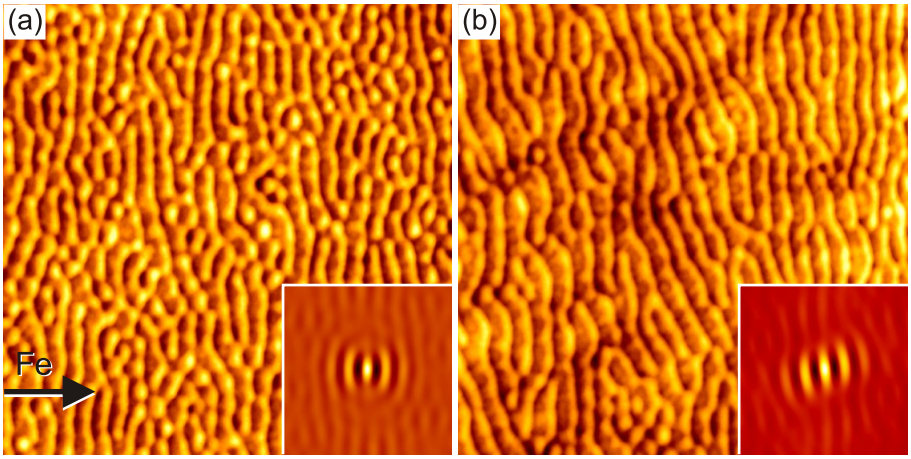

Figure 5.24: STM images of Si(100) after 2 keV Kr^+ bombardment with a fluence of (a) $F \approx 7 \times 10^{21}$ ions m^{-2}, (b) $F \approx 14 \times 10^{21}$ ions m^{-2} at 300 K. Kr^+ was incoming normal to the Si surface. Fe was co-evaporated during sputtering at near normal incidence of 30°. The Φ_{Fe}/Φ_{Kr^+} flux ratio is $\approx 15\%$. The image size is 1.6 µm × 1.6 µm. The black arrow indicates the direction of incoming Fe. The corrugation Δz is 20 nm. Insets show a detail of the self correlation (600 nm × 600 nm) of the presented STM images.

characteristic pattern wavelength are increasing with fluence, showing the standard deviation of the wavelength which is a measure for the pattern regularity.

The resulting facet analysis of the fluence dependent ripple patterns is shown in figure 5.23(b). Starting from a flat and not patterned surface at low fluences of $F \approx 0.2 \times 10^{21}$ ions m^{-2} with increasing fluence ripples develop. At a fluence of $F \approx 0.7 \times 10^{21}$ ions m^{-2} one facet is tilted away of the ion beam forming a steep facet with a local angle of incidence of $\theta_1 = 62° \pm 6°$. The other facet is tilted towards the ion beam forming a flat facet with a local angle of incidence of $\theta_2 = 16° \pm 2°$. With increasing fluence the facets divide. At a fluence of $F \approx 2.0 \times 10^{21}$ ions m^{-2} the local angle of the facets amounts to $\theta_1 = 86° \pm 6°$ and $\theta_2 = 6° \pm 4°$ for the steep and the flat facet, respectively. As in the facet evolution stage both fluence dependent facet angles θ_1 and θ_2 are located on a straight line within the logarithmic plot of figure 5.23(b), the facet's inclining velocity is proportional to the logarithm of the fluence. Even though at the last measured fluence step of $F \approx 6.9 \times 10^{21}$ ions m^{-2}

the ripple pattern lost its uniformity, the facet angles do change only marginally nevertheless. This indicates that the facet angles reached a stable state with $\theta_1 = 85° \pm 6°$ for the steep and $\theta_2 = 2° \pm 7°$ for the flat facet.

In contrast more regular patterns evolve changing the incident angles of the ion and impurity source. Figure 5.24 shows experimental results of an experiment conducted with 2 keV Kr^+ impinging normal to the Si surface and Fe deposited by co-evaporation incoming from 30° to the normal. The flux ratio is $\Phi_{Fe}/\Phi_{Kr^+} \approx 15\%$. (a) and (b) show STM images of the same sample after a fluence of $F \approx 7 \times 10^{21}\,\mathrm{ions\,m^{-2}}$ and $F \approx 14 \times 10^{21}\,\mathrm{ions\,m^{-2}}$, respectively. At the investigated relative high fluences both the steep and flat facet keep nearly constant even though the fluence is doubled. The flat facet changes its orientation marginally related to the Kr^+ beam from $21° \pm 4°$ to $22° \pm 4°$ as the steep facet does from $34° \pm 5°$ to $33° \pm 4°$. So that in relation to the incoming Fe the local angle of incidence on the flat facet is oriented $\theta_{Fe} \approx 8° \pm 4°$ while the steep facet is oriented $\theta_{Fe} \approx 63° \pm 4°$ towards the incoming Fe. As well the change in the ripple wavelength with increasing fluence is insignificant from $\Lambda \approx 68° \pm 8°$ to $\Lambda \approx 67° \pm 9°$ and roughness from $\sigma \approx 2.9\,\mathrm{nm}$ to $\sigma \approx 3.0\,\mathrm{nm}$.

Discussion

The fluence dependent measurements presented in figure 5.22 show that the type of pattern is already selected in the early stage of pattern formation. At high fluences $F \geq 2 \times 10^{21}\,\mathrm{ions\,m^{-2}}$ the ripple pattern coarsens accompanied by a loss of regularity. Presumably the pattern formation process is governed by the Hauffe coarsening mechanism at the steep facet and by shadowing at the flat facet (see figures 2.4 and 2.5).

In the following we want to discuss the coarsening mechanism of the fluence dependent measurements in detail by means of figure 5.25. The local angle of incoming ions at the steep facet amounts to $\theta_1 = 85° \pm 6°$ which is nearly grazing. For the given sputtering geometry the increased number of reflected ions at the steep

facet enhances erosion at the foot of the facet (emphasized by blue dotted lines on the flat facets, see figure 5.25). Therefore, the steep facet increases with sputtering time. Expanded steep facets have a larger ion capture region compared to short steep facets so that due to the Hauffe coarsening mechanism the erosion by reflected ions nearby the former is higher.

Additionally shadowing of the incoming Fe contributes to pattern coarsening which will be explained with the help of figure 5.25. The Fe atoms solely arrive at the steep facets pointing towards the incoming Fe. Assuming that height fluctuations of the ripples are present according to the borders of the grey area in figure 5.25, the Fe accumulates at the steep facet (green area). The red dashed line shows the shadowed area induced by the leftmost *ridge 1*. It is obvious that no Fe reaches the small *ridge 2*. The facets growth velocity depends on the Fe deposition rate, so that the facet growth velocities v are $v_2 = 0$ and $v_1, v_3 \neq 0$ labelled with the indices of the ridges according to figure 5.25. From this it follows that with increasing time *ridge 3* will swallow *ridge 2* and *ridge 1* increases laterally by the width of *ridge 2*.

As a result both the steep and the flat facets of *ridge 1* will increase with fluence and large structures grow at the expense of small structures. The dashed grey line represents the expected shape of the considered surface segment after a certain

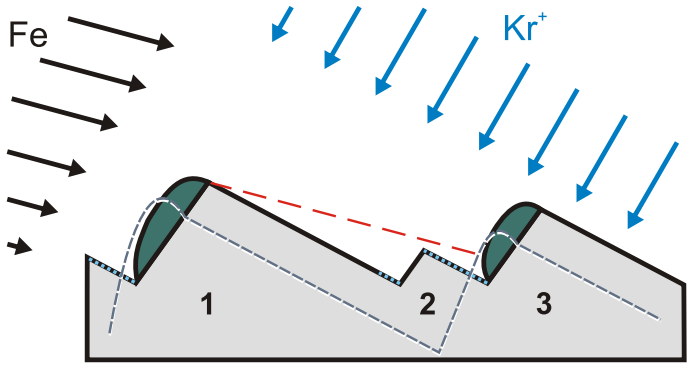

Figure 5.25: Sketch of the pattern coarsening mechanism induced by shadowing (see text).

time of Fe and Kr^+ exposure. As discussed *ridge 2* disappeared. Furthermore, it is conspicuous that the facet ridge is outwardly bulged which is a result of the expected lower erosion velocity of iron-silicide rich regions compared to pure silicon (see section 5.8).

Comparing the results of the fluence dependent measurements given in figure 5.22(d) and figure 5.24(a) it is conspicuous that we find a different behaviour. Even though the fluence of the two above mentioned experiments is comparable and the Fe to Kr flux ratio with Φ_{Fe}/Φ_{Kr^+} ≈15% of the latter is higher in comparison to the discussed sequence of figure 5.22 with Φ_{Fe}/Φ_{Kr^+} ≈4% the pattern is more regular and stable to coarsening with increasing fluence. The reason for this may be found in the difference in the geometry of the setups.

Obviously in the second setup pattern coarsening is hindered. Even up to fluences of $\approx 14 \times 10^{21} \mathrm{ions\,m^{-2}}$ no coarsening is observed. The regularity found in the according self correlation images in the insets of figure 5.24(a) and (b) is similar and nearly independent of the fluence. This discovery may be explained by the fact that the present setup geometry avoids ion scattering and shadowing. The local angle of incident ions on the flat facet is $\theta_1 \approx 21^\circ$ to 22° and $\theta_2 \approx 33^\circ$ to 34° on the steep facet; therefore, the influence of reflected ions is negligible. The incoming direction of Fe with 30° is far away from grazing incidence i.e. it is close to normal incidence. Since the incoming Fe reaches both facets the local Fe flux on the flat facet is higher by only a factor of about 2 compared to the steep facet, the incoming Fe reaches both facets. As a consequence both the Hauffe coarsening mechanism and shadowing are avoided, leading to a high pattern regularity.

Conclusion

Our investigation of fluence dependent measurements with different co-evaporation geometries disclose that the pattern roughness and regularity may be tuned by the influx directions of the incoming ions and the co-evaporated Fe.

We emphasize that simultaneous metal co-deposition experiments and elimina-

tion of coarsening mechanisms strongly enhance pattern regularity which might be suitable in view of application. An outstanding pattern regularity was previously presented by the work of Ziberi et al. [136; 138; 142]. In fact their sputtering geometry is comparable to the setup geometry we used for the experiments presented in figure 5.24. In their experiments the incoming directions of ion and Fe directions are in close proximity [106].

5.7 Dependence on the Directionality of Incoming Kr^+ and Fe

Introduction

We presented in the previous section that shadowing is strongly connected to pattern coarsening, this chapter will go a step further and demonstrate, that shadowing plays in general a crucial role in the impurity assisted pattern formation process.

In a recent publication, Zhang et al. [35] claim that the saturation Fe coverage is decisive for the pattern selected in a co-sputter deposition situation (termed surfactant sputtering by them). The authors find that for 5 keV Xe^+ ion exposure and simultaneous Fe co-sputter deposition a saturation coverage is quickly reached and established for fluences of $F \approx 1 \times 10^{21}$ ions m^{-2}. Assuming that the saturation coverage grows monotonically with the flux ratio Φ_{Fe}/Φ_{ion}, this finding agrees with our observations derived from both, co-sputter deposition and co-evaporation. However, in the section at hand it will be shown that the flux ratio (or the saturation coverage) is only a good parameter for the description of pattern formation, as long as the other variables are fixed, specifically the directionality of the impinging Fe particles with respect to the ion beam.

In the following we direct our attention to the origin of the pattern phase transition between regions (I) and (II), i.e. the transition between a flat surface marginally patterned through irregular shallow depressions (holes) and a rippled surface with

a large roughness in excess of 10 nm and a corrugation in the order of 100 nm (see section 5.3). Disregarding for the moment the real space aspect of this transition, we note that it coincides with a transition from simultaneous exposure of Si(001) to direct and scattered energetic Kr atoms for $x \leq 1$ mm in region (I), to exposure only by direct Kr^+ in region (II). This transition is unambiguous from the erosion step between regions (I) and (II) as measured by optical interferometry [compare figure 5.6(a)]. Despite the additional bombardment by scattered Kr atoms, in region (I) plenty of Fe is present. The concentration $c_{Fe} \approx 0.1$ is much higher than for $x \approx 3$ mm, where a pronounced dot pattern is observed (compare figure 5.2). We are left with the conclusion that to understand this difference, we have to consider the directionality of the energetic particles with respect to the Fe flux rather than the concentration (or saturation coverage) of Fe. Specifically, we hypothesize that if a component of the energetic particles comes from a similar direction as the Fe flux, the tendency for pattern formation is strongly diminished.

Results

To test this hypothesis, we again conducted controlled co-evaporation experiments. In figure 5.26 we compare three co-evaporation experiments with a flux ratio Φ_{Fe}/Φ_{Kr^+} = 4% – 5%, which differ only in the incidence angles of the 2 keV Kr^+ and of the Fe as sketched in (a)–(c). Figure 5.26(d) is identical to figure 5.20(b) where ion beam and Fe flux enclose an angle $\alpha = 105°$ and a faceted ripple pattern forms. The situation mimics the sputter co-deposition within region (II). If we keep the direction of incidence of the Fe flux fixed and move the ion beam close to it, such that $\alpha = 30°$, no pattern forms as displayed in the STM image of figure 5.26(e). This situation corresponds to the co-sputter deposition in region (I), but without the direct Kr^+ flux. Alternatively, if the ion beam is kept in its position but the Fe flux is moved close to it, so that $\alpha = 30°$ again no ion beam pattern forms as shown in figure 5.26(f). It appears that the angle α between ion beam and Fe flux is a decisive quantity in pattern formation and that a large α fosters pattern formation.

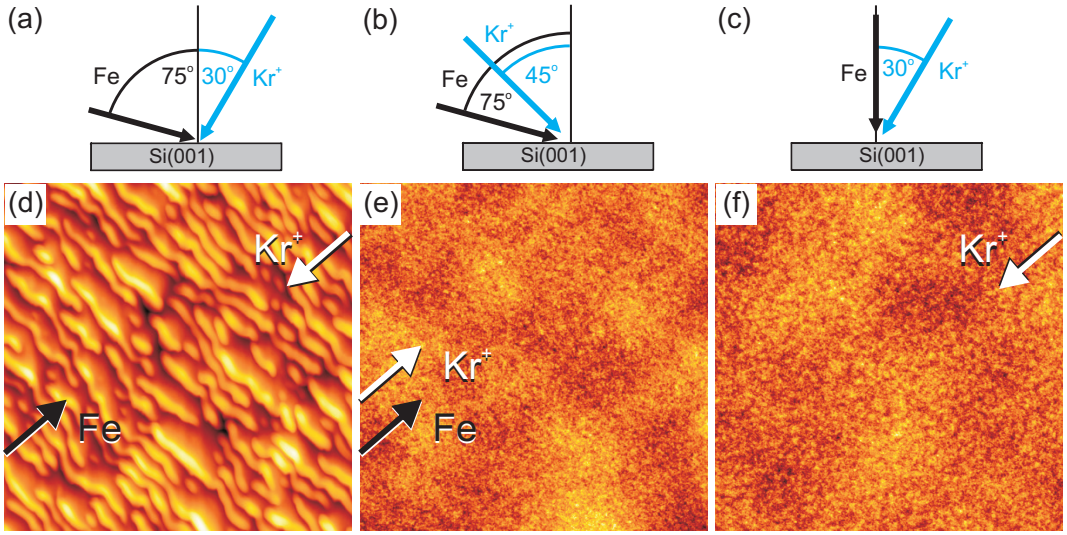

Figure 5.26: (a) Dependence of pattern formation on the directions of deposition flux and ion beam. (a)–(c) Sketches of deposition geometry indicating the angles of deposition flux and ion beam with respect to the surface normal. (d)–(f) STM images after co-evaporation during a fluence of $F \approx 6\times10^{21}$ ions m^{-2} of 2 keV Kr^+ at 300 K. Atom-to-ion flux ratios are (d) $\Phi_{Fe}/\Phi_{Kr^+} = 4\%$, (e) $\Phi_{Fe}/\Phi_{Kr^+} = 5\%$ and (f) $\Phi_{Fe}/\Phi_{Kr^+} = 4\%$. Height differences Δz spanned by the image contrast are (d) 56 nm and (e),(f) 2 nm. Images size is always 1 µm × 1 µm.

Discussion

Zhang et al. [35] state in their work on sputter co-deposition of Fe on Si(001): "Therefore the initial steps of pattern formation are caused by none of the following: directional effects of the Fe-deposition, directional effects of the ion beam, and [...]". While it would be a non-trivial task to demonstrate that pattern formation is determined solely by the directionality of the impinging particle fluxes, from our experiments it is obvious that the directional effects of Fe-deposition and ion beam are a decisive factor for pattern formation also in the initial stages of pattern formation. It turns out that co-evaporation experiments with unique and variable directions of the particle fluxes are a key to a deeper understanding of impurity induced pattern formation.

Our finding that the angle α between ion beam and impurity flux is relevant and should be large for efficient pattern formation is consistent with the observation of dot formation at normal incidence ion erosion. If the impurities are largely supplied from the sample mount, α may be close to 90°. Similar, for grazing incidence ion bombardment impurities supplied to a given location may be supplied from the ion beam illuminated parts of the sample mount, thereby resulting in α well above 90°.

Our observations also do not necessarily rule out pattern formation if the ion beam and co-deposition flux come from similar directions (i.e. α is small). If the flux ratio $\Phi_{\text{impurity}}/\Phi_{\text{ion}}$ is high enough or the ion fluence is large enough also a pattern will arise (see sections 5.6 and 5.9). But our observations indicate that using a large angle α is much more efficient for co-deposition induced pattern formation and allows one to minimize flux ratio and ion fluence. This finding may be of relevance in view of the application of co-sputter deposition for patterning with the goal of large corrugations, as achieved in the present study with only moderate ion fluences. It also implies that morphologies resulting from ion beam experiments are more tolerant with respect to impurities originating from the ion source itself than to impurities sputtered from the sample environment. In several of the previous ion beam patterning experiments of Si, unintentional impurities originated from the ion source or were deposited with a small angle α, e.g. results by Gago et al. [131] and Ziberi et al. [139]. This might explain why even with large ion fluences only shallow ripple patterns with corrugations in the nanometer range resulted. The patterns fabricated in the present study display corrugations beyond 100 nm for very moderate ion fluences. This observation and its explanation may point a way to efficient production of highly corrugated patterns.

Finally, we note that the absence of shallow holes in Figs. 5.20(b) and (c) seems to indicate that an influx of energetic particles from different orientations is necessary for hole formation, as in region (I) during sputter co-deposition.

Conclusions

Variation of the angle between ion beam and impurity source has a significant effect on pattern formation. For $\alpha > 90°$ we observe rapid formation of a faceted and rough pattern while for small angles $\alpha \approx 30°$ pattern formation diminishes. The larger this angle, the more efficient is pattern formation. We conclude that shadowing is of decisive importance for the formation of local impurity concentration inhomogeneities.

5.8 Co-deposition Directionality and Ion Beam Patterning: A Stability Analysis

Introduction

In the previous section 5.7 it was shown that shadowing and local flux variations of the incoming impurities foster the pattern formation mechanism. In the present chapter we present a surface stability analysis depending on local impurity flux variations invoked by varying the angle α between the incoming direction of the ion beam and impurity source.

Results

Our EELS analysis of a ripple pattern presented in figure 5.3 identified that the sputter co-deposited material forms a chemical pattern in phase with the topographic pattern. Iron silicides have substantial negative enthalpies of formation in the range of -20 kJ/mol to -30 kJ/mol with a maximum of 32.5 J/mol for FeSi [144]. We therefore assume that although no long range order exists, depending on the Fe concentrations the local atomic arrangements are close to the ones of the corresponding iron silicides. This assumption is consistent with the findings of Sánchez-García et al., who conclude on the basis of a chemical shift in XPS that upon Fe co-sputter

deposition on Si iron silicide forms [129]. Using TRIM.SP and the structure data compiled by Moroni et al. [175], we calculated for 2 keV Kr^+ incident with $\vartheta = 30°$ the erosion rate for the different iron silicides and the pure elements. As surface binding energy for the different compounds in TRIM.SP we used the cohesive energies calculated in the generalized gradient approximation of density functional theory by Moroni et al. [175]. As compiled in table 5.1, the erosion rate is minimal for FeSi and is lower for all silicides than is the case for elemental Si. Assuming a steady state situation, the sputtered Fe is replenished through co-deposition. The partial Si yield is in all cases lowered through the Fe co-deposition. Our inferences do not depend critically on the local angle of incidence. Similar differences in sputtering yield and erosion rate are present in a broad angular range between $0° \leq \vartheta \leq 60°$. Therefore, a height modulation with iron silicide accumulation close to the elevations of the pattern will be amplified by composition dependence of the erosion rate. Our detailed analysis agrees in this respect with the one of Zhang et al. [35].

Table 5.1: Partial silicon sputter yield Y_{Si}, total sputter yield Y, density ρ and erosion rate Y/ρ as a function of sample composition.

composition	Y_{Si} (Si atoms/ion)	Y (atoms/ion)	ρ (atoms/nm^3)	Y/ρ (nm^3/ion)
Fe	0	3.54	84.8	0.042
Fe_3Si	0.75	2.77	88.8	0.031
FeSi	1.28	2.40	89.0	0.027
$FeSi_2$	1.56	2.23	79.8	0.028
Si	1.77	1.77	50.0	0.035

Discussion

According to the picture developed by Zhang et al. [35], phase separation initiates pattern formation. Phase separation enabled by ion induced mobility is assumed to create a chemically modulated surface which is transformed into a height pattern by a composition dependent sputter yield. Only then, if a coupled pattern of composition and height is established, directed deposition of Fe enhances the pattern contrast or pattern corrugation. This plausible picture is in agreement with our

considerations on the composition dependent erosion rate and with numerous observations of ion induced phase separation. As an example, radio frequency sputter deposition of silicides on silicon substrates results in well ordered and aligned rod patterns [101].

However, this picture is hard to reconcile with three of our observations. (i) In region (I) for $x \leq 1\,\mathrm{mm}$ the Fe concentration is 0.08–0.09 and only a faint irregular pattern with a marginal roughness $\sigma \leq 0.35\,\mathrm{nm}$ develops [compare figures 5.1(a) and 5.2]. In contrast in region (II) at $x = 3\,\mathrm{mm}$ the Fe concentration is only 0.01-0.02, but a pronounced dot pattern with $\sigma \approx 1\,\mathrm{nm}$ is present. If phase separation would be decisive, one would expect that the additional mobility supplied by the scattered Kr atoms and the much higher Fe influx and steady state concentration in region (I) leads to a much faster phase separation than at $x = 3\,\mathrm{mm}$ in region (II). Consequently one would expect a well developed and well-ordered pattern in region (I) and a pattern of inferior quality for the area at $x = 3\,\mathrm{mm}$, contrary to observation. (ii) The phase boundary between region (I) and (II) visualized in figures 5.10–5.12 is abrupt and inhomogeneous, showing pill bugs in flat areas. It is not obvious how an initial phase separation could be reconciled with such an heterogeneous pattern landscape composed of large flat areas with localized pattern patches. (iii) For identical deposited amounts of Fe and identical ion beam exposure conditions patterns arise or not, only depending on the angle between ion beam and deposition flux [compare figures 5.26(a) and (c)]. One can not understand how the direction of the impinging Fe on an initially flat surface could decide on the occurrence of a phase separation as such.

Therefore, we propose a scenario for pattern evolution which involves also height fluctuations as a necessary ingredient for pattern formation. Analogous to a linear stability analysis, we assume an existent sinusoidal surface profile resulting from a height fluctuation as sketched in figure 5.27. For pure Si, the profile amplitude will decrease in time until it vanishes. This holds as long as $\vartheta \leq 55°$ (see section 4.2) and thus specifically in our case with $\vartheta = 30°$. If the ion flux and the Fe deposition flux

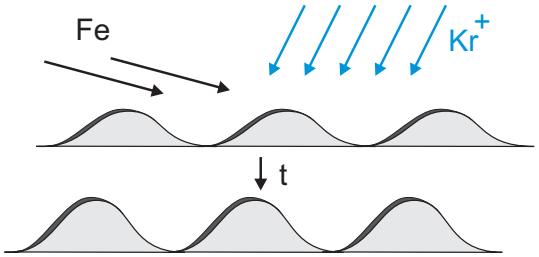

Figure 5.27: Sketch of co-deposition with a large angle between Kr^+ ion beam and Fe deposition flux for a sinusoidal surface profile. In this situation, the highest Fe flux arrives in profile locations, where the erosion flux is minimal. Consequently, the surface profile destabilizes with time t (see text).

come from the same direction, locations which receive the highest Fe flux receive also the highest ion flux, a fact that tends to diminish build-up of concentration variations. However, if (as indicated) the ion flux and the Fe flux enclose a large angle α, locations that receive the highest Fe flux receive the lowest ion flux. Thereby not only concentration differences, but also erosion rate differences build-up and the pattern is amplified. Whether this simple view captures all essentials of co-deposition induced pattern formation on Si(001) might be tested by energetic Fe^+ ion bombardment. Exposure of Si(001) to Fe^+ with sufficient energy to cause net erosion, i.e. with energies of a few keV, and for not too large angles ϑ, should not cause pattern formation.

Conclusions

We note that in agreement with the analysis of Zhang et al. [35] our observations and the derived pattern formation scenario provides no trace of indication for the relevance of curvature dependent sputtering and a stress induced instability as proposed by Zhou and Lu [95]. We find a height fluctuation to induce a modulation of the chemical composition which in turn amplifies the amplitude of the height fluctuation and thereby initiates pattern formation. Silicide formation itself is a relevant feature of this pattern formation scenario. Its relevance is implicit in table 5.1. The

negative enthalpy of formation of the silicides results in an enhanced cohesive energy and thus an enlarged surface barrier for sputtering, which tends to diminish the Si yield Y_{Si}. Also, in comparison to pure Si, the silicides have a much higher density which guaranties their reduced erosion rate.

5.9 Directionality and Flux Ratio Dependence: A Pattern Phase Diagram

Introduction

The following results are an extension of our co-evaporation experiments presented in the previous section 5.8. It was demonstrated that local impurity influx variations and shadowing play a crucial role for a self-amplifying pattern growth mechanism and a large relative angle between ion source and impurity source α fosters pattern formation. The experiments presented before were limited to Φ_{Fe}/Φ_{Kr^+} flux ratios less than 5%. The intention here is to go even further and raise the Φ_{Fe}/Φ_{Kr^+} flux ratio to get an insight if pattern formation is possible at all for certain sputter co-evaporation geometries.

Results

Figure 5.28 shows a pattern phase diagram depending on the co-evaporation geometry and the flux ratio. The energy of incoming Kr^+ is always 2 keV. The setup geometry for each row of STM images is sketched in the first column. Within the presented overview of STM images the Φ_{Fe}/Φ_{Kr^+} flux ratio increases from left to right and is noted in the lower left corner of each STM image. In order to improve data comparison the image corrugation Δz of all images is set to 15 nm[1]. The image size is always 1 µm × 1 µm. Furthermore, the insets show the resulting surface in detail with an image size of 200 nm × 200 nm and with optimized contrast.

[1]Please note that for figure 5.28(t) the image corrugation of $\Delta z = 15$ nm is far too small. The optimum image corrugation is in fact 56 nm as displayed before in figure 5.20(b).

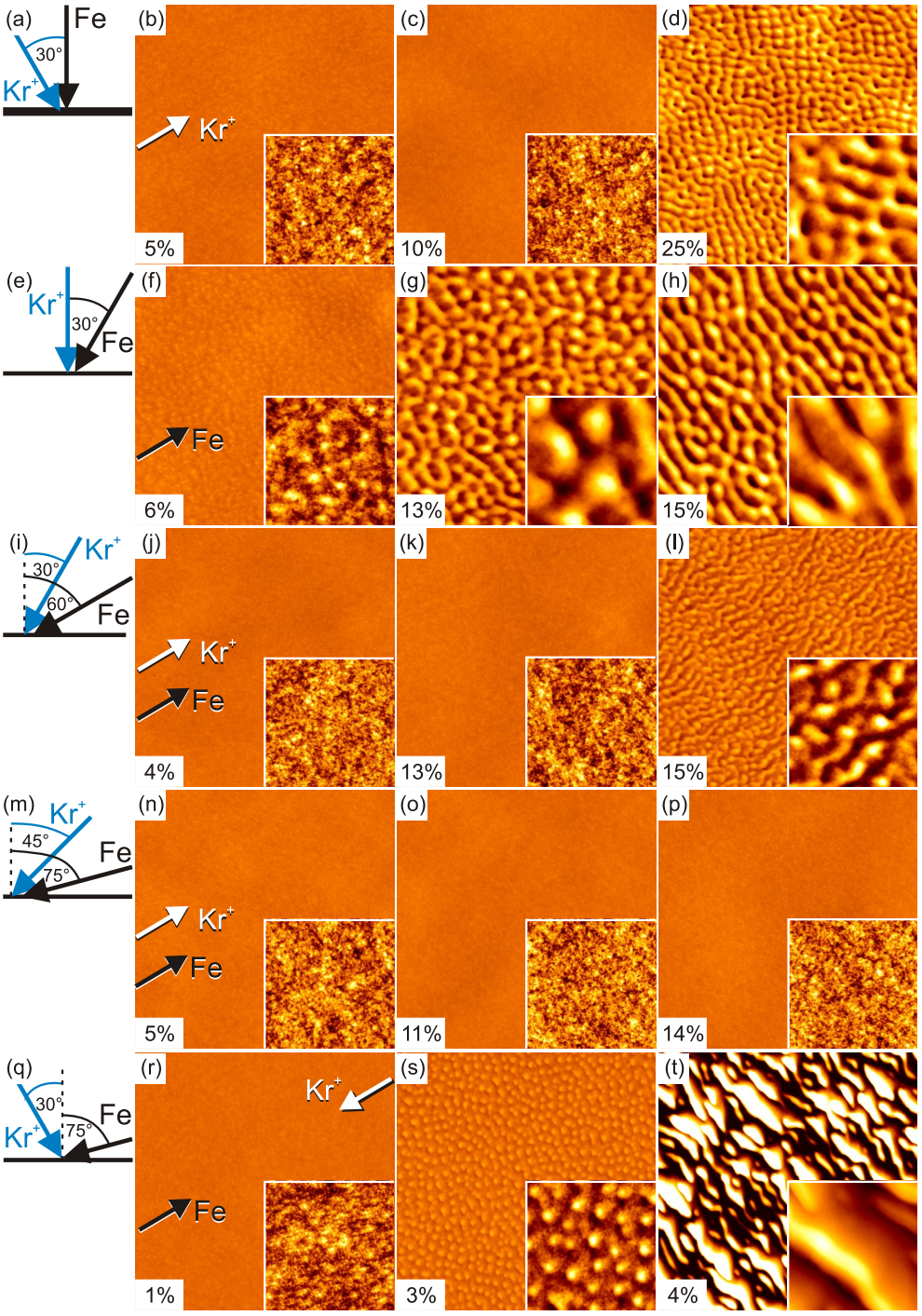

Figure 5.28: STM images of Si(001) after a 2 keV Kr^+ fluence of $F \approx 6 \times 10^{21}$ ions m^{-2} and additional co-evaporation of Fe. Image size and image corrugation are always 1 µm × 1 µm and $\Delta z =$ 15 nm, respectively. The insets show a detail of 200 nm × 200 nm with optimized contrast. The first column shows the setup geometry with the influx directions of Kr^+ and Fe for each row. The white and black arrow in the STM images of the second column indicate the incoming direction of Kr^+ and Fe, respectively. The Φ_{Fe}/Φ_{Kr^+} flux ratio is displayed in the lower left corner of each STM image.

As sketched in figure 5.28(a) the experiments presented in figures 5.28(b)–(d) show according STM images resulting from measurements with the Fe impurity flux incoming normal to the surface i.e. without a preferential direction while the Kr^+ comes in with $\vartheta = 30°$. Up to a flux ratio of $\Phi_{Fe}/\Phi_{Kr^+} \leq 10\%$ no pattern develops and the surface remains smooth with $\sigma \approx 0.2\,nm$. Raising the Fe flux so that $\Phi_{Fe}/\Phi_{Kr^+} \approx 25\%$ a waved surface develops with partially square ordered elevations or even dots and a roughness $\sigma \approx 2.0\,nm$. The characteristic pattern wavelength measured horizontally is about $\Lambda \approx 46\,nm \pm 20\,nm$ and vertically $\Lambda \approx 40\,nm \pm 20\,nm$.

Figure 5.28(e) sketches the sputter co-evaporation geometry for the second row of STM images presented in figures 5.28(f)–(h). In this case the incidence angle of Kr^+ is normal to the surface and thus without a preferential direction while the Fe influx is oriented 30° off-normal. Already at a low Φ_{Fe}/Φ_{Kr^+} flux ratio of $\approx 6\%$ a shallow dot pattern appears [figure 5.28(f)], yet the surface is still rather smooth with $\sigma \approx 0.3\,nm$. Figure 5.28(g) shows a patterned surface generated with a flux ratio of $\Phi_{Fe}/\Phi_{Kr^+} \approx 13\%$ with roughness $\sigma \approx 2.1\,nm$. Mainly dots are visible with some short ripple ridges in between. Figure 5.28(h) displays a ripple pattern with a roughness of $\sigma \approx 2.8\,nm$ and rather short ripple segments with a characteristic pattern wavelength $\Lambda \approx 35\,nm$ resulting by the use of a flux ratio of $\Phi_{Fe}/\Phi_{Kr^+} \approx 15\%$.

The third row displays measurements performed with Kr^+ incoming from $\vartheta = 30°$ and Fe incoming from 60° to the normal [figure 5.28(i)]. Thereby the influx of both Kr^+ and Fe is from the same side. Up to a Φ_{Fe}/Φ_{Kr^+} of $\approx 13\%$ the surface remains smooth with $\sigma \approx 0.2\,nm$ [figures 5.28(j)–(k)]. At a flux ratio of $\Phi_{Fe}/\Phi_{Kr^+} \approx 15\%$ a patterned surface with a roughness of $\sigma \approx 1.0\,nm$ is present. The pattern is not well ordered and might be comparable to wriggled ripples with wave vector $\vec{k}$ oriented rather perpendicular to the influx of Kr^+ and Fe. The characteristic spacing between the wriggled ripples is about $\Lambda \approx 44\,nm \pm 18\,nm$.

Figure 5.28(m) sketches a sputtering geometry with Kr^+ incoming from $\vartheta = 45°$

and the co-evaporated Fe from 75° to the normal again both incoming from the same side. Tilting the influx of Kr^+ and Fe away from the normal up to a Φ_{Fe}/Φ_{Kr^+} flux ratio of 14% no pattern develops [figures 5.28(n)–(p)] and the surface remains smooth with $\sigma \approx 0.2\,nm$.

The last row represents a co-evaporation experiment with the Kr^+ and Fe flux incoming opposite to each other. Kr^+ is impinging from $\vartheta = 30°$ to the normal and the Fe influx is grazing with 75° [figure 5.28(q)]. The measurements presented in figures 5.28(r)–(t) were illustrated already before in figures 5.20(b)–(d); thereby each image was presented with optimized contrast. While at a flux ratio of $\Phi_{Fe}/\phi_{Kr^+} = 1\%$ the surface remains smooth with $\sigma \approx 0.2\,nm$ [figure 5.28(r)], at $\Phi_{Fe}/\Phi_{Kr^+} \approx 3\%$ a nanodot pattern with roughness $\sigma \approx 0.6\,nm$ and a characteristic pattern wavelength $\Lambda \approx 42\,nm \pm 15\,nm$ is visible. Figure 5.28(t) shows a rough ripple pattern with $\sigma \approx 8.7\,nm$ exceeding clearly the fixed image corrugation Δz. The ripple patter wavelength is $\Lambda \approx 51\,nm$. It is worth mentioning that exceptionally the Φ_{Fe}/Φ_{Kr^+} flux ratio within this sequence does not exceed 4%.

Discussion

Obviously, if the Fe is incoming normal to the substrate surface, pattern formation is suppressed [figures 5.28(b)–(d)]. In this case a high Φ_{Fe}/Φ_{Kr^+} flux ratio between 10% and 25% is necessary to initiate the pattern formation process. Interestingly, figure 5.28(d) presents in the main a twofold symmetry and a characteristic pattern wavelength. The pattern orientation seems not to be strictly related to the incoming direction of the Kr^+ beam. As we expect an amorphized surface, the crystal orientation of the substrate should not play a role. Thus we cannot make any substantiated statements so far about the origin of the aforementioned pattern symmetry and orientation.

The Fe influx has no preferential direction related to the surface and as a consequence shadowing effects are prevented. As by Kr^+ erosion of Si(001) with $\vartheta = 30°$ without co-deposition of impurities no patterns form, the near normal incident Kr^+

beam rather smoothes the surface than provokes variations in height. That a pattern evolves under these conditions at all as found in figure 5.28(d) indicates that other mechanisms than shadowing have to be considered. Pattern formation on compound targets was frequently explained by segregation evoked by preferential sputtering and differing surface diffusion constants of the alloy species [94; 96]. Moreover, phase separation which might be intensified by the energy transfer of the ions to the compound target was considered as decisive mechanism [34; 35].

The situation is different when the incoming directions of Kr^+ and Fe are swapped. When Kr^+ is incoming normal to the surface i.e. the influx of ions has no preferential direction related to the surface and the Fe is incoming from an angle of 30° to the normal, the formation of patterns is more efficient. At a Φ_{Fe}/Φ_{Kr^+} flux ratio of $\approx$ 6% a shallow dot pattern forms. Dot patterns, yet more pronounced, were observed by various research groups by the use of normal incident ions [29; 95; 105; 130–132; 137]. This context will be elucidated by comparison of experiments presented in figures 5.28(f) and (s) both showing a nanodot pattern. As sketched in figures 5.28(e) and (q) the main difference may be found in the varying impurity flux from near normal to grazing incidence. The incoming Kr^+ with normal or near normal incidence should not be qualitatively different under pure conditions; in both cases the ion beam smoothes the surface (see figure 4.2).

We showed in section 5.7 that a large angle α between incoming ions and impurities promotes pattern formation. Therefore, it is plausible that the nanodots in figure 5.28(s) are even more pronounced than the dot pattern in figure 5.28(f), although the respective Φ_{Fe}/Φ_{Kr^+} flux ratio is halved.

Once more these findings lead us to the following conclusion regarding experiments influenced by unintentional co-deposition: As local impurity flux variations play an important role we assume that impurities originating from the ion source do not influence the pattern formation that much. Co-sputtered material incoming with grazing incidence e.g. from the sample surroundings triggers much more pattern formation.

Furthermore, the whole sequence of figures 5.28(g) and (h) may be compared with the sequence figures 5.28(s) and (t). Obviously, with an increasing Φ_{Fe}/Φ_{Kr^+} flux ratio both co-evaporation geometries lead from a flat surface over a nanodot pattern to a ripple pattern. The major difference is that with the geometry shown in figure 5.28(e) a higher Φ_{Fe}/Φ_{Kr^+} flux ratio is necessary compared to the geometry in figure 5.28(q). On the other hand the ripple pattern in figure 5.28(h) is more homogeneous in height and more regular than in figure 5.28(t) as shadowing and coarsening mechanisms are prevented (see section 5.6).

For figures 5.28(j)–(k) Kr^+ is incoming with $\vartheta = 30°$ and Fe with 60° to the normal. Nevertheless Fe is incoming nearly grazing, pattern formation sets in only between high Φ_{Fe}/Φ_{Kr^+} flux ratios of 13% – 15%. This might be explained as follows: both the impurity and the Kr^+ flux come in from the same side. We suggest that the pattern formation process is inhibited by the directed Kr^+ beam. As the grazing incident local Fe flux increases at a preceded height fluctuation, it is the same with the local Kr^+ flux. Hence the increased sputtering prevents an accumulation of Fe and thus a self-amplifying effect is suppressed.

For the co-evaporation geometry displayed in figure 5.28(m) up to a Φ_{Fe}/Φ_{Kr^+} flux ratio of 14% no patterns form [figures 5.28(n)–(p)]. Even though the Φ_{Fe}/Φ_{Kr^+} flux ratio in figures 5.28(h), (l), and (p) is almost the same, the roughness varies considerably. Remarkably the setups presented in figures 5.28(i) and (m) are almost identical. Nevertheless in the latter case the pattern formation process seems to be even more suppressed. This may be explained by the higher sputtering yield for an ion beam incident angle of $\vartheta = 45°$ related to $\vartheta = 30°$ by 62%. Hence deposited Fe is eroded more efficiently and Fe accumulation is strongly inhibited.

Conclusions

It is apparent that the roughening potency and pattern regularity depend on the interplay of the incoming directions of the ion beam and impurity influx and their flux ratio. Once the smoothing, roughening and coarsening mechanisms governing

the pattern formation process are understood the pattern roughness and regularity may be systematically tuned.

6 Summary

Ion beam pattern formation is an efficient and versatile technique for creating regular nanoscale surface patterns over large, wafer-size areas.

The first part of the present thesis deals with pattern formation on Si(001) through 2 keV Kr^+ ion beam erosion under pure conditions investigated by *in situ* scanning tunneling microscopy and low energy electron diffraction. Careful ion beam pattern formation experiments performed in ultra high vacuum show that under a wide range of conditions no patterns are formed at all on silicon wafers. At room temperature and for fluences up to $F \approx 1 \times 10^{22}\,\mathrm{ions\,m^{-2}}$ no patterns develop for ion incidence angles $\vartheta \leq 55°$ with respect to the global surface normal. Quite the contrary, a near normal incident ion beam in fact smoothes an initial rough Si surface.

Only for grazing incidence angles $60° \leq \vartheta < 81°$ pronounced ripple and tiled roof patterns develop. The angular range in which the Si surface becomes unstable due to ion beam erosion is located around the maximum of the angle dependent sputtering yield curve $Y(\theta)$. The highest resulting surface roughness is found at $\vartheta = 75°$ just at the maximum of the angle dependent sputtering yield curve $Y(\theta)$. Moreover, the most regular ripple patterns for 2 keV Kr^+ bombardment and a fluence of $F \approx 1 \times 10^{22}\,\mathrm{ions\,m^{-2}}$ are generated at an incidence angle of $\vartheta = 63°$. Completive, we showed that ion beam induced amorphous ripple patterns may be transformed to crystalline ones by subsequent sample annealing.

Analyses of sawtooth profiled ripple facets generated at various oblique incident angles of the ion beam disclose that for sufficient fluences both ripple facets form a stable slope with respect to the global surface plane independent of the incoming direction of the ion beam. These findings disagree with the frequently applied theory of gradient dependent surface topography development [76; 77] which predicts stable

ripple facet angles related to the incoming ion beam.

Analysis of the fluence dependence of pattern formation was conducted in the unstable range of $\vartheta = 75°$. The flat surface evolves via a small amplitude, regular ripple pattern and transforms via a coarsening mechanism to a large amplitude, irregular faceted pattern. The small amplitude ripple patterns with a distinct wavelength of 33 nm may be explained by the lately proposed theory of *solid flow*. Thereby ion induced defects such as vacancies and interstitial atoms enhance the viscosity of the amorphous surface layer. As a consequence, the ion beam induced stress is released by a redistribution of material resulting in an undulated surface.

The high amplitude ripple patterns generated at high fluence exceed the regime of linear continuum models. An adequate nonlinear theory which describes the observed specified facet orientation is still non-existent.

In the second part of the thesis we present experiments on sputter co-deposition and co-evaporation of Fe during 2 keV Kr^+ erosion of Si(001). Investigations via scanning tunneling microscopy, atomic force microscopy and scanning electron microscopy reveal that co-deposition of stainless steel during ion beam erosion results in well developed hole, dot and ripple patterns for ion fluences of $F \approx 5 \times 10^{22}\,\mathrm{ions\,m^{-2}}$. The ripple wave vector of the ripple patterns is found to be aligned parallel to the direction of the impinging steel atoms. The observed patterns form at angles ϑ, where no patterns result for clean ion erosion of Si.

Additional chemical analysis of the surface realized by secondary ion mass spectrometry identifies the co-deposited impurities to be mandatory for pattern formation in the near normal ion beam incident angular range. The formation of dot and ripple patterns is distinguished by the concentration of co-sputtered material. Dots contain much less co-sputtered Fe than ripples.

Our results show unequivocally that the variety of patterns on Si observed in different laboratories for ion incident angles $\vartheta \leq 55°$ are a result of unintentional co-deposition of metal originating from the ion source or the sample surroundings.

A surface topography analysis by phase-shifting interferometry in combination with kinetic Monte Carlo calculations evaluating the spatial distributions of sputtered Fe and reflected Kr at the steel plate as well as the according particles' energies lead to the following conclusions: Nanohole patterns are observed under the influence of co-sputtered steel and strong additional sputtering by ions reflected from the steel plate. Ripple and dot patterns are formed in a distance range in which reflected ions are largely absent.

Furthermore, we observed a pattern bifurcation at the abrupt transition from flat nanohole to rough ripple patterns. Rough rippled objects, termed *pill bugs* by us due to their characteristic shape, grow out of the flat surface which is covered with nanoholes. In this range the flux of scattered Kr atoms ceases and the coexistence of fundamentally different patterns side by side indicates that there are conditions where pattern formation does not proceed from a linear to a nonlinear regime. From their characteristic shape we were able to conceive a growth mechanism for the *pill bugs* which is governed by a rapid self-accelerated growth process that may be described in terms of pattern nucleation and lateral self-amplifying pattern growth.

We introduced the well defined experimental setup of ion erosion with simultaneous Fe co-evaporation to rule out and to identify mechanisms relevant for pattern formation on Si(001) with impurities. This experimental setup allows full control of the incoming $\Phi_{\mathrm{Fe}}/\Phi_{\mathrm{Kr}^+}$ flux ratio, and the incoming directions of Kr^+ and Fe.

The key factor selecting the type of pattern is the ion-to-impurity arrival ratio. A higher influx of Fe leads to an increased destabilization of the surface. Moreover, variation of the angle between ion beam and impurity source has a significant effect on pattern formation. The larger this angle, the more efficient pattern formation. This observation highlights the relevance of local flux variations which are of decisive importance for the formation of local impurity concentration inhomogeneities.

Fluence dependent co-evaporation measurements performed with large and small angles between ion beam and impurity source disclose that the roughening potency and the pattern regularity may be tuned by enabling or avoiding pattern coarsening

mechanisms, respectively.

Transmission electron microscopy measurements combined with electron energy loss spectroscopy of a ripple pattern generated by sputter co-deposition reveal the chemical modulation of the pattern to be in phase with the height modulation. This leads to the assumption that silicide formation is relevant for pattern formation as it affects the sputtering yields.

In conclusion, pattern formation is assumed to be initiated by height fluctuations, which themselves lead to local impurity flux variations inducing the observed modulation of the chemical composition. The resulting local sputtering yield variations in turn amplify the destabilization of the surface.

Temperature dependent measurements in the range from 140 K to 440 K where the Si surface is amorphous during erosion disclose that thermally activated processes are largely irrelevant. However, the best pattern homogeneity was realized at low temperatures. Dramatic changes take place above a threshold temperature of about 600 K. For these high temperatures pillars and spongelike patterns evolve, with amplitudes in the order of 100 nm and directed towards the ion beam. Grazing incidence X-ray diffraction and transmission electron microscopy reveal the structures to be composed of crystalline iron silicide. The high aspect ratio of the patterns indicates that additionally to sputtering a growth effect must be involved.

7 Outlook

As the phenomenon of ion beam pattern formation on Si(001) is a vivid field of research the presented results already stimulated ongoing experimental and theoretical work on this topic.

It is apparent that the experiments described in this thesis are limited. Certain parameters e.g. the substrate material, ion species and ion energy were not changed. Nevertheless, these parameters may also influence the pattern formation mechanism. Our ion beam incident angle dependent measurements under clean conditions disclosed that the inclination angle of the facet angles of a sawtooth profiled pattern is stable. In analogy for sand dunes it was found that their steepness increases with stronger wind and fineness of the sediment [153; 154]. Hence in our context we assume that accordingly the substrate viscosity and ion energy might be decisive parameters [41; 176]. To prove this hypothesis it would be interesting to study the dependence of the ion energy on the facet inclination angle at high ion fluences at which the facet orientation remains stable. Furthermore, the viscosity may be tuned by varying the silicon substrate temperature or changing the substrate material to e.g. germanium.

The surface dynamics during sputtering on amorphous and crystalline surfaces are driven by differing principles [70]. To test the influence of crystallinity, it would be interesting to perform clean angle and fluence dependent ion beam erosion experiments at temperatures where the Si surface remains crystalline during erosion.

To get a deeper insight into the ion beam pattern formation mechanism it would be interesting to investigate the damage induced by single ion impacts on a crystalline Si(001) surface by scanning tunneling microscopy. Likewise Kyuno et al. [177] investigated the damage induced by 4.5 keV He^+ on Si(001) under normal incidence. Their study could be extended by the use of heavier ion species and varying the ion

incidence angle. The results would establish a connection to molecular dynamics simulations and could prove the theory derived by Norris et al. which links the ion impact crater function to large scale ion beam pattern formation [83; 84].

We presented that simultaneous deposition of a second chemical species affects the pattern formation mechanism considerably. Therefore, our results also point to the need for well controlled erosion experiments and chemical analysis of the eroded surfaces to rule out impurity effects.

We suggested that iron-silicide formation changes the density and thus the local erosion velocity of the substrate. To confirm our argumentation, it would be insightful to co-deposit other materials and thus to investigate independently the influence of silicide formation, change in density or preferential sputtering on the pattern formation mechanism.

The angle between ion source and impurity source was found to be decisive to induce local flux variations. Sputtering with Fe^+ would set this angle to zero and it would be interesting if – under these conditions – it is possible to generate patterns on Si in the near normal incident range at all.

Otherwise, maximizing the angle between ion source and impurity source so that both ions and impurities are incoming grazing from opposite directions should amplify the pattern formation mechanism at most. Therefore, a fluence dependent study with the mentioned setup geometry would be instructional.

It remains to be investigated whether co-sputter deposition must be considered also for pattern formation of other materials or other energy ranges outside the keV region as a hidden parameter.

References

[1] S. J. Wilson and M. C. Hutley. Optica Acta **29**, 993 (1982). *The Optical Properties of 'Moth Eye' Antireflection Surfaces.* doi:10.1080/713820946. 1

[2] D. Flamm, F. Frost, and D. Hirsch. Appl. Surf. Sci. **179**, 95 (2001). *Evolution of surface topography of fused silica by ion beam sputtering.* doi:10.1016/S0169-4332(01)00269-0.

[3] H. Fouckhardt, I. Steingoetter, M. Brinkmann, M. Hagemann, H. Zarschizky, and L. Zschiedrich. Advances in OptoElectronics **2007**, Article ID 27316 (2007). *nm- and µm-Scale Surface Roughness on Glass with Specific Optical Scattering Characteristics on Demand.* doi:10.1155/2007/27316. 1

[4] C. H. Sun, P. Jiang, and B. Jiang. Appl. Phys. Lett. **92**, 061112 (2008). *Broadband moth-eye antireflection coatings on silicon.* doi:10.1063/1.2870080. 1, 105

[5] S. A. Boden and D. M. Bagnall. Appl. Phys. Lett. **93**, 133108 (2008). *Tunable reflection minima of nanostructured antireflective surfaces.* doi:10.1063/1.2993231.

[6] S.-H. Hong, B.-J. Bae, K.-S. Han, E.-J. Hong, H. Lee, and K.-W. Choi. Electron. Mater. Lett. **5**, 39 (2009). *Imprinted Moth-Eye Antireflection Patterns on Glass Substrate.* doi:10.3365/eml.2009.03.039. 1, 105

[7] P. Chaudhari, J. Lacey, J. Doyle, E. Galligan, S. C. A. Lien, A. Callegari, G. Hougham, P. S. A. N. D. Lang, R. John, K. H. Yang, M. H. Lu, C. Cai, J. Speidell, S. Purushothaman, J. Ritsko, M. Samant, J. Stohr, Y. Nakagawa, Y. Katoh, Y. Saitoh, K. Sakai, H. Satoh, S. Odahara, H. Nakano, J. Nakagaki, and Y. Shiota. Nature **411**, 56 (2001). *Atomic-beam alignment of inorganic materials for liquid-crystal displays.* doi:10.1038/35075021. 1

[8] A. H. Mayne, S. C. Bayliss, P. Barr, M. Tobin, and L. D. Buckberry. Phys. Status Solidi A **182**, 505 (2000). *Biologically Interfaced Porous Silicon Devices.* doi:10.1002/1521-396X(200011)182:1<505::AID-PSSA505>3.0.CO;2-#. 1

[9] L. T. Canham. Adv. Mater. **7**, 1033 (1995). *Bioactive Silicon Structure Fabrication Through Nanoetching Techniques*. doi:10.1002/adma.19950071215. 1

[10] V. S.-Y. Lin, K. Motesharei, K.-P. S. Dancil, M. J. Sailor, and M. R. Ghadiri. Science **278**, 840 (1997). *A Porous Silicon-Based Optical Interferometric Biosensor*. doi:10.1126/science.278.5339.840. 1

[11] Ü. Sökmen, A. Stranz, S. Fündling, S. Merzsch, R. Neumann, H.-H. Wehmann, E. Peiner, and A. Waag. Microsyst. Technol. **16**, 863 (2010). *Shallow and deep dry etching of silicon using ICP cryogenic reactive ion etching process*. doi:10.1007/s00542-010-1035-7. 1

[12] A. Wellner, R. E. Palmer, J. G. Zheng, C. J. Kiely, and K. W. Kolasinski. J. Appl. Phys. **91**, 3294 (2002). *Mechanisms of visible photoluminescence from nanoscale silicon cones*. doi:10.1063/1.1448394. 1, 105

[13] A. G. Nassiopoulos, S. Grigoropoulos, E. Gogolides, and D. Papadimitriou. Appl. Phys. Lett. **66**, 1114 (1995). *Visible luminescence from one- and two-dimensional silicon structures produced by conventional lithographic and reactive ion etching techniques*. doi:10.1063/1.113830. 1, 105

[14] P. D. Kichambare, F. G. Tarntair, L. C. Chen, K. H. Chen, and H. C. Cheng. J. Vac. Sci. Technol. B **18**, 2722 (2000). *Enhancement in field emission of silicon microtips by bias-assisted carburization*. doi:10.1116/1.1320809. 1

[15] M. Hajra, C. E. Hunt, M. Ding, O. Auciello, J. Carlisle, and D. M. Gruen. J. Appl. Phys. **94**, 4079 (2003). *Effect of gases on the field emission properties of ultrananocrystalline diamond-coated silicon field emitter arrays*. doi:10.1063/1.1594268. 1

[16] Z. Z. Bandic, E. A. Dobisz, T.-W. Wu, and T. R. Albrecht. Solid State Technology , S7 (2006). *Patterning on Hard Disk Drives*. 1

[17] K. Zhang, F. Rotter, M. Uhrmacher, C. Ronning, J. Krauser, and H. Hofsäss. New J. Phys. **9**, 29 (2007). *Ion induced nanoscale surface ripples on ferromagnetic films with correlated magnetic texture*. doi:10.1088/1367-2630/9/2/029.

[18] K. Zhang, M. Uhrmacher, H. Hofsäss, and J. Krauser. J. Appl. Phys. **103**, 083507 (2008). *Magnetic texturing of ferromagnetic thin films by sputtering induced ripple formation.* doi:10.1063/1.2905324.

[19] M. O. Liedke, B. Liedke, A. Keller, B. Hillebrands, A. Mücklich, S. Facsko, and J. Fassbender. Phys. Rev. B: Condens. Matter **75**, 220407 (2007). *Induced anisotropies in exchange-coupled systems on rippled substrates.* doi:10.1103/PhysRevB.75.220407.

[20] C. Teichert, J. J. de Miguel, and T. Bobek. J. Phys. Condens. Matter **21**, 224025 (2009). *Ion beam sputtered nanostructured semiconductor surfaces as templates for nanomagnet arrays.* doi:10.1088/0953-8984/21/22/224025. 1

[21] T. Lohner, E. Kótai, N. Khánh, Z. Tóth, M. Fried, K. Vedam, N. Nguyen, L. Hanekamp, and A. van Silfhout. Nucl. Instrum. Methods Phys. Res., Sect. B **85**, 335 (1994). *Ion-implantation induced anomalous surface amorphization in silicon.* doi:10.1016/0168-583X(94)95839-4. 1

[22] C. S. Madi, B. Davidovitch, H. B. George, S. A. Norris, M. P. Brenner, and M. J. Aziz. Phys. Rev. Lett. **101**, 246102 (2008). *Multiple Bifurcation Types and the Linear Dynamics of Ion Sputtered Surfaces.* doi:10.1103/PhysRevLett.101.246102. 2, 23, 27

[23] F. Frost, R. Fechner, B. Ziberi, J. Völlner, D. Flamm, and A. Schindler. J. Phys. Condens. Matter **21**, 224026 (2009). *Large area smoothing of surfaces by ion bombardment: fundamentals and applications.* doi:10.1088/0953-8984/21/22/224026. 2

[24] M. A. Makeev, R. Cuerno, and A. L. Barabási. Nucl. Instrum. Methods Phys. Res., Sect. B **197**, 185 (2002). *Morphology of ion-sputtered surfaces.* doi:10.1016/S0168-583X(02)01436-2. 2, 22, 25

[25] S. Facsko, T. Bobek, A. Stahl, and H. Kurz. Phys. Rev. B: Condens. Matter **69**, 153412 (2004). *Dissipative continuum model for self-organized pattern formation during ion-beam erosion.* doi:10.1103/PhysRevB.69.153412. 15, 25

[26] M. Castro, R. Cuerno, L. Vázquez, and R. Gago. Phys. Rev. Lett. **94**, 016102

(2005). *Self-Organized Ordering of Nanostructures Produced by Ion-Beam Sputtering*. doi:10.1103/PhysRevLett.94.016102.

[27] S. Vogel and S. J. Linz. Phys. Rev. B: Condens. Matter **75**, 085425 (2007). *Surface structuring by multiple ion beams*. doi:10.1103/PhysRevB.75.085425. 25

[28] W. L. Chan and E. Chason. J. Appl. Phys. **101**, 121301 (2007). *Making waves: Kinetic processes controlling surface evolution during low energy ion sputtering*. doi:10.1063/1.2749198. 2, 103

[29] G. Ozaydin, A. S. Öczan, Y. Wang, K. F. Ludwig, H. Zhou, R. L. Headrick, and D. P. Siddons. Appl. Phys. Lett. **87**, 163104 (2005). *Real-time x-ray studies of Mo-seeded Si nanodot formation during ion bombardment*. doi:10.1063/1.2099521. 2, 27, 31, 50, 59, 79, 128

[30] C. S. Madi, H. B. George, and M. J. Aziz. J. Phys. Condens. Matter **21**, 224010 (2009). *Linear stability and instability patterns in ion-sputtered silicon*. doi:10.1088/0953-8984/21/22/224010. 23, 24, 27, 31, 64

[31] S. Macko, F. Frost, B. Ziberi, D. F. Förster, and T. Michely. Nanotechnology **21**, 085301 (2010). *Is keV ion-induced pattern formation on Si(001) caused by metal impurities?* doi:10.1088/0957-4484/21/8/085301. 2, 56

[32] H. Hofsäss and K. Zhang. Appl. Phys. A **92**, 517 (2008). *Surfactant Sputtering*. doi:10.1088/0953-8984/21/22/224010. 2, 30, 69

[33] K. Zhang, H. Hofsäss, and H. Zutz. Nucl. Instrum. Methods Phys. Res., Sect. B **268**, 1967 (2010). *Nanoscale metal-silicide films prepared by surfactant sputtering and analyzed by RBS*. doi:10.1016/j.nimb.2010.02.110.

[34] N. Iwata, G. Mori, N. Arai, Y. Murakami, and A. Takahashi. Nanotechnology **21**, 365301 (2010). *Self-organized nanodot pattern fabrication using the reverse sputtering method*. doi:10.1088/0957-4484/21/36/365301. 26, 30, 128

[35] K. Zhang, M. Brötzmann, and H. Hofsäss. New J. Phys. **13**, 013033 (2011). *Surfactant driven self-organized surface patterns by ion beam erosion*. doi:10.1088/1367-2630/13/1/013033. 26, 27, 31, 74, 116, 118, 121, 123, 128

[36] O. El-Atwani, S. Ortoleva, A. Cimaroli, and J. P. Allain. Nanoscale Res. Lett. **6**, 403 (2011). *Formation of silicon nanodots via ion beam sputtering of ultrathin gold thin film coatings on Si.* doi:10.1186/1556-276X-6-403. 2

[37] M. Nastasi, J. W. Mayer, and J. K. Hirvonen, *Ion-Solid Interactions: Fundamentals and Applications*, Cambridge University Press, Cambridge, 1996. doi:10.1017/CBO9780511565007. 5, 7, 8, 9

[38] R. Behrisch, *Sputtering by Particle Bombardment I: Physical Sputtering of Single-Element Solids*, 1st Edition, Vol. 47, Springer, Berlin, Heidelberg, New York, 1981. 5, 10, 11

[39] R. Behrisch and K. Wittmaack, *Sputtering by Particle Bombardment III: Characteristics of Sputtered Particles, Technical Applications*, 1st Edition, Vol. 64, Springer, Berlin, Heidelberg, New York, 1991.

[40] R. Behrisch and W. Eckstein, *Sputtering by Particle Bombardment: Experiments and Computer Calculations from Threshold to MeV Energies*, 1st Edition, Vol. 110, Springer, Berlin, Heidelberg, 2007. 5, 10, 11, 12

[41] M. Castro and R. Cuerno. arXiv:1007.2144v1 (2010). *Ion induced viscous flow.* 6, 9, 23, 24, 57, 58, 93, 135

[42] W. Eckstein. Radiat. Eff. Defects Solids **130**, 239 (1994). *Backscattering and Sputtering with the Monte-Carlo Program TRIM.SP.* doi:10.1080/10420159408219787. 6, 12, 75

[43] F. Seitz and J. S. Koehler. Solid State Phys. **2**, 315 (1956). *Displacement of Atoms during Irradiation.* 9

[44] G. J. Iafrate, J. F. Ziegler, and M. J. Nass. J. Appl. Phys. **51**, 984 (1980). *Application of Lindhard's dielectric theory to the stopping of ions in solids.* doi:10.1063/1.327679.

[45] J. F. Ziegler and G. J. Iafrate. Radiat. Eff. **46**, 199 (1980). *The Stopping of Energetic Ions in Solids.* doi:10.1080/00337578008209171.

[46] J. P. Biersack and J. F. Ziegler. Nucl. Instrum. Methods **194**, 93 (1982). *Refined Universal Potentials in Atomic Collisions.* doi:10.1016/0029-554X(82)90496-7. 9

[47] H. Hofsäss, H. Feldermann, R. Merk, M. Sebastian, and C. Ronning. Appl. Phys. A **66**, 153 (1998). *Cylindrical spike model for the formation of diamond-like thin films by ion deposition.* doi:10.1007/s003390050652. 9

[48] Z. G. Wang, C. Dufour, E. Paumier, and M. Toulemonde. J. Phys. Condens. Matter **6**, 6733 (1994). *The S_e sensitivity of metals under swift-heavy-ion irradiation: a transient thermal process.* doi:10.1088/0953-8984/6/34/006. 9

[49] K. Nordlund, M. Ghaly, R. S. Averback, M. Caturla, T. Diaz de la Rubia, and J. Tarus. Phys. Rev. B: Condens. Matter **57**, 7556 (1998). *Defect production in collision cascades in elemental semiconductors and fcc metals.* doi:10.1103/PhysRevB.57.7556. 9

[50] W. Bock, H. Gnaser, and H. Oechsner. Surf. Sci. **282**, 333 (1993). *Modification of crystalline semiconductor surfaces by low-energy Ar^+ bombardment: Si(111) and Ge(100).* doi:10.1016/0039-6028(93)90938-G. 9, 49

[51] P. D. Edmondson, D. J. Riley, R. C. Birtcher, and S. E. Donnelly. J. Appl. Phys. **106**, 043505 (2009). *Amorphization of crystalline Si due to heavy and light ion irradiation.* doi:10.1063/1.3195081. 9

[52] W. Eckstein and W. Möller. Nucl. Instrum. Methods Phys. Res., Sect. B **7-8**, 727 (1985). *Computer Simulation of Preferential Sputtering.* doi:10.1016/0168-583X(85)90460-4. 10, 13

[53] W. Eckstein, V. I. Shulga, and J. Roth. Nucl. Instrum. Methods Phys. Res., Sect. B **153**, 415 (1999). *Carbon implantation into tungsten at elevated temperatures.* doi:10.1016/S0168-583X(98)01018-0. 11

[54] K. Schmid and J. Roth. J. Nucl. Mater. **313-316**, 302 (2003). *Erosion of high-Z metals with typical impurity ions.* doi:10.1016/S0022-3115(02)01346-6. 11

[55] L. G. Haggmark and W. D. Wilson. J. Nucl. Mater. **76 & 77**, 149 (1978). *Monte Carlo Studies of Sputtering.* doi:10.1016/0022-3115(78)90128-9. 11, 12

[56] J. P. Biersack and L. G. Haggmark. Nucl. Instrum. Methods **174**, 257 (1980). *A Monte Carlo Computer Program for the Transport of Energetic Ions in Amorphous Targets.* doi:10.1016/0029-554X(80)90440-1. 11

[57] J. P. Biersack and W. Eckstein. Appl. Phys. A **34**, 73 (1984). *Sputtering Sudies with the Monte Carlo Program TRIM.SP*. doi:10.1007/BF00614759. 11, 12, 46, 52, 53, 65, 76

[58] W. Möller and W. Eckstein. Nucl. Instrum. Methods Phys. Res., Sect. B **2**, 814 (1984). *TRIDYN - A TRIM Simulation code including dynamic composition changes*. 12

[59] W. W. Mullins. J. Appl. Phys. **28**, 333 (1957). *Theory of Thermal Grooving*. doi:10.1063/1.1722742. 13

[60] S. Vauth and S. G. Mayr. Phys. Rev. B: Condens. Matter **75**, 224107 (2007). *Relevance of surface viscous flow, surface diffusion, and ballistic effects in keV ion smoothing of amorphous surfaces*. doi:10.1103/PhysRevB.75.224107. 13, 14, 64

[61] J. Muñoz-García, M. Castro, and R. Cuerno. Phys. Rev. Lett. **96**, 086101 (2006). *Nonlinear Ripple Dynamics on Amorphous Surfaces Patterned by Ion Beam Sputtering*. doi:10.1103/PhysRevLett.96.086101. 13

[62] J. Muñoz-García, R. Cuerno, and M. Castro. Phys. Rev. B: Condens. Matter **78**, 205408 (2008). *Coupling of morphology to surface transport in ion-beam irradiated surfaces: Oblique incidence*. doi:10.1103/PhysRevB.78.205408. 13

[63] C. C. Umbach, R. L. Headrick, and K.-C. Chang. Phys. Rev. Lett. **87**, 246104 (2001). *Spontaneous Nanoscale Corrugation of Ion-Eroded SiO_2: The Role of Ion-Irradiation-Enhanced Viscous Flow*. doi:10.1103/PhysRevLett.87.246104. 14

[64] M. Moseler, P. Gumbsch, C. Casiraghi, A. C. Ferrari, and J. Robertson. Science **309**, 1545 (2005). *The Ultrasmoothness of Diamond-like Carbon Surfaces*. doi:10.1126/science.1114577. 14

[65] N. Anspach and S. J. Linz. J. Stat. Mech: Theory Exp. **2010**, P06023 (2010). *Modeling particle redeposition in ion-beam erosion processes under normal incidence*. doi:10.1088/1742-5468/2010/06/P06023. 15

[66] R. M. Bradley. Phys. Rev. B: Condens. Matter **83**, 075404 (2011). *Redeposition of sputtered material is a nonlinear effect*. doi:10.1103/PhysRevB.83.075404. 15

[67] R. M. Feenstra and G. S. Oehrlein. Appl. Phys. Lett. **47**, 97 (1985). *Surface morphology of oxidized and ion-etched silicon by scanning tunneling microscopy.* doi:10.1063/1.96431. 15

[68] N. Kalyanasundaram, M. Ghazisaeidi, J. B. Freund, and H. T. Johnson. Appl. Phys. Lett. **92**, 131909 (2008). *Single impact crater functions for ion bombardment of silicon.* doi:10.1063/1.2905297. 15

[69] A. Benninghoven. Z. Physik **230**, 403 (1970). *Die Analyse monomolekularer Festkörperoberflächenschichten mit Hilfe der Sekundärionenemission.* doi:10.1007/BF01394486. 15

[70] G. Carter. Vacuum **47**, 409 (1996). *The effects of ion bombardment sputtering and atomic transport related roughening and smoothing on depth profiling resolution.* doi:10.1016/0042-207X(95)00239-1. 15, 16, 135

[71] D. Cherns. Philos. Mag. **36**, 1429 (1977). *The surface structure of (111) gold films sputtered in the high voltage electron microscope: A theoretical model.* doi:10.1080/14786437708238526. 16

[72] P. Sigmund. Journal of Materials Science **8**, 1545 (1973). *A mechanism of surface micro-roughening by ion bombardment.* doi:10.1007/BF00754888. 16, 17

[73] R. J. Hoekstra, M. J. Kushner, V. Sukharev, and P. Schoenborn. J. Vac. Sci. Technol., B **16**, 2102 (1998). *Microtrenching resulting from specular reflection during chlorine etching of silicon.* doi:10.1116/1.590135. 17

[74] J. T. Drotar, Y.-P. Zhao, T.-M. Lu, and G.-C. Wang. Phys. Rev. B: Condens. Matter **61**, 3012 (2000). *Mechanisms for plasma and reactive ion etch-front roughening.* doi:10.1103/PhysRevB.61.3012. 17, 18, 19

[75] W. Hauffe. Phys. Status Solidi A **35**, K93 (1976). *Facetting Mechanism in the Sputtering Process.* doi:10.1002/pssa.2210350246. 17, 18, 65

[76] M. J. Nobes, J. S. Colligon, and G. Carter. J. Mater. Sci. **4**, 730 (1969). *The Equilibrium Topography of Sputtered Amorphous Solids.* doi:10.1007/BF00742430. 19, 20, 56, 65, 131

[77] G. Carter, J. S. Colligon, and M. J. Nobes. J. Mat. Sci. **6**, 115 (1971). *The Equilibrium Topography of Sputtered Amorphous Solids II*. doi:10.1007/BF00550340. 20, 56, 65, 131

[78] I. V. Katardjiev, G. Carter, and M. J. Nobes. Vacuum **39**, 1069 (1989). *A fundamental approach to surface evolution during growth and erosion*. doi:10.1016/0042-207X(89)91095-6.

[79] G. Carter. J. Phys. D: Appl. Phys. **34**, R1 (2001). *The physics and applications of ion beam erosion*. doi:10.1088/0022-3727/34/3/201. 19

[80] R. M. Bradley and J. M. E. Harper. J. Vac. Sci. Technol., A **6**, 2390 (1988). *Theory of ripple topography induced by ion bombardment*. doi:10.1116/1.575561. 21, 22, 23, 47, 64, 80

[81] P. Sigmund. Phys. Rev. **184**, 383 (1969). *Theory of Sputtering. I. Sputtering Yield of Amorphous and Polycrystalline Targets*. doi:10.1103/PhysRev.184.383. 22

[82] M. A. Makeev and A.-L. Barabási. Appl. Phys. Lett. **71**, 2800 (1997). *Ion-induced effective surface diffusion in ion sputtering*. doi:10.1063/1.120140. 22

[83] S. A. Norris, M. P. Brenner, and M. J. Aziz. J. Phys.: Condens. Matter **21**, 224017 (2009). *From crater functions to partial differential equations: a new approach to ion bombardment induced nonequilibrium pattern formation*. doi:10.1088/0953-8984/21/22/224017. 22, 23, 136

[84] S. A. Norris, J. Samela, L. Bukonte, M. Backman, F. Djurabekova, K. Nordlund, C. S. Madi, M. P. Brenner, and M. J. Aziz. Nat. Commun. **21**, 1 (2011). *Molecular dynamics of single-particle impacts predicts phase diagrams for large scale pattern formation*. doi:10.1038/ncomms1280. 22, 136

[85] B. Davidovitch, M. J. Aziz, and M. P. Brenner. Phys. Rev. B: Condens. Matter **76**, 205420 (2007). *On the stabilization of ion sputtered surfaces*. doi:10.1103/PhysRevB.76.205420. 22, 23

[86] G. Carter and V. Vyshnyakov. Phys. Rev. B: Condens. Matter **54**, 17647 (1996). *Roughening and Ripple Instabilities on Ion-Bombarded Si*. doi:10.1103/PhysRevB.54.17647. 23

[87] C. S. Madi, E. Anzenberg, K. F. Ludwig, and M. J. Aziz. Phys. Rev. Lett. **106**, 066101 (2011). *Mass Redistribution Causes the Structural Richness of Ion-Irradiated Surfaces*. doi:10.1103/PhysRevLett.106.066101. 23

[88] C. S. Madi, S. A. Norris, and M. J. Aziz. unpublished (2011). *Multiple Scattering, Rather than Stress, Causes the Low Energy-Low Angle Constant Wavelength Bifurcation of Argon Ion Bombarded Silicon surfaces*. 23, 27, 58

[89] S. Park, B. Kahng, H. Jeong, and A.-L. Barabási. Phys. Rev. Lett. **83**, 3486 (1999). *Dynamics of Ripple Formation in Sputter Erosion: Nonlinear Phenomena*. doi:10.1103/PhysRevLett.83.3486. 25

[90] B. Kahng, H. Jeong, and A. L. Barabasi. Appl. Phys. Lett. **78**, 805 (2001). *Quantum dot and hole formation in sputter erosion*. doi:10.1063/1.1343468. 25

[91] P. Hohenberg and B. I. Shraiman. Physica D **37**, 109 (1989). *Chaotic Behavior of an Extended System*. doi:10.1016/0167-2789(89)90121-8. 25

[92] R. Cuerno and A.-L. Barabási. Phys. Rev. Lett. **74**, 4746 (1995). *Dynamic Scaling of Ion-Sputtered Surfaces*. doi:10.1103/PhysRevLett.74.4746.

[93] M. Rost and J. Krug. Phys. Rev. Lett. **75**, 3894 (1995). *Anisotropic Kuramoto-Sivashinsky Equation for Surface Growth and Erosion*. doi:10.1103/PhysRevLett.75.3894. 25

[94] V. B. Shenoy, W. L. Chan, and E. Chason. Phys. Rev. Lett. **98**, 256101 (2007). *Compositionally Modulated Ripples Induced by Sputtering of Alloy Surfaces*. doi:10.1103/PhysRevLett.98.256101. 25, 128

[95] J. Zhou and M. Lu. Phys. Rev. B: Condens. Matter **82**, 125404 (2010). *Mechanism of Fe impurity motivated ion-nanopatterning of Si(100) surfaces*. doi:10.1103/PhysRevB.82.125404. 25, 123, 128

[96] R. M. Bradley and P. D. Shipman. Phys. Rev. Lett. **105**, 145501 (2010). *Spontaneous Pattern Formation Induced by Ion Bombardment of Binary Compounds*. doi:10.1103/PhysRevLett.105.145501. 25, 128

[97] R. Kree, T. Yasseri, and A. K. Hartmann. Nucl. Instrum. Methods Phys. Res., Sect. B **267**, 1403 (2009). *Surfactant Sputtering: Theory of a new method of*

surface nanostructuring by ion beams. doi:10.1016/j.nimb.2009.01.150. 25

[98] J. W. Cahn. Acta Metall. **9**, 795 (1961). *On Spinodal Decomposition*. doi:10.1016/0001-6160(61)90182-1. 25

[99] M. Atzmon, D. A. Kessler, and D. J. Srolovitz. J. Appl. Phys. **72**, 442 (1992). *Phase Separation During Film Growth*. doi:10.1063/1.351872. 25

[100] K. Fukutani, K. Tanji, T. Saito, and T. Den. J. Appl. Phys. **98**, 033507 (2005). *Phase-separated Al–Si thin films*. doi:10.1063/1.1994942. 26

[101] N. Yasui, R. Horie, Y. Ohashi, K. Tanji, and T. Den. Adv. Mater. **19**, 2797 (2007). *Well-Aligned Nanocylinder Formation in Phase-Separated Metal-Silicide–Silicon and Metal-Germanide–Germanium Systems*. doi:10.1002/adma.200700726. 26, 122

[102] K. Fukutani, K. Tanji, T. Saito, and T. Den. Jpn. J. Appl. Phys. **47**, 1140 (2008). *Fabrication of Well-Aligned Al Nanowire Array Embedded in Si Matrix Using Limited Spinodal Decomposition*. doi:10.1143/JJAP.47.1140. 25, 26

[103] P. Haymann. C.R. Hebd. Seances Acad. Sci. **248**, 2472 (1959). *Action des ions argon de faibles énergies sur des surfaces d´uranium*. 26

[104] M. Navez, C. Sella, and D. Chaperot. C.R. Hebd. Seances Acad. Sci. **254**, 240 (1962). *Étude de l´attaque du verre par bombardement ionique*. 26

[105] J. A. Sánchez-García, L. Vázquez, R. Gago, A. Redondo-Cubero, J. M. Albella, and Z. Czigány. Nanotechnology **19**, 224009 (2008). *Tuning the surface morphology in self-organized ion beam nanopatterning of Si(001) via metal incorporation: from holes to dots*. doi:10.1088/0957-4484/19/35/355306. 27, 31, 33, 70, 73, 128

[106] M. Cornejo, B. Ziberi, C. Meinecke, D. Hirsch, J. W. Gerlach, T. Höche, F. Frost, and B. Rauschenbach. Appl. Phys. A **102**, 593 (2011). *Self-organized patterning on Si(001) by ion sputtering with simultaneous metal incorporation*. doi:10.1007/s00339-011-6246-y. 31, 116

[107] M. Cornejo, B. Ziberi, C. Meinecke, and F. Frost. Appl. Surf. Sci. **257**, 8659 (2011). *Formation of two ripple modes on Si by ion erosion with simultaneous Fe incorporation.* doi:10.1016/j.apsusc.2011.05.044. 27, 31

[108] F. Ludwig, C. R. Eddy, O. Malis, and R. Headrick. Appl. Phys. Lett. **81**, 2770 (2002). *Si(100) surface morphology evolution during normal-incidence sputtering with 100–500 eV Ar^+ ions.* doi:10.1063/1.1513655. 27

[109] V. Vishnyakov and G. Carter. Nucl. Instrum. Methods Phys. Res., Sect. B **106**, 174 (1995). *Ne^+, Ar^+ and Xe^+ ion bombardment induced and suppressed topography on Si.* doi:10.1016/0168-583X(95)00699-0. 28, 56, 92

[110] K. Zhang, H. Hofsäss, F. Rotter, M. Uhrmacher, C. Ronning, and J. Krauser. Surf. Coat. Technol. **203**, 2395 (2009). *Morphology of Si surfaces sputter-eroded by low-energy Xe-ions at glancing incident angle.* doi:10.1016/j.surfcoat.2009.02.105. 28, 52, 53

[111] A. Keller, S. Facsko, and W. Möller. New J. Phys. **10**, 063004 (2008). *Minimization of topological defects in ion-induced ripple patterns on silicon.* doi:10.1088/1367-2630/10/6/063004. 28

[112] A. Keller, S. Roßbach, S. Facsko, and W. Möller. Nanotechnology **19**, 135303 (2008). *Simultaneous formation of two ripple modes on ion sputtered silicon.* doi:10.1088/0957-4484/19/13/135303. 28, 65

[113] A. Keller and S. Facsko. Phys. Rev. B: Condens. Matter **82**, 155444 (2010). *Tuning the Quality of Nanoscale Ripple Patterns by Sequential Ion-Beam Sputtering.* doi:10.1103/PhysRevB.82.155444. 28

[114] G. W. Lewis, G. Kiriakides, G. Carter, and M. J. Nobes. Surf. Interface Anal. **4**, 141 (1982). *Ion Bombardment Induced Surface Topography Modification of Clean and Contaminated Single Crystal Cu and Si.* doi:10.1002/sia.740040404. 28

[115] A. Hanisch, A. Biermanns, J. Grenzer, S. Facsko, and U. Pietsch. J. Phys. D: Appl. Phys. **43**, 112001 (2010). *Xe ion beam induced rippled structures on differently oriented single-crystalline Si surfaces.* doi:10.1088/0022-3727/43/11/112001. 29

[116] F. Frost, R. Fechner, D. Flamm, B. Ziberi, W. Frank, and A. Schindler. Appl. Phys. A **78**, 651 (2004). *Ion beam assisted smoothing of optical surfaces*. doi:10.1007/s00339-003-2274-6. 29, 59

[117] G. Carter, V. Vishnyakov, Y. Martynenko, and M. J. Nobes. J. Appl. Phys. **78**, 3559 (1995). *The effects of ion species and target temperature on topography development on ion bombarded Si*. doi:10.1063/1.359931. 29, 30, 40, 80

[118] J. Erlebacher, M. J. Aziz, E. Chason, M. B. Sinclair, and J. A. Floro. Phys. Rev. Lett. **82**, 2330 (1999). *Spontaneous Pattern Formation on Ion Bombarded Si(001)*. doi:10.1103/PhysRevLett.82.2330. 30, 67, 68, 80

[119] J. Erlebacher, M. J. Aziz, E. Chason, M. B. Sinclair, and J. A. Floro. Phys. Rev. Lett. **84**, 5800 (2000). *Nonclassical smoothening of nanoscale surface corrugations*. doi:10.1103/PhysRevLett.84.5800.

[120] A.-D. Brown and J. Erlebacher. Phys. Rev. B: Condens. Matter **72**, 075350 (2005). *Temperature and fluence effects on the evolution of regular surface morphologies on ion-sputtered Si(111)*. doi:10.1103/PhysRevB.72.075350. 30, 67, 68, 80

[121] G. Carter, V. Vishnyakov, and M. J. Nobes. Nucl. Instrum. Methods Phys. Res., Sect. B **115**, 440 (1996). *Ripple topography development on ion bombarded Si*. doi:10.1016/0168-583X(95)01522-1. 30

[122] G. K. Wehner and D. J. Hajicek. J. Appl. Phys. **42**, 1145 (1971). *Cone Formation on Metal Targets during Sputtering*. doi:10.1063/1.1660158. 30

[123] J. Punzel and W. Hauffe. Phys. Status Solidi A **14**, K97 (1972). *Development of Relief Structures on Si Surfaces by Ion Bombardment*. doi:10.1002/pssa.2210140241. 30

[124] R. S. Robinson and S. M. Rossnagel. J. Vac. Sci. Technol. **21**, 790 (1982). *Ion-beam-induced topography and surface diffusion*. doi:10.1116/1.571826. 30

[125] S. M. Rossnagel and R. S. Robinson. J. Vac. Sci. Technol. **20**, 195 (1982). *Surface diffusion activation energy determination using ion beam microtexturing*. doi:10.1116/1.571356. 30

[126] M. Tanemura, H. Yamauchi, Y. Yamane, T. Ohita, and S. Tanemura. Nucl. Instrum. Methods Phys. Res., Sect. B **215**, 137 (2004). *Controlled fabrication of Mo-seeded Si microcones by Ar^+-ion bombardment.* doi:10.1016/j.nimb.2003.08.025. 30

[127] G. Ozaydin-Ince and K. F. Ludwig Jr. Phys. Rev. B: Condens. Matter **21**, 224008 (2009). *In situ x-ray studies of native and Mo-seeded surface nanostructuring during ion bombardment of Si(100).* doi:10.1088/0953-8984/21/22/224008. 31, 32, 59, 79, 86

[128] C. Teichert, C. Hofer, and G. Hlawacek. Adv. Eng. Mater. **8**, 1057 (2006). *Self-organization of Nanostructures in Inorganic and Organic Semiconductor Systems.* doi:10.1002/adem.200600142. 31, 79

[129] J. A. Sánchez-García, R. Gago, R. Caillard, A. Redondo-Cubero, J. A. Martin-Gago, F. J. Palomares, M. Fernández, and L. Vázquez. J. Phys. Condens. Matter **21**, 224009 (2009). *Production of nanohole/nanodot patterns on Si(001) by ion beam sputtering with simultaneous metal incorporation.* doi:10.1088/0953-8984/21/22/224009. 31, 32, 33, 80, 86, 121

[130] J. Muñoz-García, R. Gago, L. Vázquez, J. A. Sánchez-García, and R. Cuerno. Phys. Rev. Lett. **104**, 026101 (2010). *Observation and Modeling of Interrupted Pattern Coarsening: Surface Nanostructuring by Ion Erosion.* doi:10.1103/PhysRevLett.104.026101. 31, 128

[131] R. Gago, L. Vázquez, R. Cuerno, M. Varela, C. Ballesteros, and J. M. Albella. Appl. Phys. Lett. **78**, 3316 (2001). *Production of ordered silicon nanocrystals by low-energy ion sputtering.* doi:10.1063/1.1372358. 31, 74, 119

[132] R. Gago, L. Vázquez, O. Plantevin, J.-A. Sánchez-García, M. Varela, M. C. Ballesteros, J. M. Albella, and T. H. Metzger. Phys. Rev. B: Condens. Matter **73**, 155414 (2006). *Temperature influence on the production of nanodot patterns by ion beam sputtering of Si(001).* doi:10.1103/PhysRevB.73.155414. 32, 33, 80, 85, 128

[133] W.-B. Fan, W.-Q. Li, L.-J. Qi, H.-T. Sun, J. Luo, Y.-Y. Zhao, and M. Lu. Nanotechnology **16**, 1526 (2005). *On the role of ion flux in nanostructuring by ion sputter erosion.* doi:10.1088/0957-4484/16/9/020.

[134] W.-B. Fan, L. Ling, L.-J. Qi, W.-Q. Li, H.-T. Sun, C.-X. Gu, Y. Y. Zhao, and M. Lu. J. Phys. Condens. Matter **18**, 3367 (2006). *The effect of redeposition on the ion flux dependence of Si dot pattern formation during ion sputter erosion.* doi:10.1088/0953-8984/18/13/004.

[135] B. Ziberi, F. Frost, B. Rauschenbach, and T. Höche. Appl. Phys. Lett. **87**, 033113 (2005). *Highly ordered self-organized dot patterns on Si surfaces by low-energy ion-beam erosion.* doi:10.1063/1.2000342. 31

[136] B. Ziberi, M. Cornejo, F. Frost, and B. Rauschenbach. J. Phys. Condens. Matter **21**, 224003 (2009). *Highly ordered nanopatterns on Ge and Si surfaces by ion beam sputtering.* doi:10.1088/0953-8984/21/22/224003. 31, 32, 40, 116

[137] R. Gago, L. Vázquez, R. Cuerno, M. Varela, C. Ballesteros, and J. M. Albella. Nanotechnology **13**, 304 (2002). *Nanopatterning of silicon surfaces by low-energy ion-beam sputtering: dependence on the angle of ion incidence.* doi:10.1088/0957-4484. 31, 32, 128

[138] B. Ziberi, F. Frost, T. Höche, and B. Rauschenbach. Phys. Rev. B: Condens. Matter **72**, 235310 (2005). *Ripple pattern formation on silicon surfaces by low-energy ion-beam erosion: Experiment and theory.* doi:10.1103/PhysRevB.72.235310. 31, 32, 40, 116

[139] B. Ziberi, F. Frost, T. Höche, and B. Rauschenbach. Vacuum **81**, 155 (2006). *Ion-induced self-organized dot and ripple patterns on Si surfaces.* doi:10.1016/j.vacuum.2006.03.018. 32, 74, 119

[140] B. Ziberi, F. Frost, and B. Rauschenbach. J. Vac. Sci. Technol., A **24**, 1344 (2006). *Formation of large-area nanostructures on Si and Ge surfaces during low energy ion beam erosion.* doi:10.1116/1.2188415. 31, 32

[141] J. Zhou, S. Facsko, M. Lu, and W. Möller. J. Appl. Phys. **109**, 104315 (2011). *Nanopatterning of Si surfaces by normal incident ion erosion: Influence of iron incorporation on surface morphology evolution.* doi:10.1063/1.3585796. 31, 74

[142] B. Ziberi, F. Frost, M. Tartz, H. Neumann, and B. Rauschenbach. Appl. Phys. Lett. **92**, 063102 (2008). *Ripple rotation, pattern transitions, and long range*

ordered dots on silicon by ion beam erosion. doi:10.1063/1.2841641. 31, 116

[143] J. Zhou, M. Hildebrandt, and M. Lu. J. Appl. Phys. **109**, 053513 (2011). *Self-organized antireflecting nano-cone arrays on Si(100) induced by ion bombardment.* doi:10.1063/1.3560539. 33, 104

[144] B. Predel, Fe-si (iron-silicon), Madelung, O (ed.). SpringerMaterials – The Landolt-Börnstein Database (http://www.springermaterials.com). doi:10.1007/10474837_1340. 33, 34, 120

[145] J. M. Gallego, J. M. García, J. Alvarez, and R. Miranda. Phys. Rev. B: Condens. Matter **46**, 13339 (1992). *Metallization-induced spontaneous silicide formation at room temperature: The Fe/Si case.* doi:10.1103/PhysRevB.46.13339. 34

[146] Q.-G. Zhu, H. Iwasaki, E. D. Williams, and R. L. Park. J. Appl. Phys. **60**, 2629 (1986). *Formation of Iron Silicide Films.* doi:10.1063/1.337136. 35

[147] D. F. Förster. Doctoral Thesis (2011). *EuO and Eu on metal crystals and graphene: interface effects and epitaxial films,* II. Physikalisches Institut, Universität zu Köln. 38, 39

[148] I. Horcas, R. Fernández, J. M. Gómez-Rodríguez, J. Colchero, J. Gómez-Herrero, and A. M. Baro. Rev. Sci. Instrum. **78**, 013705 (2007). *WSXM: A software for scanning probe microscopy and a tool for nanotechnology.* doi:10.1063/1.2432410. 44, 45, 46

[149] T. K. Chini, D. P. Datta, and S. R. Bhattacharyya. J. Phys. Condens. Matter **21**, 224004 (2009). *Ripple formation on silicon by medium energy ion bombardment.* doi:10.1088/0953-8984/21/22/224004. 45

[150] E. W. and P. R. J. Nucl. Mater. **320**, 209 (2003). *New fit formulae for the sputtering yield.* doi:10.1016/S0022-3115(03)00192-2. 46, 52, 53

[151] Q. Wei, J. Lian, L. A. Boatner, L. M. Wang, and R. C. Ewing. Phys. Rev. B: Condens. Matter **80**, 085413 (2009). *Propagation of ripples on pyrochlore induced by ion beam bombardment.* doi:10.1103/PhysRevB.80.085413. 56

[152] J. Völlner, B. Ziberi, F. Frost, and B. Rauschenbach. J. Appl. Phys. **109**, 043501 (2011). *Topography evolution mechanism on fused silica during low-energy ion beam sputtering.* doi:10.1063/1.3549170. 56

[153] C. M. Neuman, N. Lancaster, and W. G. Nickling. Sedimentology **47**, 211 (2000). *The effect of unsteady winds on sediment transport on the stoss slope of a transverse dune, Silver Peak, NV, USA.* doi:10.1046/j.1365-3091.2000.00289.x. 57, 135

[154] H. El belrhiti and S. Douady. Geomorphology **125**, 558 (2011). *Equilibrium versus disequilibrium of barchan dunes.* doi:10.1016/j.geomorph.2010.10.025. 57, 135

[155] M. Engler. Diploma Thesis (2010). *Nanostrukturierung von Si(001) mittels Ionenstrahlerosion,* II. Physikalisches Institut, Universität zu Köln. 64, 65, 110

[156] N. Kalyanasundaram, M. C. Moore, J. B. Freund, and H. T. Johnson. Acta Mater. **54**, 483 (2006). *Stress Evolution due to Medium-Energy Ion Bombardment of Silicon.* doi:10.1016/j.actamat.2005.09.028. 64

[157] N. Kalyanasundaram, M. Wood, J. B. Freund, and H. T. Johnson. Mech. Res. Commun. **35**, 50 (2007). *Stress Evolution to Steady State in Ion Bombardment of Silicon.* doi:10.1016/j.mechrescom.2007.08.009. 64

[158] A. Keller, R. Cuerno, S. Facsko, and W. Möller. Phys. Rev. B: Condens. Matter **79**, 115437 (2009). *Anisotropic scaling of ripple morphologies on high-fluence sputtered silicon.* doi:10.1103/PhysRevB.79.115437. 65

[159] S. Adachi and T. Aoki. J. Appl. Phys. **71**, 3313 (1992). *Optical properties of Si partially amorphized by ion implantation.* doi:10.1063/1.350951. 66

[160] H. Mori, S. Adachi, and M. Takahashi. J. Appl. Phys. **90**, 87 (2001). *Optical properties of self-ion-implanted S(100) studied by spectroscopic ellipsometry.* doi:10.1063/1.1371951. 66

[161] F. A. Stevie and R. G. Wilson. J. Vac. Sci. Technol., A **9**, 3064 (1991). *Relative sensitivity factors for positive atomic and molecular ions sputtered from Si and GaAs.* doi:10.1116/1.577174. 72

[162] R. G. Wilson. Int. J. Mass Spectrom. Ion Processes **143**, 43 (1995). *SIMS quantification in Si, GaAs, and diamond - an update.* doi:10.1016/0168-1176(94)04136-U. 72

[163] B. Predel, Pd-si (palladium-silicon), Madelung, O (ed.). SpringerMaterials – The Landolt-Börnstein Database (http://www.springermaterials.com). doi:10.1007/10542753_2445. 78

[164] B. Predel, Ag-si (silver-silicon), Madelung, O (ed.). SpringerMaterials – The Landolt-Börnstein Database (http://www.springermaterials.com). doi:10.1007/10000866_68. 78

[165] J. Punzel. Phys. Status Solidi **24**, K1 (1967). *Temperature Dependence of the Surface Structure of Ion-Bombarded Si Single Crystals.* doi:10.1002/pssb.19670240139. 80

[166] G. Carter, M. J. Nobes, F. Paton, and J. S. Williams. Radiat. Eff. Defects Solids **33**, 65 (1977). *Ion Bombardment Induced Ripple Topography on Amorphous Solids.* doi:10.1080/00337577708237469. 92

[167] G. K. Wehner. Appl. Phys. Lett. **43**, 366 (1983). *Whisker growth and cone formation on metal surfaces under ion bombardment.* doi:10.1063/1.94339. 103

[168] R. L. Schwoebel. J. Appl. Phys. **40**, 614 (1969). *Step Motion on Crystal Surfaces. II.* doi:10.1063/1.1657442. 103

[169] L. Vočadlo, K. S. Knight, G. D. Price, and I. G. Wood. Phys. Chem. Minerals **29**, 132 (2002). *Thermal expansion and crystal structure of FeSi between 4 and 1173 K determined by time-of-flight neutron powder diffraction.* doi:10.1007/s002690100202. 104

[170] D. Askeland (Ed.), *Materialwissenschaften*, Elsevier - Spektrum Akademischer Verlag, Heidelberg, 1996. 104

[171] D. Leong, M. Harry, K. J. Reeson, and K. P. Homewood. Nature **387**, 686 (1997). *A silicon/iron-disilicide light-emitting diode operating at a wavelength of 1.5 µm.* 105

[172] N. Bibić, S. Dhar, K. Lieb, M. Milosavljevic, P. Schaaf, Y.-L. Huang, M. Seibt, K. Homewood, and C. McKinty. Surf. Coat. Technol. **158-159**, 198 (2002).

Structural and optical properties of β-$FeSi_2$ layers grown by ion beam mixing. doi:10.1016/S0257-8972(02)00205-0. 105

[173] Y. Maeda, Y. Terai, M. Itakura, and N. Kuwano. Thin Solid Films **461**, 160 (2004). *Photoluminescence properties of ion beam synthesized β-$FeSi_2$.* doi:10.1016/j.tsf.2004.02.057. 105

[174] Z. Yang and K. P. Homewood. J. Appl . Phys. **79**, 4312 (1996). *Effect of annealing temperature on optical and structural properties of ion-beam-synthesized semiconducting $FeSi_2$ layers.* doi:10.1063/1.361879. 105

[175] E. Moroni, W. Wolf, J. Hafner, and R. Podloucky. Phys. Rev. B **59**, 12860 (1999). *Cohesive, structural and electronic properties of Fe-Si compounds.* doi:10.1103/PhysRevB.59.12860. 121

[176] R. Cuerno, M. Castro, J. M. noz García, R. Gago, and L. Vázquez. Nucl. Instrum. Methods Phys. Res., Sect. B **269**, 894 (2011). *Nanoscale pattern formation at surfaces under ion-beam sputtering: A perspective from continuum models.* doi:10.1016/j.nimb.2010.11.072. 135

[177] K. Kyuno, D. G. Cahill, R. S. Averback, J. Tarus, and K. Nordlund. Phys. Rev. Lett. **83**, 4788 (1999). *Surface Defects and Bulk Defect Migration Produced by Ion Bombardment of Si(001).* doi:10.1103/PhysRevLett.83.4788. 135

A Publications

Parts of the results presented in this thesis were published in the following articles:

S. Macko, J. Grenzer, F. Frost, M. Engler, M. Fritzsche, D. Hirsch, A. Mücklich and T. Michely, unpublished. *Iron assisted ion beam patterning on Si(001) in the crystalline regime.*

S. Macko, F. Frost, M. Engler, D. Hirsch, T. Höche, J. Grenzer and T. Michely. New J. Phys. **13**, 073017 (2011). *Phenomenology of iron-assisted ion beam pattern formation on Si(001).* doi: 10.1088/1367-2630/13/7/073017

S. Macko, F. Frost, B. Ziberi, D. F. Förster and T. Michely. Nanotechnology **21**, 085301 (2010). *Is keV ion-induced pattern formation on Si(001) caused by metal impurities?* doi: 10.1088/0957-4484/21/8/085301

Further scientific publications:

R. Meinhardt, S. Macko, B. Qi, A. Draude, Y. Zhao, W. Wenig and H. Franke. J. Phys. D: Appl. Phys. **41**, 195303 (2008). *Photoinduced Molecular Motion in an Azobenzene-Containing Diblock Copolymer.*
doi: 10.1088/0022-3727/41/19/195303

S. Macko, R. Meinhardt, A. Draude, Y. Zhao and H. Franke. Proc. SPIE 6796 **6796**, L7961 (2007). *Optical characterization of thin layers of an azo di-block copolymer.* doi:10.1117/12.778926

Press Release

S. Macko et al. Impurities possess nanopatterning powers:
http://iopscience.iop.org/0957-4484/labtalk-article/41927

B Ripple Erosion Velocity Simulation: Gnuplot Code

```
set angles degrees \\
set hidden3d \\
set isosamples 200; \\
set pm3d \\
set palette rgbformulae -25, -24, -32 \\

set xrange [0.:1] \\
set yrange [0.:0.6966] #plots x and y with same scale \\
set zrange [0:10] \\
set cbrange [1:6.5] # sets range of colour scale \\
set title "Erosion rate at a certain facet angle combination" \\
set xlabel 'Base' \\
set ylabel 'Height' \\
set view map \\

#                      /ions    ions/           \\
#          \          /            /talpha_/     \\
#           \ tbeta /             /    __/       \\
#            \     /             /   _/          \\
#             \   /    __/\     /  _/            \\
#              \ /  __/   |\  / _/               \\
#               \__/      | \/_/                 \\
#             __/         |  \                   \\
#          __/ a         y|   \ b                \\
#       __/               |    \                 \\
#    __/                  |     \                \\
#   / beta      x         | alpha\               \\
# -------------------------------               \\
#                  c

#global angle of incidence \\
vartheta=75 \\
#Ions impinging per time unit \\
J=1.0 \\
#length of the base of the triangle \\
c=1.0 \\

#facet slope \\
beta(x,y)=atan(y/x) \\
```

```
alpha(x,y)=atan(y/(c-x)) \\

#facet length \\
b(x,y)=sqrt((c-x)*(c-x)+y*y) \\
a(x,y)=sqrt(x*x+y*y) \\

#local angles of incidence theta \\
talpha(x,y)=vartheta-alpha(x,y) \\
tbeta(x,y)=vartheta+beta(x,y) \\

#projection of the facet onto the normal \\
#of the incoming ion beam \\
pa(x,y)=a(x,y)*cos(tbeta(x,y)) \\
pb(x,y)=b(x,y)*cos(talpha(x,y)) \\

#relative fraction of ions impinging on each facet\\
#Ja + Jb = const.\\
Ja(x,y)=J*(pa(x,y)/(pa(x,y)+pb(x,y))) \\
Jb(x,y)=J*(pb(x,y)/(pa(x,y)+pb(x,y))) \\

#constants for 2 keV Kr+ on Si estimated by \\
#fitting the TRIM.SP simulation data \\
k=0.87234 \\
#k: in publication of Eckstein labeled "c" \\
f=4.32554 \\
b=1.46367 \\
pi=3.141592654 \\

#Sputtering yield curve for 2 keV Kr+ on Si \\
#calculated by Eckstein's formula \\
#S(x)=1.07*(cos(((((x)*pi)/180)**k)*180/pi))**(-f) \\
#*exp(b*(1-1/(cos(((((x)*pi)/180)**k)*180/pi)))) \\

#Sputtering yield for the local angles of each facet \\
#Y(tbeta) \\
Ybeta(x,y)=1.07* \\
(cos(((((tbeta(x,y))*pi)/180)**k)*180/pi))**(-f) \\
*exp(b*(1-1/(cos(((((tbeta(x,y))*pi)/180)**k)*180/pi)))) \\
#Y(talpha) \\
Yalpha(x,y)=1.07* \\
(cos(((((talpha(x,y))*pi)/180)**k)*180/pi))**(-f) \\
*exp(b*(1-1/(cos(((((talpha(x,y))*pi)/180)**k)*180/pi)))) \\

f(x,y)=Ja(x,y)*Ybeta(x,y)+Jb(x,y)*Yalpha(x,y) \\

splot alpha(x,y)<vartheta && \\
beta(x,y)<(90-vartheta) ? f(x,y) :0/0 with pm3d \\
```

C Acknowledgements

I would like to express my gratitude to all the people who supported and inspired me during my thesis work and without whom this thesis could not have been possible.

First of all, I would like to thank my supervisor Professor Thomas Michely for giving me the opportunity to work in this exciting field of science described in the present thesis. I am deeply grateful for his continuous support and advice and for sharing his deep understanding of physics and technical insight. I am honoured to have been working with him.

I would also like to express my gratitude to Professor Hans Hofsäss for being co-referee of this thesis, it was also beneficial that he pursues his research interests in the fields of the present thesis. Our related scientific investigations inspired one another. My thanks also to his Postdoc Kun Zhang for the valuable discussions at several spring meetings. I would like to thank Prof. Joachim Krug for his time and for being in my thesis committee.

Thanks to current and former members of the entire working group of Prof. Thomas Michely for the friendly atmosphere. Thanks for all the inspiring scientific and non-scientific discussions we had - especially during our gladsome group meetings. Furthermore I enjoyed the companionship by playing tabletop football, having barbecues and by relishing *Kölsch* - we should have done this more often.

I want to express my gratitude to Daniel Förster my office colleague who was guiding me from the very beginning of my thesis. Many thanks for introducing me into the complex ultra high vacuum scanning tunneling microscopy apparatus and for always being available and open to any questions I faced. His constant help – discussions about science and instrumentation – were always valuable to me.

I want to thank Martin Engler for discussing experimental and theoretical questions we encountered on our common path in the world of ion beam patterning. Thanks for proofreading of the whole thesis. Moreover, he assisted faithfully concerning my problems with LaTeX and Gnuplot.

I thank Georgia Lewes-Malandrakis, Jürgen Klinkhammer, Sebastian Standop and Timm Gerber for their encouragement and for their 'colourful' suggestions while proofreading parts of my thesis. My explicit thanks to Alex Redinger, Alpha T. N'Diaye, Sebastian Bleikamp, Carsten Busse and Johann Coraux for their worthwile suggestions to all my concerns expecially in the beginning of my thesis. I thank Sven Runte, Matthias Winter, Rabia Djemour, Stefan Schumacher, Sven Müller, Fabian Craes, Patrick Stratmann, Andreas Jacobi, Charlotte Herbig, Torben Moyzio and Ulrike Schröder for the enjoyable working atmosphere and help. Special thanks to Anna Lindner and Paul Rosenberger for performing the facet orientation analysis during their mini-research in our working group.

Especially, I want to thank Norbert Henn for being an excellent technician. He dared all technical problems and solved them in a masterly manner. Special

thanks to Ralf Müller and Martin Valldor for their help concerning my work in the chemistry laboratory. My cordial thanks to the mechanics workshop of the 2nd Institute of Physics under the leadership of Mr W. Külzer. Thanks for realizing some of my impossible constructions with meticulous attention to detail. My respect and admiration goes to Mr P. Hansmann for his unsurpassed skills in the field of precision mechanic. Furthermore, I thank the electronics workshop of the 2nd Institute of Physics under the leadership of Mr H.-G. Menz for their good work. I thank Ms D. Hochscheid for delivering me promptly all the needed but rarely available publications.

I gratefully acknowledge the financial support by *Deutsche Forschungsgemeinschaft* through *Forschergruppe 845* and I thank for the fruitful cooperation and discussions with the members of the *Forschergruppe 845*. In this regard I thank Prof. B. Rauschenbach for facilitating support and cooperation by the *Leibniz-Institut für Oberflächenmodifizierung e.V.* and I want to thank Frank Frost for the interesting and productive collaboration and his helpful comments and remarks as well as for performing AFM measurements. Dietmar Hirsch conducted with his outstanding capability the SEM and SIMS measurements. Thanks to Thomas Höche for conducting high resolution TEM and EELS measurements and Agnes Mill for optical micro phase interference measurements. Furthermore, I thank Marina Cornejo, Bashkim Ziberi and Jens Völlner for helpful discussions and the good time we had during our meetings of the *Forschergruppe 845*. Moreover, I thank Hubert Gnaser for his advice related to quantification of the SIMS data.

Special thanks to Jörg Grenzer for coordinating the collaboration with the *Helmholtz-Zentrum Dresden-Rossendorf*, for performing the GI-XRD measurements and for proofreading of a part of the present thesis. I thank Monika Fritzsche for making the exceptionally well sample preparation by FIB and Arndt Mücklich for skilful TEM, EELS and EDX measurements.

I thank Rodolfo Cuerno for a good time in Montréal and a highly interesting conversation about his work on *solid flow*. Special thanks to Jing Zhou for the illuminating conversations we had about the influence of iron on ion beam pattern formation already in the beginning of the project. Likewise, I thank Karl-Heinz Heinig and Charbel Madi for seminal discussions on the phenomenology of ion beam pattern formation.

Special thanks to my father-in-law Bernd Eifler for proofreading my thesis and providing me with useful revisions without changing my writing style. I also thank Anette Eifler for her pleasant support.

I would like to say thanks to my parents Anka and Mihal Macko for their love and for standing always by my side and provide their unconditional support with all possible ways. My appreciation to my brother Eduard, his wife Susanne and their lovely kids Jana and Mia for their warm-heartedness.

Finally, I want to thank my wife Nina she was always there and willing to help me with all my concerns. Her encouragement will be unforgettable. You are special! Thanks to God. Thanks to my whole family, I love you all. Thanks from the bottom of my heart.

Erklärung

Ich versichere, dass ich die von mir vorgelegte Dissertation selbständig angefertigt, die benutzten Quellen und Hilfsmittel vollständig angegeben und die Stellen der Arbeit - einschließlich Tabellen, Karten und Abbildungen -, die anderen Werken im Wortlaut oder dem Sinn nach entnommen sind, in jedem Einzelfall als Entlehnung kenntlich gemacht habe; dass diese Dissertation noch keiner anderen Fakultät oder Universität zur Prüfung vorgelegen hat; dass sie - abgesehen von den auf Seite 157 angegebenen Teilpublikationen - noch nicht veröffentlicht worden ist sowie, dass ich eine solche Veröffentlichung vor Abschluss des Promotionsverfahrens nicht vornehmen werde. Die Bestimmungen der Promotionsordnung sind mir bekannt. Die von mir vorgelegte Dissertation ist von Prof. Dr. T. Michely betreut worden.

D Curriculum Vitae

Personal details

Name: Macko
First Name: Sven
Date of birth: 01.10.1979
Place of birth: Duisburg, Germany

Education

10/2007 – 10/2011
Doctoral Thesis in Physics, University of Cologne, Germany
• Thesis: Mechanisms and Manipulation of Pattern Formation on Silicon
• Modification and nanostructuring of semiconductor surfaces by ion beam erosion

05/2007 – 10/2007
Scientific Assistant, University of Duisburg-Essen, Germany
• Development of a photo-bio-reactor - a new technology
in the area of clean tech and CO_2 reduction

10/2000 – 05/2007
Higher Education in Physics, University of Duisburg-Essen, Germany
• Diploma Thesis: Optical Investigations of Organic Azo-Benzene Thin Films
• Major field of study: materials science, optics, polymer physics,
functional materials
• Minor field of study: anorganic chemistry, analytical chemistry
• Grade point average 1.6 (best score 1.0 of 6.0).

10/1999 – 08/2000

Social Service, St. Johannes Hospital, Duisburg, Germany

• Dept. of Medical Technology: Administrative tasks associated with medical-technical instruments

08/1990 – 06/1999

Landfermann-Gymnasium (High School), Duisburg, Germany

• Major subjects: Mathematics, Geography, Music, Sports

• Grade point average 2.3 (best score 1.0 of 6.0).

Recognition

Invited talk at the International Conference on Ion Beam Modification of Materials (IBMM), Montréal, Canada, Aug. 2010.

Featured cover article: Macko et al. *Nanotechnology* **21** (2010), 085301.